# NON-EQUILIBRIUM DYNAMICS: REACTION-DIFFUSION SYSTEMS AND VISCOUS FLOW NEAR THE GELATION TRANSITION

by

Daniel Vernon

B.A., Cornell University, 1996

M.Sc., Simon Fraser University, 1999

A THESIS SUBMITTED IN PARTIAL FULFILLMENT
OF THE REQUIREMENTS FOR THE DEGREE OF
DOCTOR OF PHILOSOPHY
in the Department
of
Physics



SIMON FRASER UNIVERSITY

August 2004

# APPROVAL

| | |
|---|---|
| **Name:** | Daniel Vernon |
| **Degree:** | Doctor of Philosophy |
| **Title of thesis:** | Non-Equilibrium Dynamics: Reaction-Diffusion Systems and Viscous Flow Near the Gelation Transition |
| **Examining Committee:** | Dr. Howard Trottier, Professor of Physics<br>Chair |
| | Dr. Michael Plischke, Professor of Physics<br>Senior Supervisor |
| | Dr. David Boal, Professor of Physics |
| | Dr. Michael Wortis, Professor of Physics |
| | Dr. Igor Herbut, Associate Professor of Physics<br>Internal Examiner |
| | Dr. Michael Thorpe, Professor of Physics<br>Arizona State University<br>External Examiner |
| **Date Approved:** | August 10, 2004 |

# SIMON FRASER UNIVERSITY

## Partial Copyright Licence



Bennett Library
Simon Fraser University
Burnaby, BC, Canada

# Abstract

Many physical systems are found in non-equilibrium states, and the usual methods of statistical mechanics cannot be used to describe them. In general, this means that many more kinds of behaviour are possible, and that the universality seen in equilibrium statistical mechanics does not necessarily occur. However, in some models a critical point appears, and the properties of systems near this critical point may exhibit universal behaviour. In this thesis, we will discuss two kinds of models in which this occurs.

A simple model used to study physics far from equilibrium is a system of reacting and diffusing particles, which may be maintained far from equilibrium by the breaking of detailed balance. For many of these simple systems it is possible to construct a field theory, which can then be studied using renormalization group techniques to determine universal properties. Models with pair annihilation of particles and branching to produce several new particles are studied here, with the addition of anomalous diffusion, in which transport occurs via Lévy flights. Anomalous diffusion is interesting as a model for some physical situations, and also makes it possible to vary continuously the expansion parameter in the renormalization group calculation. The results of analytic calculations and simulations are compared and show the same critical behaviour, with quantities such as the density behaving as power laws close to a critical point.

Another system with interesting dynamics is a complex fluid, or a sol close to its gel transition. The structure of the fluid is modelled by the clusters studied in percolation theory: particles are bonded instantaneously with their nearby neighbours, with a probability $p$. The geometric properties of this model are well understood, behaving

as power laws close to a critical point $p_c$, at which a cluster which spans the entire sample first appears. Adding dynamics then produces a model in which material properties may be calculated, which may have interesting behaviour near the critical point. In particular, the viscosity, which characterizes the non-equilibrium behaviour, is shown by molecular dynamics simulation to diverge as a power law close to $p_c$.

# Acknowledgements

Several people deserve acknowledgement for their contributions to this thesis.

First, thanks to Michael Plischke. I have enjoyed working with him and have learned a great deal from him. He has always been an excellent supervisor.

Two other people have collaborated with me on material which appears in this thesis. Thanks to Martin Howard for suggesting the problem of branching random walks with anomalous diffusion, and for his contributions to that calculation. Thanks as well to Béla Joós for discussions about the viscoelastic properties of materials as discussed in the second half of this thesis.

Thanks also to Martin Siegert, who is responsible for most of the computers used in the simulations in this thesis. Without him, performing these simulations would have been much more difficult.

Finally, thanks are due to the many friends and colleagues who have discussed my work with me.

# Contents

**Approval** ii

**Abstract** iii

**Acknowledgements** v

**Contents** vi

**List of Tables** x

**List of Figures** xi

**1 Introduction** 1

1.1 Reaction-Diffusion Systems . . . . . 1

1.1.1 Mean-Field Results . . . . . 6

1.2 Viscosity Near the Gelation Transition . . . . . 10

**2 Probability and Lévy Distributions** 16

2.1 Transformation of Variables . . . . . 17

2.2 Processes . . . . . 19

2.2.1 Detailed Balance . . . . . 20

2.3 Lévy-Stable Distributions . . . . . 21

2.3.1 Flights and Walks . . . . . 22

2.3.2 Examples . . . . . 23

2.3.3 Large $x$ Expansion of $\rho(x)$ . . . . . 25

2.3.4 An Anomalous Diffusion Equation . . . . . 25
2.4 Generation of Random Numbers . . . . . 26

**3 Derivation of a Field Theory** **28**
3.1 From the M-equation to a Continuum Equation . . . . . 28
3.1.1 Coherent State Representation . . . . . 32
3.1.2 Decay . . . . . 35
3.1.3 Pair Annihilation . . . . . 37
3.1.4 Branching . . . . . 38
3.2 One (or More) Spatial Dimension(s) . . . . . 39
3.2.1 Anomalous Diffusion . . . . . 40
3.3 Langevin Equation for the Annihilation Process . . . . . 40

**4 Renormalization Group Calculations** **47**
4.1 Annihilation Reaction . . . . . 47
4.1.1 Renormalized Annihilation Rate . . . . . 49
4.1.2 Renormalization Group Equation . . . . . 51
4.1.3 Density . . . . . 52
4.2 Branching and Annihilation Reactions . . . . . 56

**5 Simulations** **65**
5.1 Anomalous Diffusion With Pair Annihilation . . . . . 66
5.2 Annihilation and Branching Reactions . . . . . 72
5.2.1 Dynamical Simulations . . . . . 75
5.2.2 Steady-State Simulations . . . . . 79
5.3 Conclusions . . . . . 81

**6 Rheology** **83**
6.1 Introduction . . . . . 83
6.2 Shear Flow . . . . . 84
6.3 Linear Viscoelasticity . . . . . 85
6.3.1 Rheological Functions . . . . . 85

6.3.2 Modelling . . . . . 87
6.3.3 Useful Limits . . . . . 89
6.4 Non-linear Viscoelasticity . . . . . 90
6.4.1 Non-linear Flows . . . . . 90

**7 Gels** **92**
7.1 Percolation . . . . . 92
7.2 Modelling Materials . . . . . 94
7.3 Gels . . . . . 95
7.3.1 Gel Formation . . . . . 96
7.4 Experiments on Viscoelastic Properties of Gels . . . . . 97
7.5 Theoretical Models of Dynamic Properties . . . . . 100
7.5.1 Dynamic Scaling . . . . . 100
7.5.2 Vulcanized Rubber . . . . . 101
7.5.3 The Electrical Analogy . . . . . 102
7.5.4 Rouse Dynamics . . . . . 102

**8 Simulation Techniques** **105**
8.1 Molecular Dynamics . . . . . 105
8.2 Liouville Operators . . . . . 108
8.3 Constant Temperature . . . . . 111
8.4 Homogeneous Shear Flow . . . . . 113
8.5 Shear Flow at Constant Temperature . . . . . 116
8.6 Integration Scheme for Shear Flow at Constant Temperature . . . . . 116
8.7 Green-Kubo Formula for the Viscosity . . . . . 118
8.8 Units . . . . . 118

**9 Molecular Dynamics Simulation Results** **120**
9.1 Model . . . . . 120
9.2 Results in Two Dimensions . . . . . 121
9.2.1 Normal Stress Difference . . . . . 127
9.3 Results in Three Dimensions . . . . . 129

9.4 Conclusions . . . . . 133
9.5 Future Work . . . . . 135

**Bibliography** **138**

# List of Tables


5.1 The amplitude of the density decay for the annihilation problem . . . 72
5.2 Critical probabilities and exponents . . . . . 77
5.3 The exponent $\beta$ . . . . . 81

7.1 Exponents for structural quantities in the percolation problem . . . . 94
7.2 Experimental values of dynamical exponents . . . . . 99
7.3 Theoretical predictions for dynamical exponents in $d = 2$ . . . . . 104
7.4 Theoretical predictions for dynamical exponents in $d = 3$ . . . . . 104

# List of Figures


1.1 Mean-field density in the $A + A \rightarrow \emptyset$ reaction . . . . . 9
1.2 Schematic sol-gel transition . . . . . 12

2.1 Lévy-stable distributions . . . . . 23

4.1 The renormalized annihilation rate . . . . . 49
4.2 The classical density . . . . . 53
4.3 The classical response function . . . . . 54
4.4 The density to one loop . . . . . 56
4.5 Annihilation and branching vertices . . . . . 59
4.6 The renormalized annihilation rate in a field theoretic calculation . . 60
4.7 The renormalized branching rate . . . . . 61
4.8 Regions of different behaviours in the branching problem . . . . . 63

5.1 Density for pair annihilation with normal diffusion . . . . . 67
5.2 Density for pair annihilation with anomalous diffusion . . . . . 69
5.3 Density for pair annihilation, for several values of $\sigma$ . . . . . 70
5.4 The amplitude of the density decay for pair annihilation . . . . . 71
5.5 Sample runs with both branching and annihilation reactions . . . . . 74
5.6 Analysis of effective local exponents . . . . . 76
5.7 The phase diagram for branching and annihilating random walkers . . 78
5.8 Density decay near the critical point . . . . . 80

9.1 A sample configuration of particles . . . . . 122
9.2 The stress-stress correlation function for a simple fluid . . . . . 123

9.3 The stress-stress correlation function at $p = 0.1$ . . . . . 124
9.4 The non-equilibrium shear viscosity as a function of $\dot{\gamma}$ . . . . . 125
9.5 The shear viscosity as a function of $\dot{\gamma}$ at $p = 0.3$ . . . . . 127
9.6 The viscosity as a function of $p$ . . . . . 128
9.7 The normal stress coefficient . . . . . 129
9.8 The normal stress coefficient as a function of $p$ . . . . . 130
9.9 The complex viscosity $\eta^*$ . . . . . 131
9.10 The viscosity in $d = 3$ . . . . . 132
9.11 Finite-size-scaled viscosity . . . . . 133

# Chapter 1

# Introduction

In this thesis we will discuss two different kinds of models for systems which are not in equilibrium. Non-equilibrium phenomena are of increasing interest to physicists, as it becomes clear that many important systems are found in states far from equilibrium. There are many recent reviews of non-equilibrium phenomena. Many of the issues discussed in this thesis are mentioned in a recent collection [1].

Two different kinds of non-equilibrium models will be discussed here. In the first, the system studied is far from equilibrium, but the models studied are very simple, and a reasonably complete theoretical treatment may be carried out. The behaviour of these models may be calculated using both analytic and simulation methods. The examples of this kind of system studied here will involve stochastic systems of moving and reacting particles. In the second part of this thesis we will discuss the viscous flow of a complex fluid. Here, we are interested in behaviour close to equilibrium, and which is often controlled by equilibrium physics. However, the models studied here contain more detailed interactions, and have only been studied using simulation methods.

## 1.1 Reaction-Diffusion Systems

In the first part of this thesis, I will describe the results of some calculations of properties of models of the non-equilibrium behaviour of statistical systems. The

dynamics of systems not in equilibrium have applications in many areas of physics, as well as other fields, and many different methods have been used in their description. The systems studied here are far from equilibrium, and their dynamics may differ from those close to an equilibrium critical point [2]. The methods used include the effects of fluctuations, unlike other, mean-field, approaches. They apply to systems which can be represented as a collection of moving and interacting particles. Measurable macroscopic properties are time dependent due to reactions between particles, rather than due to the imposed external field in driven diffusive systems [3]. The general approach involves mapping a microscopic model to a field theory, and then using renormalization group techniques to study the field theory. These field theoretic techniques are particularly useful for systems in which the number of particles is changing with time.

In physics, obvious examples where this approach could be, and has been, applied include exciton annihilation in solid state materials [4], monopole annihilation in the early universe [5], and chemical reactions. An early mean-field calculation by Smoluchowski [6, 7] of reacting and diffusing particles was in the context of the aggregation of colloidal particles. The dynamics of other models can also be mapped into this kind of model. For example, the growth of domains in a kinetic Ising model can be treated in this way [8]. The motion of a domain wall corresponds to the motion of a particle, and the creation of a new domain of reversed spins to the creation of several new particles. This kind of model is also used to model less physical processes, such as the spread of disease or population dynamics.

The most interesting effects in these systems are due to the breaking of "detailed balance." This is a simple condition on the transition rates between configurations of the system, and is sufficient to guarantee that time averages of measurable quantities of the system are governed by equilibrium statistical mechanics. The detailed balance condition will be given in section 2.2.1. Very complicated rules governing simulations of equilibrium systems can be designed which, as long as they satisfy detailed balance (and make it possible to visit all microstates of the system), produce equilibrium statistical mechanics results. The time-evolution of a model with a particular dynamics may be studied, and can display interesting behaviour, but the

details of the dynamics have no effect on equilibrium statistical averages. This lack of dependence on dynamics is one reason for the usefulness of simple models in the study of statistical systems. It is also the case that, as long as detailed balance is obeyed, even some dynamical properties of systems driven away from equilibrium are controlled by equilibrium physics. The Green-Kubo formula used in the second part of this thesis to calculate the viscosity is an example of this.

Once detailed balance is broken, then there would seem to be many more possibilities for the behaviour of a system. However, there are some cases in which there is universal behaviour, and many details of the system may be ignored. These cases may usefully be treated with the field theoretical methods discussed here.

In some of these systems, there is a quantitative change in the time dependence of macroscopic properties as parameters of the model are changed. This is a non-equilibrium phase transition, as the change is in either the time-dependence of these properties or in their steady-state values. In the cases studied here, the phase on one side of the transition is characterized by a non-zero steady-state density of particles, called the "active state", while on the other side of the transition, there is a power-law decay for all time toward an "absorbing state" with zero particles.

These phase transitions exhibit universality in a way similar to equilibrium phase transitions. Close to a critical point, certain properties are insensitive to changes in irrelevant parameters of the models studied and are also the same between models defined in quite different ways. The number of particles, the distances particles spread, and other measurable quantities each exhibit power law behaviour, as a function of time, while other quantities, such as the steady-state density, are given by power laws in the distance from the critical point. Just as in equilibrium statistical mechanics, the renormalization group is a useful tool to study which features of a system are important to the behaviour of a system.

To model these systems, we begin with a microscopic model describing the dynamics of a collection of particles. This model can be defined by a Master equation (or M-equation), which describes the time-dependence of the probability of finding the system in each possible state. The model thus includes statistics from the outset. This should be thought of as modelling the influence of other degrees of freedom

which are not explicitly included, just as in the description of Brownian motion of a small particle in water by a random walk, rather than explicitly including the many water molecules. For example, in the chemical case, the motion is diffusive, exactly as it is in Brownian motion, while whether or not nearby particles react is governed by quantum mechanics. The quantum mechanical interaction is represented by an effective reaction rate.

Several of the universality classes of non-equilibrium phase transitions have representations as systems of reacting and diffusing particles. The simplest reaction, annihilation of one species of particles in pairs at a rate $\lambda$, is denoted by

$$A + A \xrightarrow{\lambda} \emptyset. \tag{1.1}$$

This system is always at its critical point, with various quantities, such as the density of particles, depending on time as power laws. A renormalization group calculation of the properties of this system with normal diffusion was given by [9].

A simple system with a single species of particles which exhibits a phase transition has the same annihilation reaction and in addition a branching reaction, which produces $m$ offspring at a rate $\mu_m$. This is denoted by

$$A + A \xrightarrow{\lambda} \emptyset \tag{1.2}$$

$$A \xrightarrow{\mu_m} (m+1)A. \tag{1.3}$$

The possibility of different long-time behaviours can be seen from these reactions. If there are no particles, then no particles can be created, and so the system will remain in this state. This is why the state is referred to as the absorbing state. Fluctuations also cease in this state. On the other hand, if $\mu_m$ is large, then there may be a steady state density of particles at long times; in this state, there may be fluctuations around an average density.

The universality class of this system depends on $m$, as can be seen in the renormalization group calculation of Cardy and Täuber [10, 11]. If $m$ is odd, then the behaviour is that of the directed percolation universality class, named after another model falling into this class. The directed percolation problem resembles ordinary

percolation, but a special direction is chosen and bonds may only point in this direction. For example, on a square lattice, bonds from an occupied site may only point up and to the right. If $m$ is even, then a new universality class appears, called the parity conserving class. Here, the parity of the number of particles is constant, as even numbers of particles are are removed or added in any reaction. This is an important change in the dynamics, which results in different long-time behaviour. That this apparently small change is important can be seen by considering a single particle diffusing in a large region empty of other particles. If $m$ is 1, then this particle may create a new particle and then annihilate with it, leaving the whole region empty; other processes with odd $m$ produce similar behaviour. In the case where $m$ is even, new particles are created in pairs, so that this particle, or one of its offspring, will survive until it encounters another particle from outside the empty region. There are several other important universality classes, which are discussed in detail in [12].

The first part of this thesis describes renormalization group calculations and simulations of systems of reacting particles with the addition of long-ranged motion. The two reactions discussed above are studied here: the annihilation reaction alone and the annihilation reaction along with a branching reaction which creates two additional offspring, so that the system is in the parity conserving universality class. Adding anomalous diffusion to these systems is of interest for two reasons. First, anomalous diffusion is important for many different systems, in physics and in other fields, as will be described in chapter 2. Second, the long-ranged motion studied here can act to change the critical dimensions associated with each kind of interaction. This means that by doing simulations in fixed dimension, it is possible to study the the behaviour seen in the normal diffusion model in varying dimension. Since the $\epsilon$-expansion used in the renormalization group calculation is an expansion in the number of dimensions about the upper critical dimension, this expansion can become an expansion in a small parameter, and so the renormalization group results can be easily compared to simulation results. In the case of a reaction with both branching and annihilation of particles, earlier work on the normal diffusion case by Cardy and Täuber [10, 11] predicted that there is an important quantitative change in the behaviour of the system

at a non-integer dimension. In the work reported here, we will see that a similar quantitative change can be explored in one dimension, by varying a parameter controlling the nature of the transport of particles. The behaviour in these two cases is similar in that the fixed point structure is the same, with an additional fixed point appearing as the dimension of the system is varied in the first case and as the transport is varied in the second.

In the next section, we will introduce the exponents describing the behaviour of a reaction-diffusion system close to its critical point and present the mean-field solution to a simple reaction-diffusion problem. In chapter 2, we will discuss some ideas from probability theory which are used in the rest of the thesis, as well as the method used to implement anomalous diffusion: particles are allowed to hop from one lattice site to another, with the hop length chosen from a Lévy distribution. Chapter 3 discusses the method used to derive a field theory or a Langevin equation. This chapter is a review of previous work, although the details of the calculation are somewhat different than in previous work. The field theory, with our new feature of anomalous diffusion, is analysed using renormalization group methods in chapter 4 to calculate several quantities of interest. The results of these renormalization group calculations are compared to simulations in chapter 5. The results in chapters 4 and 5 are the new results in this section of the thesis. The calculations of the properties of a system of particles with both annihilation and branching reactions were done with Martin Howard and appear in [13]. The work done on the system with annihilation alone appears in [14].

### 1.1.1 Mean-Field Results

While most of the work in the first part of this thesis focuses on renormalization group methods, a number of other methods are used to explore the properties of reaction-diffusion systems. In this section we will discuss approximate calculations at a mean-field level, using a differential equation for the number of particles. As is often done, the mean field results will be used to define the exponents governing the behaviour near the critical point.

Much of the work studying the kind of reaction-diffusion systems which are described in this thesis has been done on a mean-field level. One way to describe these processes is with a differential equation for the number of particles. This can be constructed by modifying the normal diffusion equation by adding a term describing the reaction desired. For normal diffusion, and the simple pair annihilation reaction, the time evolution of the number of particles $n(\mathbf{x}, t)$ is given by

$$\frac{\partial n(\mathbf{x}, t)}{\partial t} = D\nabla^2 n(\mathbf{x}, t) - 2\lambda n^{(2)}(\mathbf{x}, t). \tag{1.4}$$

Here, $2\lambda$ is the rate at which particles at the same point annihilate. The last term, $n^{(2)}(\mathbf{x}, t)$, should be the number of pairs of particles at the same point in space, which is not known until the problem is solved. As a first approximation, one could try $n^{(2)} = n^2$, to estimate the number of pairs of particles. This then gives a mean-field equation, or rate equation,

$$\frac{\partial n(\mathbf{x}, t)}{\partial t} = D\nabla^2 n(\mathbf{x}, t) - 2\lambda n^2(\mathbf{x}, t). \tag{1.5}$$

As we will see, the results of this equation are correct in high enough dimension, but there are significant differences between them and the correct behaviour in low dimensions. They are a useful first approximation, and the solution to this kind of equation does appear in the renormalization group calculation later in this thesis.

If the particles move by an anomalous diffusion process, then the normal diffusion term is replaced by an anomalous diffusion term,

$$\frac{\partial n(\mathbf{x}, t)}{\partial t} = D_A\nabla^\sigma n(\mathbf{x}, t) - 2\lambda n^2(\mathbf{x}, t), \tag{1.6}$$

as discussed in section 2.3.4. Some of the features of solutions to this equation will appear in the full solution in chapter 4.

If the density is constant, then the term $D_A\nabla^\sigma n(\mathbf{x}, t)$ is zero, and there is only one steady-state solution, $n = 0$. If the initial density is a constant ($n(\mathbf{x}, t = 0) = n_0$), then the density approaches zero as $n(\mathbf{x}, t) = \frac{n_0}{1+2n_0\lambda t}$. At long times, the leading behaviour is $n(t) \sim (n_0\lambda t)^{-1}$. This gives a mean-field value for a critical exponent $\alpha$, defined by $n(t) \sim t^{-\alpha}$, so the mean-field value is $\alpha_{\mathrm{MF}} = 1$.

If the particles can branch creating $m$ additional particles, then a new term appears in the mean-field equation:

$$\frac{\partial n(\mathbf{x},t)}{\partial t} = D\nabla^{\sigma} n(\mathbf{x},t) - 2\lambda n^2(\mathbf{x},t) + m\mu n(\mathbf{x},t). \tag{1.7}$$

There are now two homogeneous, steady-state ($n$ independent of $x$ and $t$) solutions,

$$n(x,t) = 0 \tag{1.8}$$

and

$$n(x,t) = \frac{m\mu}{2\lambda} \equiv n_s. \tag{1.9}$$

In this mean-field approximation, the second is the stable solution for any $\mu > 0$. The approach to this steady state from an initial density $n_0$ is given by

$$n(t) = \frac{n_s}{1 + \left(\frac{n_s}{n_0} - 1\right) e^{-m\mu t}}. \tag{1.10}$$

This reaction-diffusion equation exhibits a phase transition in its time-dependent behaviour. For $\mu = 0$, we have the pure annihilation process of equation 1.6, in which the density goes to zero as a power law in time. For all $\mu > 0$, there is a non-zero steady-state density at large times. This gives another critical exponent $\beta$, given by the dependence of the density of particles as $t \to \infty$ on the distance $\Delta = \mu - \mu_c$ from the critical point: $n_s \sim (|\Delta|)^{\beta}$. In this approximation, the critical point is at $\mu_c = 0$; since the steady state density is $n = n_s \sim (\mu - 0)^1$, the mean field value of $\beta$ is $\beta_{\mathrm{MF}} = 1$. In this regime, the difference of the density from the steady state density at time $t$ decreases exponentially in $t$, as can be seen from (1.10). For $\mu < 0$, which can effectively occur if single particles may spontaneously annihilate, the density approaches zero exponentially fast.

There are in fact two different exponents conventionally called $\beta$. The first is as described above, giving the dependence of the long-time density on $\Delta$, and will be called $\beta_{\mathrm{dens}}$. The second, called $\beta_{\mathrm{seed}}$, determines the dependence on $\Delta$ of the probability that a finite cluster of particles at $t = 0$ (the seed) survives to $t = \infty$: $P_{\infty} = (\mu - \mu_c)^{\beta_{\mathrm{seed}}}$. In high enough dimension, a random walk or Lévy flight never

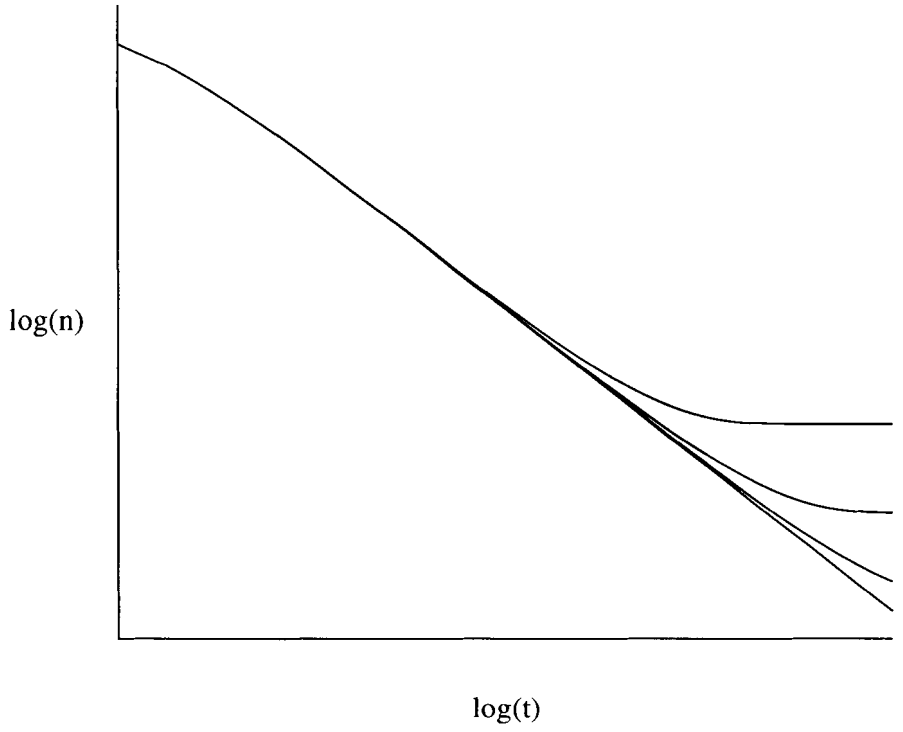


Figure 1.1: The decay of the number of particles in the mean-field approximation to a system of diffusing particles which annihilate in pairs and can branch to produce a single "offspring" particle. The lowest curve shows the power law density decay at $\mu_c$, while the other curves show the increasingly rapid exponential decay to a steady state as $\mu$ increases.

returns to its original position, so that two particles released from the origin will never meet again. (Consider one as stationary and the other as the walker.) This then means that the mean field value of $\beta_{\text{seed}}$ is zero; for any $\mu > 0$, there is a finite probability that the cluster will survive forever.

Several additional exponents are associated with the structure of clusters grown from a seed of a few particles. The first gives the power law decay of the probability that at least one particle survives to time $t$ (the "survival probability"), $P(t) \sim t^{-\delta}$. The second gives the mean squared distance the particles spread, $R^2(t) \sim t^{2/z}$. A third gives the average number of particles at time $t$, $N(t) \sim t^{\theta}$. $N$ is used here rather than the density $n$ as this situation is thought of as the growth from a small seed into

an infinite lattice, so that the density is zero. The exponent $\theta$ is, in general, different from the exponent $\alpha$ governing the density decay starting from a large uniform density. These exponents do not have mean field values, as they are associated with a special, very non-uniform, initial condition.

Two additional exponents are defined by the divergence of the correlation lengths in the temporal and spatial directions near the critical point. In general, the correlations will be different in the temporal direction and in the spatial direction, which is perpendicular to the temporal direction in a space-time diagram. These correlation lengths are denoted by $\xi_\parallel$ and $\xi_\perp$ (parallel and perpendicular to the direction of time.) The two exponents are $\xi_\parallel \sim |\Delta|^{\nu_\parallel}$ and $\xi_\perp \sim |\Delta|^{\nu_\perp}$. In the mean-field approximation, they are $\nu_\parallel = 1$ and $\nu_\parallel = 1/\sigma$. The dynamical exponent $z$, defined by $\xi_\perp \sim \xi_\perp^{1/z}$, is thus $z_{\rm MF} = \sigma$.

Attempts have been made to improve the mean field equations treated here by adding a noise term to produce, for the pair annihilation process with normal diffusion,

$$\frac{\partial n(\mathbf{x},t)}{\partial t} = \nabla^2 n(\mathbf{x},t) - 2\lambda n^2(\mathbf{x},t) + \zeta(\mathbf{x},t). \tag{1.11}$$

Here, $\zeta(\mathbf{x},t)$ is a random variable. The mean field equation may not correctly describe a given physical system, as it neglects possible correlations in the density. The noise term is intended to replace the effects of the correlations lost by replacing the unknown two-particle density by the density squared. However, the properties of $\zeta(\mathbf{x},t)$ are not known in advance, and must be derived by some procedure similar to that in chapter 3.

## 1.2 Viscosity Near the Gelation Transition

In the second part of this thesis, I will present results of simulations of a model for a complex fluid. The fluid studied is made up of small subunits, representing atoms or molecules, which are joined together in a random way. The number of crosslinks joining the subunits provides a parameter which can be used to tune the properties of the fluid, with macroscopic properties taking on different values as the number of crosslinks is varied. The region of particular interest is close to the transition to a disordered solid, or gel state. There are a number of physical systems which

undergo similar transitions. A number of different kinds of gels, made with different materials crosslinked either from a dense fluid or from a suspension of a solute in a solvent, have been studied in experiments. These gels are interesting for a number of reasons, as examples of an equilibrium disordered solid. The fluid phase, called a sol, also displays unusual characteristics in its macroscopic parameters. For example, the viscosity diverges as a power law, in a way which may be universal across a number of different materials, at the transition to the solid gel phase. In the solid phase, the shear modulus follows a power law dependence on the distance from the transition. This solidification transition is quite different from the first-order transition to a crystalline state.

In addition to the gels themselves, a number of other systems have similar disordered microscopic structures. Many plastics are made up of long chain polymers, joined by randomly placed crosslinks, as is vulcanized rubber. In the preparation of these materials, a number of polymer chains are mixed together with a crosslinking agent, which then selects random pairs of chains to link together. As this crosslinking progresses, the material changes from a fluid of independent polymers, to a more viscous fluid of crosslinked polymers, and then to a solid phase, with a subset of the polymer chains linked into a single giant molecule which spans the entire sample.

There is another transition to a disordered solid state, the glass transition, which has some similarities to the gel transition. In glassy materials, both simple glasses such as silica window glass and in more complex polymer glasses, the viscosity increases dramatically as the glass transition temperature is approached from the high temperature side. Eventually, the viscosity becomes large enough that the material will not flow under a small stress on any possible experimental timescale, and so it may be treated as a solid. It is possible that some glasses acquire a yield stress, so that they will never flow below some fixed stress.

The differences between a sol-gel transition and a glass transition are a subject of current debate. However, there are some features that seem to distinguish the two transitions. As the gel transition is approached, a characteristic length scale associated with the static structure of the gel diverges. Some of the particles which make up the sol, or incipient gel, are bonded to each other, with bonds which are permanent

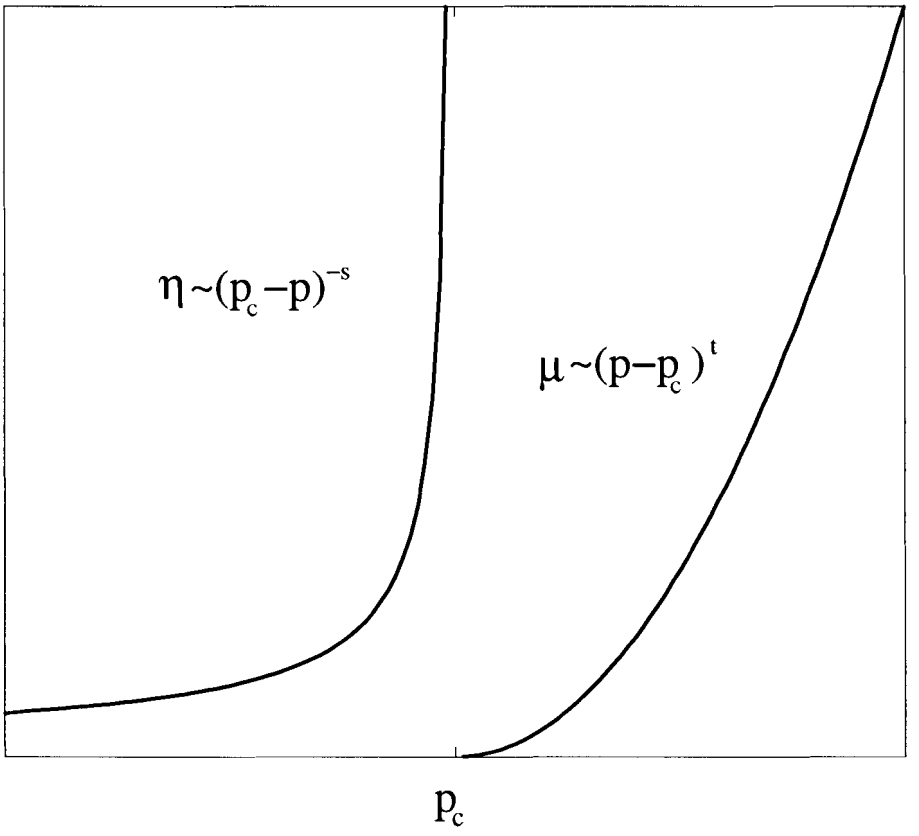


Figure 1.2: A schematic picture of the behaviour of the material properties near a sol-gel transition, as a function of the density of crosslinks $p$. At low crosslink density, the viscosity increases as a power law as $p$ is varied, diverging at the critical point. At $p_c$, the fluid becomes a solid, with a shear modulus which increases from zero at $p_c$ as a power law as $p$ increases.

in some cases, and merely very long lived in other cases. The sets of particles which are bonded to each other form clusters, which have a characteristic length scale. This length scale diverges at the gel point. Glasses may form with no additional bonds, only the interactions which are present in a low-viscosity fluid or a solid of the same collection of atoms. At any time, the structure of a glass is similar to that of a fluid of the same constituents. There is no length scale associated with the static structure which grows as the glass transition is approached. All static correlations remain a few particle spacings at the largest. The dynamics of a glass can exhibit a growing length scale: the size of regions in which the motion of particles is correlated may grow [15].

Gels and glasses also differ in that a glass is a non-equilibrium material, while a gel may not be. Glasses are formed when liquids are cooled quickly enough that they do not crystallize. There is a lower free energy crystalline state, but this ordered structure cannot be reached. Even before the glass transition temperature, the glass-forming liquid falls out of equilibrium, and the highly viscous fluid observed is in a non-equilibrium phase. A gel formed with permanent crosslinks is, in principle, an equilibrium system. The structure is the result of a non-equilibrium process, but once the structure is formed, the gel may explore all of phase space consistent with this initial structure. In experiments, it may be difficult to see that a gel is in equilibrium, as the timescales for relaxations become very large as the gel transition is approached. However, in a theoretical treatment of a gel, averages may be performed over the entire phase space available to the crosslinked material. To describe a glass, the region of phase space associated with the crystal structure must be explicitly excluded. Some gels do exhibit a non-equilibrium effect called ageing, in which certain properties are time-dependent. However, it is not clear whether this ageing is intrinsic or extrinsic, or in other words whether it is directly related to the dynamics of the gel or is due to the influence of external forces such as gravity.

Another system in which a gel transition can be seen is a colloidal suspension in which a number of small particles are suspended in a solvent. A colloidal suspension in which the interactions between particles is purely repulsive has a glass transition. Here, the temperature is not the control parameter; instead, the transition occurs as the volume fraction occupied by particles increases. If the suspension is not allowed to crystallize, then a glass is formed at a volume fraction $\phi_c$ (with $\phi_c \approx 0.58$ for hard spheres) for many different colloidal systems. This is again a non-equilibrium structure, with a crystal structure available at the same packing fraction. Colloidal glasses exhibit ageing, another sign of their non-equilibrium nature.

A colloidal suspension in which there are attractive interactions between the colloidal particles may form a gel. If the attractions are strong enough, colloidal particles which come close to each other may become bonded, either permanently or for very long times. The bonded particles may then form a sample-spanning network at arbitrarily low volume fractions. This network provides the rigidity associated with the

gel state. There is currently some debate as to the differences between a colloidal glass and gel states (see [16]), due in part to a lack of consensus about the correct definition of a gel state. Colloidal gels also seem to exhibit ageing. However, it is possible that this ageing is due to the influence of external forces, such as gravity. In a colloidal suspension under the influence of gravity, the colloidal particles will eventually sediment out to the bottom of the container in which they are placed. It is possible that the gel state would be an equilibrium one in the absence of external forces.

There is as yet no complete theory to describe the macroscopic properties of these randomly crosslinked fluids. One approach which can be taken to describe these materials is to use the ideas of percolation theory to model the structure of the crosslinked fluid. In percolation theory, the geometric properties of a randomly linked lattice are studied, and the universal properties of these structures are used to describe disordered structures which appear in many different areas of physics. Some of the results of percolation theory will be presented in chapter 7.

However, even with the same model for the structure of a material near a sol-gel transition, and very similar assumptions about the dynamics, different theories predict quite different mechanical properties. In the work presented in this thesis, the structure of a gelling material is modelled by the random lattices of percolation theory and the dynamics of these structures studied using molecular dynamics simulations. The hope is that a complete molecular dynamics calculation with a particular model will make it possible to determine what the important features of the microscopic models are.

Two different techniques have been used to calculate viscoelastic properties of complex fluids in simulations. In the first, an equilibrium simulation is done and the response of the system to an external force extracted from a Green-Kubo relation. These relations are derived from linear response theory and relate fluctuations in an equilibrium system to transport coefficients governing non-equilibrium systems. In the second, a flowing system is simulated and the viscosity extracted from the force required to create the flow. Results from both of these methods will be presented in this thesis.

The phenomenology of fluid flow and the language used to describe the viscoelastic response of a material to external forces will be discussed in chapter 6. In chapter 7, I will describe the use of percolation theory to model the structure of a material near a gel transition and will discuss several experiments done on gels to determine their microscopic structure and their transport coefficients. In chapter 8, I will describe the molecular dynamics techniques used, and the results of these simulations will be presented in chapter 9. These simulations in which a Green-Kubo technique is used to calculate the viscosity are from work done with Michael Plischke and Béla Joós, and are discussed in reference [17].

# Chapter 2

# Probability and Lévy Distributions

Probability theory has a long history. It began with practical applications to problems which arose in gambling but has become a large branch of mathematics, much of which is concerned with problems quite far from the original motivation. Its basic principles are described in many books, such as [18, 19]. Only a few ideas from probability theory are needed in this thesis, and they will be briefly reviewed here. In this chapter we will also discuss the properties of Lévy distributions. Particles with motion controlled by Lévy flights diffuse anomalously, and this will be used later in the thesis. We will discuss their form in both real and Fourier space, as well as a few experiments in which they occur and the methods used to generate them in simulations.

Probability theory has been reduced to a purely axiomatic theory by Kolmogorov. A set of possible events, called a "sample space", is chosen. A probability is defined on each subset of the sample space, which must obey three axioms. For each subset $A$, the probability $P(A)$ is non-negative, the probability associated with the whole set is $P(S) = 1$ and if $A$ and $B$ are disjoint sets, then $P(A + B) = P(A) + P(B)$. The standard results of probability theory then follow.

Two different methods are used to make a connection between this abstract probability theory and experiments. In the first, an ensemble picture, an experiment is imagined to be done many times, either on the same system many times or on a large number of identically prepared systems. The probability of an outcome is then the fraction of systems which produce that outcome. In the second method, a probability

is taken to represent our state of knowledge of a system, and arguments are then made about the plausibility of derived statements.

The idea of a sample space applies most easily to discrete variables. However, it may be extended to a continuous variable in a simple way. If a "probability density function" $\rho(x)$ is defined on the real numbers $x$, the probability of finding a value between $x$ and $x+\mathrm{d}x$ is $\rho(x)\mathrm{d}x$; in an ensemble picture, this is the fraction of systems found in this range. It is traditional in physics to use $\rho$ to represent many different probability distribution functions, with a subscript if necessary to distinguish different functions, as in $\rho_x$ for the distribution of possible values of the variable $x$. Once $\rho(x)$ has been defined, expectation values of functions of the random variable $x$ are given by integrals over this distribution: $\langle f(x)\rangle = \int \mathrm{d}x f(x)\rho(x)$. The expectation value of a function is the average value obtained after many measurements of this function.

Often not all of the information contained in the probability distribution function is necessary. Instead, only the first few moments are important. The $n$-th moment of a distribution is given by the expectation value of $x^n$. The average is then simply the first moment, while the second moment, if it exists, gives a measure of the width of the distribution.

The characteristic function $G(k)$ of a probability distribution is the expectation value of $\exp(ikx)$, or the Fourier transform of the probability distribution:

$$G(k) = \tilde{\rho}(k) = \langle e^{ikx}\rangle = \int \mathrm{d}x \rho(x) e^{ikx}. \tag{2.1}$$

This function is also referred to as the moment generating function, as the coefficients of a Taylor expansion in $k$ are proportional to the moments of the distribution $\rho(x)$.

A probability distribution can be defined for multiple random variables as well. If the distribution factors so that $\rho(x_1, x_2, \ldots) = \rho_{x_1}(x_1)\rho_{x_2}(x_2)\ldots$, then the $x_i$ are independent random variables.

## 2.1 Transformation of Variables

Once the fundamental objects are defined, the rest of probability theory consists of transformations of variables. The probability distribution over a sample space is

assumed known, and probability distributions of functions of the random variable are calculated. When changing from $x$, with distribution $\rho_x(x)$, to a new variable $z = f(x)$, the new distribution $\rho_z(z)$ is given by integration of $\rho_x(x)$ over all $x$, subject to the constraint that $f(x) = z$:

$$\rho_z(z) = \int \mathrm{d}x \rho_x(x) \delta(z - f(x)) = \sum_i \frac{1}{\left|\frac{\mathrm{d}f}{\mathrm{d}x}\right|_{x_i}} \rho_x(x_i). \tag{2.2}$$

The sum occurs as $f$ may not be one-to-one and is over solutions $x_i$ to $z = f(x_i)$. If $f$ is one-to-one, then there is only one term in the sum, and the same result can be seen from the identity for a change of variables from $x$ to $z(x)$,

$$\int \mathrm{d}z \rho_z(z) = 1 = \int \mathrm{d}x \rho_x(x) = \int \mathrm{d}z \left|\frac{\mathrm{d}x}{\mathrm{d}z}\right| \rho_x(z), \tag{2.3}$$

which then implies $\rho_z(z) = \left|\frac{\mathrm{d}x}{\mathrm{d}z}\right|_{x(z)} \rho_x(x(z))$.

For example, if $z(x) = -\ln(x)$, and $x$ is uniformly distributed between 0 and 1 (so that $\rho(x) = 1$ for $0 < x < 1$), then $\rho_z(z) = e^{-z}$, that is, $z$ is a new random number with an exponential distribution.

A simple transformation is the addition of two random variables. Given a joint probability distribution for two variables $x$ and $y$, $\rho(x, y)$, the probability distribution of the sum $z = x + y$ is

$$\rho_z(x) = \int \mathrm{d}x \mathrm{d}y \rho(x, y) \delta(z - (x + y)) = \int \mathrm{d}x \rho(x, z - x). \tag{2.4}$$

This is simply the sum all ways in which $x$ and $y$ can add up to $z$. If $x$ and $y$ are independent, then

$$\rho(z) = \int \mathrm{d}x \rho_x(x) \rho_y(z - x). \tag{2.5}$$

This is the convolution of the distributions of the variables being added, and the characteristic function associated with $\rho_z(z)$ is thus just the product of the two characteristic functions associated with $\rho_x(x)$ and $\rho_y(y)$, so that $G_z(k) = \hat{\rho}(k) = G_x(k) G_y(k) = \hat{\rho}_x(k) \hat{\rho}_y(k)$, as long as $x$ and $y$ are independent random variables.

## 2.2 Processes

Once a probability distribution is defined, it can be extended to the idea of a stochastic process, discussed at length in [19]. This is an extension of the idea of a single random variable to a random variable which changes with time, representing the evolution of a system. The basic idea is simple. The system studied is thought of as making transitions from one state to another with some distribution of new states, which may depend on the current state and on previous states. The simplest case, in which the probability of making a transition to another state depends only on the current state of the system and the state to which the transition is to be made, is called a Markov process. All processes discussed in this thesis are Markov processes. The evolution may be represented by following a single realization of the system through a series of transitions, with new configurations chosen at random from the possible configurations. This is done in a simulation, using a random number generator to choose the next configuration. Both the equilibrium, statistical mechanical, properties and the non-equilibrium, statistical dynamical, properties may be studied in this way. The dynamics may also be studied by following the evolution of the probability distribution, using the rules for the transformation of variables discussed in the previous section. The analytic calculations in chapter 4 use this kind of approach.

One common way to study the evolution of a system is through a Langevin equation. In this approach, a continuum limit is taken in time, and a differential equation is written for the time evolution of the probabilities of finding the system in a given state, if it starts in a known state. There are two pieces to a Langevin equation. The first piece gives a deterministic evolution and if it appeared alone, could be treated as a standard differential equation. The second piece takes account of fluctuations and is referred to as a noise term. The form of a Langevin equation is

$$\frac{\partial n}{\partial t} = f(n) + \zeta g(n) \tag{2.6}$$

where $f$ and $g$ are given functions of the current density, and $\zeta$ is a noise function. The properties of $\zeta$ are usually specified by its moments, or the correlation function between $\zeta$ at different times and spatial positions. The determination of $\zeta$ for a specific

physical system is often a difficult problem. Under some circumstances, such as when the system is approaching equilibrium, the form of $\zeta$ is determined by equilibrium physics. In the non-equilibrium systems studied here, the properties of $\zeta$ must be derived in some other way from a microscopic model.

### 2.2.1 Detailed Balance

We will be concerned with non-equilibrium systems for much of this thesis. However, we will briefly discuss a condition which ensures that the sequence of states generated in a simulation does represent an equilibrium system, as the breaking of this condition is important so as to generate genuinely non-equilibrium dynamics, even at large times. This condition is called "detailed balance". It is a condition on the transition rates from one microscopic configuration of the system to another. It is described in most books which discuss simulations in statistical mechanics, such as [20].

We will discuss detailed balance in the context of a system with a finite number of possible states. Then the transition probabilities $W_{ji}$ from state $i$ to state $j$ form a matrix and the probabilities of finding the system in state $i$ form a vector. The effect of a single timestep is given by applying the transition matrix $W_{ji}$ to the vector giving the current set of probabilities. If there is a steady state probability vector $\pi_i$, it must be an eigenvector of $W_{ji}$ with eigenvalue 1, so that

$$\pi_j = \sum_i W_{ji}\pi_i. \tag{2.7}$$

The detailed balance condition gives a relation between the transition probabilities between a pair of states in terms of the steady state probabilities, as

$$\frac{W_{ji}}{W_{ij}} = \frac{\pi_j}{\pi_i}. \tag{2.8}$$

The transition probabilities out of state $i$ must be normalized, so that starting in state $i$ some state is reached with probability 1:

$$\sum_j W_{ji} = 1. \tag{2.9}$$

Using this normalization condition in (2.8), after rearranging and summing over $j$, we find

$$\pi_i = \sum_j W_{ji}\pi_i = \sum_j W_{ij}\pi_j. \tag{2.10}$$

This shows that $\pi_i$ is indeed an eigenvector of $W_{ji}$ and is therefore a steady state probability vector. If the system is a standard statistical mechanics model, in which the energy of state $i$ is given by $E_i$, the steady state probability should be $\pi_i = e^{-\beta E_i}/Z$. Equation (2.8) then provides limits on how transition rates may be chosen to make this be a steady state solution, with different choices of $W_{ji}$ possible. For each of the choices consistent with detailed balance, there will be some dynamics of the system as it approaches equilibrium. However, the detailed balance condition and the fact that the system is approaching an equilibrium state produce important constraints on these dynamics. In particular, if the dynamics are described by a Langevin equation with a deterministic part plus a noise term, the form of the noise term is fixed by equilibrium physics [21].

In the models studied here, the detailed balance condition is broken. This creates the possibility of many different kinds of dynamics and removes the constraint on the noise term. The formal approach described in chapter 3 must be used to derive the form of the noise.

## 2.3 Lévy-Stable Distributions

The Gaussian distribution appears frequently in many areas of physics and mathematics. One reason for this importance comes from the central limit theorem: given any distribution with a finite second moment, the sum of numbers chosen from this distribution, after enough numbers are added, has a Gaussian distribution. The Gaussian is also "stable", which means that if two numbers drawn from a Gaussian are added, the distribution of the sum is again a Gaussian with a rescaled second moment. The importance of these properties led mathematicians to look for other distributions with the same properties. The set of all possible (symmetric) distributions which are stable was given by Paul Lévy. These distributions have Fourier transforms (or

characteristic functions)

$$\tilde{\rho}(k) = e^{-D_A|k|^\sigma}, \qquad 0 < \sigma \leq 2. \tag{2.11}$$

Here $\sigma$ is a parameter which controls the shape of the distribution and $D_A$ is a scaling parameter. For $\sigma = 2$, this is a Gaussian distribution. For $\sigma > 2$, the inverse Fourier transform has negative regions and therefore cannot be a probability distribution. For all other values, $0 < \sigma < 2$, the real-space distributions have power law tails, of the form

$$\rho(r) \sim \frac{1}{r^{d+\sigma}} \tag{2.12}$$

in $d$ dimensions. The second moment is thus infinite and so the distribution can avoid the central limit theorem. The fact that these distributions are stable can be seen from the characteristic function; the product of two functions of the form (2.11) has the same form, with a new $D_A$.

The real space distributions cannot be written in closed form for most Lévy distributions. Only for a few special cases, such as $\sigma = 1$ (the Lorentzian) and $\sigma = 2$ (the Gaussian), is this possible.

### 2.3.1 Flights and Walks

There are two distinct ways in which the motion of a particle can follow a Lévy law. In the first, a particle moves in a randomly chosen direction for a distance chosen from a Lévy distribution, but at constant velocity. This is called a Lévy walk. In the second, the distance moved is again chosen from a Lévy distribution, but the move is made in a fixed time, independent of the distance. This is called a Lévy flight. It is the Lévy walk which appears in most physical examples, although some systems do exhibit signs of Lévy flights. Only Lévy flights were studied in this thesis.

One way to describe a stochastically moving object is with a continuous-time random walk. Both the distance travelled and the time taken to make this step are chosen from a probability distribution, with the distribution for $t$ depending on the value of $x$ chosen. This is written $\rho(x,t) = \rho(x)\rho(t|x)$. $\rho(x)$ can be a Lévy distribution and with a suitably chosen $\rho(t|x)$, the second moment, which is the root mean squared

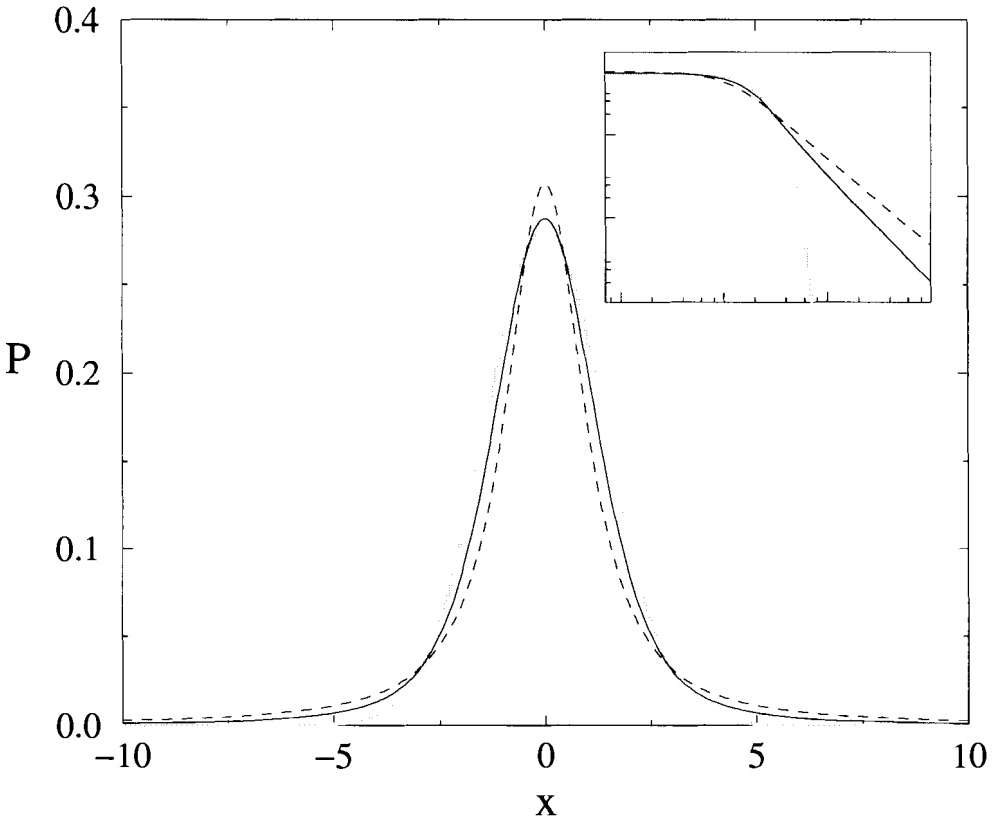


Figure 2.1: Two Lévy-stable distributions, for $\sigma = 1.5$ (solid line) and $\sigma = 1.1$ (dashed line) compared to a Gaussian (grey line). The Lévy distributions are narrower and sharper than the Gaussian, but have much more weight in the tails, as can been seen in the inset, where the same distributions are shown on a log-log plot.

distance travelled at time $t$, may be finite if desired. Many different types of anomalous diffusion may then be described. The Lévy walk is given by $\rho(t|x) = \delta(t - x/v)$, while a Lévy flight is given by $\rho(t|x) = \delta(t - 1)$. This is of course not a continuous-time process but is defined only on integer values of $t$.

### 2.3.2 Examples

These distributions can arise in a number of different physical contexts, both experimental and theoretical. Anomalous diffusion is often associated with disordered

structures, as discussed in detail in [22], but is also seen in systems with complicated dynamics, such as turbulent flow.

An early use of Lévy statistics in physics was in the explanation of conductivity in amorphous semiconductors after the creation of electron-hole pairs by exposure to an intense pulse of light [23, 24]. In this process, holes were assumed to be confined to traps for waiting times distributed according to a Lévy distribution. This trapping then leads to a time-dependent current different from that predicted for normal diffusion of holes, as was seen in experiments.

The motion of a tracer particle in turbulent fluid flow in a rotating tank is governed by Lévy statistics [25, 26]. In these experiments, an annular tank filled with a glycerol solution is rotated at 1.5 Hz, and a turbulent flow is created by pumping fluid through holes in the bottom of the tank. When the flow is chaotic, vorticies are formed at various points around the tank. Tracer particles are then introduced and their motion tracked as a function of time. These tracer particles following the flow and perform random walks in the azimuthal direction. The motion during each step of the random walk is taken at constant velocity, and the distribution of step lengths is a power law: the probability of a step through an angle $\theta$ is $P(\theta) \sim \theta^{-2.05\pm0.30}$. This corresponds to a Lévy walk with an exponent $\sigma \approx 1.05$. For many of these steps the tracer moves within a single vortex, while the long-ranged steps occur when the tracer moves from one vortex to another.

Lévy flights have also been seen in the diffusion of a tracer particle in a system of transient micelles [27]. In this experiment, a fluorescent probe molecule is introduced to a system of elongated micelles, which break apart and reform during the course of the experiment. The probe molecule is similar to those that make up the micelles, and is incorporated into one of them. As the micelles break into their constituent molecules and form new micelles, the tracer particles will be part of micelles of different sizes. Micelles of different sizes diffuse at different rates and carry the probe molecules with them. This leads to anomalous diffusion of the probe molecules, with $\sigma$ between 1.55 and 2.04. This seems to be the only experimental case in which a true Lévy flight has been observed.

### 2.3.3 Large $x$ Expansion of $\rho(x)$

In real space, a Lévy distribution is given by the inverse Fourier transform of equation (2.11)

$$\rho(x) = \frac{1}{2\pi}\int_{-\infty}^{\infty} \mathrm{d}k e^{-|k|^\sigma} e^{ikx}. \tag{2.13}$$

Since $e^{-|k|^\sigma}$ is symmetric, this is the same as

$$\rho(x) = \frac{1}{\pi}\mathrm{Re}\int_{0}^{\infty} \mathrm{d}k e^{-k^\sigma} e^{ikx}. \tag{2.14}$$

The integrand vanishes on a quarter-circle in the lower right quadrant taken to infinity, so the contour of integration can be rotated to the negative imaginary axis:

$$\rho(x) = \frac{1}{\pi}\mathrm{Re}\int_{0}^{-i\infty} \mathrm{d}k e^{-k^\sigma} e^{ikx}. \tag{2.15}$$

Changing the integration variable to $v = -ikx$,

$$\rho(x) = \frac{1}{\pi}\mathrm{Re}\frac{i}{x}\int_{0}^{\infty} \mathrm{d}v e^{-(iv/x)^\sigma} e^{-v} = \frac{1}{\pi}\mathrm{Im}\frac{1}{x}\int_{0}^{\infty} \mathrm{d}v e^{-(iv/x)^\sigma} e^{-v}. \tag{2.16}$$

After substituting an expansion of the first exponential which is valid for large $x$, $\exp(-(iv/x)^\sigma) \approx 1 - \frac{1}{x^\sigma}(iv)^\sigma + \frac{1}{x^{2\sigma}}(iv)^{2\sigma}$, the first term is purely real, so the first non-zero contribution is

$$\rho(x) \approx \frac{1}{\pi}\mathrm{Im}\frac{i^\sigma}{x^{\sigma+1}}\int_{0}^{\infty} \mathrm{d}v v^\sigma e^{-v} = \frac{1}{\pi}\frac{1}{x^{\sigma+1}}\Gamma(\sigma+1)\mathrm{Im}(i^\sigma), \tag{2.17}$$

and $i = \exp(i\pi/2)$, so

$$\rho(x) \approx \frac{1}{\pi}\frac{1}{x^{\sigma+1}}\sin\left(\frac{\sigma\pi}{2}\right)\Gamma(\sigma+1). \tag{2.18}$$

This is the first term in an asymptotic expansion of $\rho(x)$.

### 2.3.4 An Anomalous Diffusion Equation

The motion of particles according to a Lévy flight may be described by a variation on the diffusion equation. In a time $\Delta t$, the particles take a step chosen from a distribution $\rho_1(x)$, where $\rho_1$ is a Lévy distribution. In Fourier space, the probability

distribution for the position of a particle at time $t + \Delta t$ is then related to that at time $t$ by

$$\tilde{\rho}(k, t + \Delta t) = \tilde{\rho}(k, t)\tilde{\rho}_1(x). \tag{2.19}$$

If $\rho_1$ is a Lévy distribution, then the first two terms in an expansion in $k$ are $\rho_1(k, t) \approx 1 - a|k|^\sigma$ with $a$ a constant, so that

$$\tilde{\rho}(k, t + \Delta t) - \tilde{\rho}(k, t) = a\tilde{\rho}(k, t). \tag{2.20}$$

Dividing by $\Delta t$, and taking the limit $\Delta t \to 0$ with $a/\Delta t = D_A$ constant,

$$\frac{\partial \tilde{\rho}(k, t)}{\partial t} = -D_A|k|^\sigma \tilde{\rho}(k, t). \tag{2.21}$$

This can be written in position space as

$$\frac{\partial \rho(x, t)}{\partial t} = D_A \nabla^\sigma \rho(x, t), \tag{2.22}$$

where $\nabla^\sigma$ represents the real space operator corresponding to the Fourier space operator in (2.21).

Just as a Gaussian is a solution of the normal diffusion equation with delta function initial conditions, the Lévy distribution of equation (2.11) provides a solution of (2.21), $\tilde{\rho}(k, t) = e^{-D_A|k|^\sigma t}$. This shows that with any distribution of single steps with a lowest term in a Fourier expansion proportional to $|k|^\sigma$ the distribution evolves into a Lévy distribution with Lévy index $\sigma$.

## 2.4 Generation of Random Numbers

Many methods exist for the generation of a sequence of numbers on a computer which have the statistical properties characteristic of a "random" physical process. The most important feature of a random number generator is that the successive numbers produced by the generator are independent or uncorrelated. The most basic problem, the generation of numbers chosen from a uniform distribution, has many different solutions. The simulations done here use the `ranmar` algorithm [28].

Once a sequence of uniformly distributed numbers is available, a sequence of numbers distributed according to other distributions can be constructed. The most straightforward method is the transformation method, which is based on the transformation properties of random variables. Transforming a given a random number $x$ by a given function $y(x)$ produces a new random number with a different distribution, as discussed in section 2.1. This is used to generate new distributions from the flat distribution generated by the random number generator.

Two different methods were used to generate random numbers distributed according to a Lévy law. The first, simpler, method produces a power law tail but does not produce the correct small $r$ behaviour. Since the Lévy distribution is the attractive fixed point for a power law distribution with a given exponent, the long-time behaviour of this distribution is the behaviour needed. The second method is somewhat more complicated but does produce a better match for the Lévy distribution.

To produce the power law distribution, a random number $x$ was chosen from a uniform distribution on the interval $[0, 1)$, and then a new random variable $r = (1-x)^{-1/\sigma}$ was calculated. The numbers $r$ are then distributed according to a power law. Using the results of section 2.1, it can be seen that

$$\rho_z(r) = \left|\frac{\mathrm{d}x}{\mathrm{d}r}\right| \rho_x(x(r)) = \frac{\sigma}{r^{\sigma+1}}. \tag{2.23}$$

Random numbers with a distribution everywhere equal to the Lévy distribution can be produced by a more complicated method described in [29, 30]. First, a number $V$ is chosen from a uniform distribution between $-\pi/2$ and $\pi/2$ and a number $W$ is chosen from an exponential distribution with mean 1. $r$ is then calculated from

$$r = \frac{\sin(\sigma V)}{\cos(V)^{1/\sigma}} \left(\frac{\cos(V - \sigma V)}{W}\right)^{(1-\sigma)/\sigma} \tag{2.24}$$

and has the required distribution. See [29] for a proof that this procedure does in fact produce a sequence of numbers with the correct distribution.

# Chapter 3

# Derivation of a Field Theory

This chapter is a description of an approach which is useful for processes that can be represented as stochastically moving and reacting particles, as discussed in the introduction. The basic approach was developed by Doi [31, 32] and Peliti [33] and is often referred to as the Doi-Peliti method. Their description of this method differs in some ways from that presented here, which is similar to that discussed by Cardy [34] and Lee [9, 35]. By the end of this chapter we will have derived the form of a Langevin equation or a field theory which describes the macroscopic properties of a reaction-diffusion system. Using the method described here the correlations in the noise term in the Langevin equation may be derived, rather than guessed and added to a mean-field equation. In the last section we will also discuss the diagrammatic perturbation theory used to analyse these theories.

## 3.1 From the M-equation to a Continuum Equation

We will begin with an equation describing the time-evolution of the probability of finding the system in each microscopic state. This kind of equation is often called a master equation; van Kampen [19] suggests calling it an M-equation, to avoid confusion when it is not the fundamental equation from which all results are derived. The

form of the M-equation can be derived from probability considerations [19], but we will consider it to define the system studied. Since we begin with an M-equation, we cannot hope to reproduce the exact microscopic dynamics. Instead, we will calculate average properties of the system.

The M-equation for the probability of finding the system in the state labelled by $n$ is written as a sum over all other states $n'$ of the probability of finding the system in state $n'$, times a transition rate $W_{n' \to n}$ from state $n'$ to $n$, minus the sum over all states of the probability of finding the system in state $n$ times the transition rate $W_{n \to n'}$ from $n$ to $n'$.

The general procedure used here will be to map the M-equation into a field theory, which can then be used to calculate observable properties of the model. This field theory will be similar to those appearing in equilibrium statistical mechanics, in which the partition function is written $Z = e^{-S}$, where $S$ is an effective action describing the system. Once an expression of this form is obtained, methods used in equilibrium statistical mechanics, such as the renormalization group, can be applied to the problem. The field theory can also sometimes be used to derive a Langevin equation. Solving either the field theory or the Langevin equation makes it possible to calculate any observable.

We will begin with reactions at a single site and generalize to one or more spatial dimensions later. The only variable in this case is the number of particles $n$, and so the state of the system can be labelled by $n$. These single-site reactions are appropriate for a process with no spatial dependence, such as radioactive decay. The M-equation for this zero-dimensional case is

$$\frac{\mathrm{d}P(n,t)}{\mathrm{d}t} = \sum_{n'} (W_{n' \to n} P(n',t) - W_{n \to n'} P(n,t)). \tag{3.1}$$

This equation is linear in $P$ and is first order in time, so it can be analyzed using a formalism similar to second quantization in quantum mechanics. The state of the system is given by a vector, written in Dirac notation as a ket. The state with exactly $n$ particles can be thought of as an infinite vector with a 1 in the $n$-th position, and the transition rates $W$ as matrices, with non-zero elements where a transition is possible from $n$ to $n'$ particles. Creation and annihilation operators $a^\dagger$ and $a$ can be

introduced to connect states differing in the number of particles, and used to construct the whole set of states starting from a "vacuum state", $|0\rangle$, with no particles, and which is annihilated by the annihilation operator, $a|0\rangle = 0$. The state with $n$ particles is then given by acting on this vacuum $n$ times with the creation operator $a^\dagger$, and is written as $|n\rangle = (a^\dagger)^n|0\rangle$. The creation and annihilation operators have the usual properties, so that $a^\dagger|n\rangle = |n+1\rangle$, $a|n\rangle = n|n-1\rangle$, $[a, a^\dagger] = 1$, and the scalar product is $\langle n|m\rangle = n!\delta_{nm}$. The number operator, $\hat{n} = a^\dagger a$, counts the number of particles in a state: $\hat{n}|m\rangle = m|m\rangle$.

The set of probabilities of finding the system with $n$ particles, $P(n)$, can now be represented by a vector in the space of all possible states:

$$P(n) \rightarrow |P\rangle = \sum_n^\infty P_n|n\rangle. \tag{3.2}$$

In this expression, the vector $|n\rangle$ represents a state with exactly $n$ particles, while a vector $|P\rangle$, which is a "superposition" of $n$-particle states, represents a system with probabilities $P_n$ of being found to contain $n$ particles. The M-equation can now be written as

$$\frac{\mathrm{d}|P\rangle}{\mathrm{d}t} = -\hat{H}|P\rangle, \tag{3.3}$$

where the time-evolution operator $\hat{H}$ contains the transition rates on the right side of the M-equation (3.1).

We need to choose some initial condition. It is convenient to choose a Poisson distribution with average $n_0$

$$P(n, t = 0) = e^{-n_0}\frac{n_0^n}{n!}. \tag{3.4}$$

This distribution is represented by

$$|P(0)\rangle = e^{-n_0}e^{n_0 a^\dagger}|0\rangle \equiv |n_0\rangle, \tag{3.5}$$

which can be seen by expanding the exponential,

$$\begin{aligned} e^{-n_0}e^{n_0 a^\dagger}|0\rangle &= \sum_n^\infty e^{-n_0}\frac{1}{n!}(n_0 a^\dagger)^n|0\rangle \\ &= \sum_n^\infty e^{-n_0}\frac{n_0^n}{n!}|n\rangle. \end{aligned} \tag{3.6}$$

Comparing this with (3.2) shows that it does indeed give the correct $P_n$. The vector $|n_0\rangle$ represents a coherent state, rather than a state with $n_0$ particles.

The long-time solution should, in most cases, be independent of the initial condition chosen. An example in which this can be seen explicitly is given in section 3.1.2. There are, however, problems in which the initial conditions become important. This is true in particular of problems in which there is a conservation law, which can have an influence on the long-time dynamics. When there are several species of particles, the steady-state solution, if one exists, may be constrained by the initial condition. In the single species problems considered here, the steady state is unique, up to issues connected to parity conservation, which will be discussed later.

Looking ahead to models with spatial dependence, the initial condition can also be important if there are some correlations in the positions of particles at $t = 0$. Any uncorrelated initial conditions produce similar results in the long-time limit.

We want to calculate the expectation value of some quantity which depends on the number of particles, $A(n)$, at some time $t$. As usual, the expectation value is

$$\langle A(t)\rangle = \sum_n A(n)P(n,t). \tag{3.7}$$

This is linear in $P$, as is $|P\rangle$, so $\langle P|\hat{A}|P\rangle$, as used in quantum mechanics, would not produce the correct result. Instead, define the "projection state"

$$\langle| \equiv \langle 0|e^a = \sum_n \frac{1}{n!}\langle n|, \tag{3.8}$$

so that averages are given by $\langle A(t)\rangle = \langle|\hat{A}|P(t)\rangle$. Here, $\hat{A}$ is given by $A(n)$ with $n$ replaced by the number operator $\hat{n} = a^\dagger a$. The inner product with the projection state is the correct thing to do because

$$\begin{aligned}
\langle|\hat{A}|P(t)\rangle &= \sum_n \langle n|\frac{1}{n!}\hat{A}\sum_m P_m|m\rangle \\
&= \sum_{mn} \langle n|\frac{1}{n!}A(m)P_m|m\rangle \\
&= \sum_{mn} A(m)P_m\frac{1}{n!}\langle n|m\rangle \\
&= \sum_{mn} A(m)P_m\frac{1}{n!}n!\delta_{mn}
\end{aligned} \tag{3.9}$$

$$= \sum_n A(n)P_n.$$

The expression for an operator $\hat{A}$ can be simplified by commuting all the creation operators to the left, and using $\langle 0|e^a a^\dagger = \langle 0|e^a$, so $\hat{A}$ can be written using just the destruction operator $a$. Measurable quantities, such as the average number of particles or the standard deviation of the number of particles, may now be calculated. The average number of particles is given by the average of $\hat{n} = a^\dagger a = a$, as $a^\dagger$ produces 1 acting on $\langle 0|e^a$. The standard deviation is $\sigma^2 = \langle n^2 \rangle - \langle n \rangle^2$, where $n^2 = a^\dagger a a^\dagger a = a^\dagger a^\dagger a a + a^\dagger a = a^2 + a$.

The formal solution to the M-equation is $|P(t)\rangle = e^{-\hat{H}t}|P(0)\rangle$, so the time evolution of the average is

$$\langle A(t) \rangle = \langle |\hat{A}e^{-\hat{H}t}|P(0)\rangle. \tag{3.10}$$

The time-evolution should conserve probability. The expectation value of 1 is given by

$$\langle 1 \rangle = \sum_n P_n(t) = \langle 0|e^a e^{-\hat{H}t}|P(0)\rangle. \tag{3.11}$$

Expand $e^{\hat{H}t} = 1 + \hat{H}t + \ldots$, and so if $\langle 0|e^a\hat{H} = 0$, then probability will be conserved. The creation operator $a^\dagger$ gives one acting to the left on the state $\langle 0|e^a$, so that $\langle 0|e^a a^\dagger = 1$. If the operator $\hat{H}$ vanishes when all $a^\dagger$ are commuted to the left and set to 1, then we have probability conservation; all terms beyond the first after the expansion of $e^{\hat{H}t}$ is substituted in (3.11) will vanish.

### 3.1.1 Coherent State Representation

We can now write operators representing measurable quantities in terms of creation and annihilation operators and describe the evolution of the system of particles using the same operators. The next step in the derivation of a field theory is to replace these discrete operators by a continuous variable. This can be done using a coherent state representation, as is used for the harmonic oscillator in quantum mechanics [36]. These are defined by

$$|\phi\rangle = e^{-\frac{1}{2}|\phi|^2} e^{\phi a^\dagger}|0\rangle, \tag{3.12}$$

where $\phi$ is a complex number. Only two properties of these states are needed. First, coherent states are eigenstates of the destruction operator, $a|\phi\rangle = \phi|\phi\rangle$, and they form an overcomplete set, with a resolution of unity

$$1 = \int \frac{\mathrm{d}^2\phi}{\pi} |\phi\rangle\langle\phi|, \tag{3.13}$$

where the integration measure is

$$\mathrm{d}^2\phi = \mathrm{d}(\mathrm{Re}\ \phi)\mathrm{d}(\mathrm{Im}\ \phi). \tag{3.14}$$

The resolution of unity is not an independent result, but rather a consequence of properties of the number representation. It follows from the completeness relation for the number representation,

$$1 = \sum_{mn} \frac{1}{n!} |n\rangle\langle m|\delta_{mn}, \tag{3.15}$$

and an integral representation of the delta function,

$$\delta_{mn} = \frac{1}{\pi m!} \int \mathrm{d}^2\phi e^{-|\phi|^2} \phi^{*m} \phi^n. \tag{3.16}$$

The expectation value of an observable may be written as an integral over coherent states. Using the identity (called the Trotter formula)

$$e^{-\hat{H}t} = \lim_{N\to\infty} (1 - \hat{H}\Delta t)^N, \tag{3.17}$$

with $\Delta t = t/N$, the right hand side of equation (3.10), giving the time evolution of $\langle A\rangle$, can be divided into "slices." Unity, written in terms of a set of coherent states, can be inserted between each pair of slices, to give

$$\begin{aligned} \langle A(t)\rangle \ &= \ \lim_{N\to\infty} \frac{1}{Z} \int \mathrm{d}^2\phi_0 \prod_{j=1}^{N} \left( \int \mathrm{d}^2\phi_j \langle\phi_j|(1 - \hat{H}\Delta t)|\phi_{j-1}\rangle \right) \\ &\quad \times \langle|\hat{A}|\phi_N\rangle\langle\phi_0|P(0)\rangle. \end{aligned} \tag{3.18}$$

The normalization $Z$ can be found from $\langle 1\rangle = 1$ at the end. Rewrite (3.18) as

$$\begin{aligned} \langle A(t)\rangle \ &= \ \lim_{N\to\infty} \frac{1}{Z} \int \mathrm{d}^2\phi_0 \prod_{j=1}^{N} \left[ \int \mathrm{d}^2\phi_j \langle\phi_j|\phi_{j-1}\rangle \left( 1 - \frac{\langle\phi_j|\hat{H}\Delta t|\phi_{j-1}\rangle}{\langle\phi_j|\phi_{j-1}\rangle} \right) \right] \\ &\quad \times \langle|\hat{A}|\phi_N\rangle\langle\phi_0|n_0\rangle. \end{aligned} \tag{3.19}$$

The inner products in this expression are given by

$$\langle\phi_j|\phi_{j-1}\rangle = \langle 0|e^{-\frac{1}{2}|\phi_j|^2}e^{\phi_j^* a}e^{-\frac{1}{2}|\phi_{j-1}|^2}e^{\phi_{j-1}a^\dagger}|0\rangle. \tag{3.20}$$

Using the Baker-Hausdorff identity $e^{A+B} = e^A e^B e^{\left[A,B\right]}$,

$$\begin{aligned}\langle\phi_j|\phi_{j-1}\rangle &= e^{-\frac{1}{2}|\phi_j|^2}e^{-\frac{1}{2}|\phi_{j-1}|^2}\langle 0|e^{\phi_{j-1}a^\dagger}e^{\phi_j^* a}e^{\left[\phi_j^* a,\phi_{j-1}a^\dagger\right]}|0\rangle \\ &= e^{-\frac{1}{2}|\phi_j|^2}e^{-\frac{1}{2}|\phi_{j-1}|^2}e^{\phi_j^*\phi_{j-1}},\end{aligned} \tag{3.21}$$

so that

$$e^{-\frac{1}{2}|\phi_j|^2}\langle\phi_j|\phi_{j-1}\rangle = e^{-\phi_j^*(\phi_j-\phi_{j-1})}e^{-\frac{1}{2}|\phi_{j-1}|^2}. \tag{3.22}$$

This term appears for each time slice. Replace the difference between $\phi$ at neighbouring times with a derivative, $\phi_j - \phi_{j-1} = \frac{\mathrm{d}\phi_j}{\mathrm{d}t}\Delta t + O(\Delta t)^2$. Notice that this means that the derivative is a forward difference. This will become important in the diagrammatic expansion in the next chapter, as it implies that there can be no diagrams with loops.

The other factors appearing in (3.19) are given by

$$\langle|\hat{A}|\phi_N\rangle = \langle|\phi_N\rangle A(\phi_N) \propto e^{-\frac{|\phi_N|^2}{2}+\phi_N}A(\phi_N), \tag{3.23}$$

with $A(\phi)$ given by $\hat{A}(a)$ with $a$ replaced with $\phi$, and by

$$\begin{aligned}\langle\phi_0|P(0)\rangle &= \langle\phi_0|n_0\rangle \\ &= \langle 0|e^{-\frac{1}{2}|\phi_0|^2}e^{\phi_0^* a}e^{-n_0}e^{n_0 a^\dagger}|0\rangle \\ &= e^{-\frac{1}{2}|\phi_0|^2}e^{-n_0}\langle 0|e^{n_0 a}e^{\phi a}e^{\left[\phi_0 a,n_0 a^\dagger\right]} \\ &= e^{-\frac{1}{2}|\phi_0|^2+n_0\phi_0^*}e^{-n_0}\end{aligned} \tag{3.24}$$

so that

$$\begin{aligned}\langle A\rangle &= \lim_{N\to\infty}\frac{1}{Z}\left(\prod_{j=0}^{N}\int \mathrm{d}^2\phi_j e^{\phi_N+n_0\phi_0^*-|\phi_0|^2-\sum_{j=1}^{N}\Delta t\phi_j^*\frac{\partial\phi_j}{\partial t}}\right) \\ &\quad\times\prod_{j=1}^{N}(1-H(\phi,\phi^*)\Delta t)A(\phi).\end{aligned} \tag{3.25}$$

In (3.19), $H(a, a^\dagger)$ appears between states $\langle\phi_j|$ and $|\phi_{j-1}\rangle$. If $H$ is written in normal order, with creation operators to the right, then $a$ can be replaced by $\phi_{j-1}$, as $|\phi_{j-1}\rangle$ is a right eigenstate of $a$, and $a^\dagger$ by $\phi_j^*$, after acting on $\langle\phi_j|$. We will be dropping terms in $H\Delta t$ proportional to $(\Delta t)^2$, and so the difference between $\phi_j$ and $\phi_{j-1}$ will be dropped. $H(\phi, \phi^*)$ is therefore $H(a, a^\dagger)$ with $a$ and $a^\dagger$ replaced by $\phi$ and $\phi^*$.

Using $e^{-H\Delta t} = 1 - H\Delta t + O(\Delta t)^2$, we get

$$\langle A\rangle = \lim_{N\to\infty} \frac{1}{Z}\left(\prod_{j=0}^{N}\int \mathrm{d}^2\phi_j e^{\phi_N + n_0\phi_0^* - |\phi_0|^2 - \sum_{j=1}^{N}\Delta t\phi_j^*\frac{\partial\phi_j}{\partial t} - H\Delta t}\right) A(\phi). \tag{3.26}$$

The continuum limit, $N \to \infty$, can now be taken,

$$\langle A\rangle = \frac{1}{Z}\int \mathrm{D}\phi^*\mathrm{D}\phi A(\phi)e^{-S} \tag{3.27}$$

with

$$S = \int_0^t \mathrm{d}t'\left(\phi^*(t')\frac{\partial\phi(t')}{\partial t'} + H\right) - n_0\phi^*(0) - \phi(t) \tag{3.28}$$

and

$$Z = \int \mathrm{D}\phi^*\mathrm{D}\phi e^{-S}. \tag{3.29}$$

It is often useful to make the change of variables $\bar{\phi} = \phi^* - 1$ but in some situations this can cause problems. This change of variables may obscure a symmetry of the system, which may be violated by a later approximation. This is the case in the system in which new offspring particles are created in pairs, discussed in this thesis.

### 3.1.2 Decay

A simple example of the above is given by the decay of a collection of independent particles, as in radioactive decay. The treatment here follows Mattis and Glasser's example [37], where it is used as a demonstration of field theoretic techniques. This problem provides a simple example of how to use this method in a case where the answer is already known, and also provides an example in which the lack of dependence of the long-time solution on the initial condition can be seen. The transition rates are given by

$$W_{n\to n'} = w(n+1)\delta_{n,n'+1} \tag{3.30}$$

so that particles vanish from the system at a rate $w$, independent of the number of particles; each particle has a probability $w$ per unit time of decaying. The probability of finding the system with $n$ particles increases due to systems with $n+1$ particles losing a particle to decay, while this probability decreases due to systems with $n$ particles losing a particle to decay. The M-equation is then

$$\frac{\mathrm{d}P(n,t)}{\mathrm{d}t} = w(n+1)P(n+1,t) - wnP(n,t). \tag{3.31}$$

The time evolution operator for the system is

$$-\hat{H} = w(a - a^\dagger a). \tag{3.32}$$

This form of $\hat{H}$ produces the correct M-equation, as

$$\begin{aligned} \frac{\mathrm{d}|P\rangle}{\mathrm{d}t} &= -H|P\rangle = w(a - a^\dagger a)|P\rangle \\ &= wa\sum_n^\infty P_n|n\rangle - wa^\dagger a\sum_n^\infty P_n|n\rangle \\ &= w\sum_n^\infty nP_n|n-1\rangle - w\sum_n^\infty nP_n|n\rangle. \end{aligned} \tag{3.33}$$

Taking an inner product with any state $|m\rangle$ then gives

$$\langle m|\frac{\mathrm{d}}{\mathrm{d}t}\sum_n^\infty P_n|n\rangle = w\sum_n^\infty nP_n\langle m|n-1\rangle - w\sum_n^\infty nP_n\langle m|n\rangle \tag{3.34}$$

so that

$$\frac{\mathrm{d}P_m}{\mathrm{d}t} = w(m+1)P_{m+1} - wmP_m, \tag{3.35}$$

as desired. Introducing the continuous variable $\phi$ by working through the procedure described in section 3.1 then produces

$$S = \int_0^t \mathrm{d}t' \left[\phi^*(t')\frac{\partial\phi(t')}{\partial t'} + w(\phi^*(t')\phi(t') - \phi(t))\right] - n_0\phi^*(0) - \phi(t) \tag{3.36}$$

or, after changing variables,

$$S = \int_0^t \mathrm{d}t' \left[\bar{\phi}(t')\frac{\partial\phi(t')}{\partial t'} + w\bar{\phi}(t')\phi(t') + \frac{\partial\phi(t')}{\partial t'}\right] - n_0(\bar{\phi}(0)+1) - \phi(t). \tag{3.37}$$

Integrating the partial derivative then cancels with $\phi(t)$ outside the integral, to give

$$S = \int_0^t \mathrm{d}t' \left[\bar{\phi}(t')\frac{\partial\phi(t')}{\partial t'} + w\bar{\phi}(t')\phi(t')\right] - n_0(\bar{\phi}(0)+1) - \phi(0). \tag{3.38}$$

The factor $e^{-n_0}$ can be absorbed into the normalization factor of $Z$, and so will be dropped.

If we take the expression for the expectation value of the number of particles,

$$\langle n(t)\rangle = \langle\phi(t)\rangle = \frac{1}{Z}\int \mathrm{D}\bar{\phi}\mathrm{D}\phi\phi(t)e^{-\int_0^t \mathrm{d}t'\left[\bar{\phi}(t')\frac{\partial\phi(t')}{\partial t'}+w\bar{\phi}(t')\phi(t')\right]-n_0\bar{\phi}(0)-\phi(0)} \tag{3.39}$$

and do the $\mathrm{D}\bar{\phi}$ integral, which is over the imaginary direction, we get a delta functional:

$$\langle\phi(t)\rangle = \frac{1}{Z}\int \mathrm{D}\phi\,\delta\left[\frac{\partial\phi}{\partial t} + w\phi(t) - n_0\delta(t)\right]. \tag{3.40}$$

This means that $\langle n\rangle$ may be calculated by integration over all solutions of

$$\frac{\partial\phi}{\partial t} + w\phi(t) - n_0\delta(t) = 0. \tag{3.41}$$

There is only one solution, the usual exponential decay, so this has indeed produced the correct answer.

It is actually easier in this problem to go back to an earlier form,

$$\langle A\rangle = \langle 0|e^a A(a)e^{wt(a-a^\dagger a)}|P(0)\rangle \tag{3.42}$$

to evaluate averages. Using the expressions for the average number of particles and the fluctuation in number of particles, it is an exercise in commutation to show $\langle n(t)\rangle = n_0e^{-wt}$, and $\sigma^2(t) = n_0e^{-wt}$. With a different initial condition, exactly $n_0$ particles, $|P(0)\rangle = (a^\dagger)^{n_0}|0\rangle$, so that $\langle n(t)\rangle = n_0e^{-wt}$, and $\sigma^2(t) = n_0e^{-wt}(1-e^{-wt})$. Notice that the average numbers of particles with these two different initial conditions are the same and that at long times the fluctuations in number become the same.

### 3.1.3 Pair Annihilation

If the particles are taken to annihilate in pairs, so that the reaction is

$$A + A \to \emptyset \tag{3.43}$$

at a rate $\lambda$, then the M-equation is

$$\frac{\mathrm{d}P(n,t)}{\mathrm{d}t} = \lambda(n+1)(n+2)P(n+2,t) - \lambda n(n-1)P(n,t). \tag{3.44}$$

As usual, the first term gives the increase in the probability of finding $n$ particles due to annihilation of two particles in $n+2$ particle systems, while the second term gives the decrease in probability of finding $n$ particles. The annihilation of any pair of particles is independent, so the rate at which a pair annihilates in an $n$ particle system should be proportional to $n(n-1)$. Represented as creation and destruction operators, this gives a time-evolution operator

$$-\hat{H} = \lambda(a^2 - a^{\dagger 2}a^2). \tag{3.45}$$

The term appearing in the "action" $S$ is

$$S_2 = -\lambda(\phi^2 - \phi^{*2}\phi^2). \tag{3.46}$$

If the shift $\bar{\phi} = \phi^* - 1$ can be made, then

$$S_2 = \lambda(\bar{\phi}^2\phi^2 + 2\bar{\phi}\phi^2). \tag{3.47}$$

In the simple pair annihilation problem, all terms may be treated exactly, and so this shift may be done. In the problem with particle branching as well, some approximations must be made, and so the shift should not be done. This will be discussed in more detail in chapter 4.

### 3.1.4 Branching

One additional single site reaction will be treated in this thesis, one in which a particle branches into several. If a single particle may create $m$ offspring at a rate $\mu$, then the M-equation contains a term

$$\frac{\mathrm{d}P(n)}{\mathrm{d}t} = \mu(n-m)P(n-m) - \mu n P(n). \tag{3.48}$$

The term in the action corresponding to this reaction is

$$S_b = \mu\left[1 - \phi^{*m}\right]\phi^*\phi. \tag{3.49}$$

## 3.2 One (or More) Spatial Dimension(s)

All of the above has been for a single site, or zero spatial dimensions. These processes can easily be extended to a lattice in one or more spatial dimensions. The state of the system is represented by the number of particles at each lattice site. There must now be creation and annihilation operators $a_i^\dagger$ and $a_i$ for each lattice site, so the vector representing the state of the system with $..., n_{i-1}, n_i, n_{i+1}, ... \equiv n_i$ particles is

$$|\{n_i\}\rangle = \prod_i (a_i^\dagger)^{n_i} |0\rangle. \tag{3.50}$$

The single site interactions introduced above can occur at each lattice site, and so should be summed over all lattice sites. The fields $\phi$ and $\bar{\phi}$ now become functions of position, and the action is integrated over all space, with contributions due to every kind of reaction from each lattice site.

New kinds of behaviour are now possible, as particles can now move from one lattice site to another, by diffusion or ballistic transport. Only diffusion will be described here. The simplest way to obtain normal diffusion is to have particles hop from site to nearest neighbour site. To derive the term appearing in $S$ due to diffusion, focus on a single site $i$. The probability of finding a particle at this site may change due to particles moving into site $i$ from its nearest neighbours, sites $i+1$ and $i-1$, each at a rate $D/(\Delta t)^2$, or due to particles moving out of site $i$ to either side, which occurs at a rate $2D/(\Delta t)^2$. The M-equation for this probability is thus

$$\begin{aligned} \frac{\mathrm{d}P(n_i)}{\mathrm{d}t} &= D\Big[(n_{i+1}+1)P(\ldots, n_i - 1, n_{i+1}+1, \ldots) \\ &\quad +(n_{i-1})P(\ldots, n_{i-1}+1, n_i - 1, \ldots) \\ &\quad -2n_i P(\ldots, n_{i-1}, n_i, n_{i+1}, \ldots)\Big]. \end{aligned} \tag{3.51}$$

This will generate a term in $S$ of the form $S_D = -D\bar{\phi}\nabla^2\phi$.

With both pair annihilation reactions and diffusion, the "action" is

$$\begin{aligned} S = \int \mathrm{d}^d x \Bigg[ \int_0^t \mathrm{d}t' \Bigg( & \bar{\phi}(t')\frac{\partial \phi(t')}{\partial t'} - D\bar{\phi}(t')\nabla^2\phi(t') + 2\lambda\bar{\phi}(t')\phi^2(t') \\ & + \lambda\bar{\phi}^2(t')\phi^2(t')\Bigg) - n_0\bar{\phi}(t)\Bigg]. \end{aligned} \tag{3.52}$$

With pair annihilation, branching, and diffusion, the action is

$$S = \int \mathrm{d}^d x \Big[ \int_0^\tau \mathrm{d}t [\hat{\phi}(\mathbf{x},t)[\partial_t - D_A \nabla^\sigma]\phi(\mathbf{x},t) - \lambda[1-\hat{\phi}(\mathbf{x},t)^2]\phi(\mathbf{x},t)^2 + \mu[1-\hat{\phi}(\mathbf{x},t)^2]\hat{\phi}(\mathbf{x},t)\phi(\mathbf{x},t)] - \phi(\mathbf{x},\tau) - n_0\hat{\phi}(\mathbf{x},0)\Big], \quad (3.53)$$

where $\phi^*$ is rewritten as $\hat{\phi}$, but the shift $\hat{\phi} \to 1 + \bar{\phi}$ has not been done, for reasons which will be discussed in chapter 4.

### 3.2.1 Anomalous Diffusion

If the motion of particles is given by a Lévy flight rather than normal diffusion, the M-equation for the probability is modified from that in equation (3.51) to include a sum over all lattice sites. The terms on the right hand side are weighted by a factor given by the real space Lévy distribution in the distance between the beginning and final lattice sites, so that they fall off as $r^{-d-\sigma}$ for large $r$. The effect of this change on the action can be seen by considering the anomalous diffusion equation derived in section 2.3.4. This differs from the normal diffusion equation simply by substitution of $D_A\nabla^\sigma$ for $D\nabla^2$, and this is also true for the term in the action due to anomalous diffusion. Anomalous diffusion thus adds a term $S_{D_A} = -D_A\bar{\phi}\nabla^\sigma\phi$ to the action. This term will not be written in the rest of this chapter, where the Langevin equation describing these models is derived, but may easily be restored when necessary.

## 3.3 Langevin Equation for the Annihilation Process

In this section, we will derive the equation giving the average density of particles in the system and the correct form of the noise term to properly reproduce the microscopic dynamics of the system.

The average of any quantity is given by equation (3.27), with the "action" $S$ for the annihilation process given by equation (3.52). The observable $A$ corresponding to

the number of particles is, as before, given by $A = n = \phi$, so we have, for this process,

$$\langle n(t)\rangle = \frac{1}{Z}\int \mathrm{D}\bar{\phi}\mathrm{D}\phi\phi(t)e^{-S} \tag{3.54}$$

$$= \frac{1}{Z}\int \mathrm{D}\bar{\phi}\mathrm{D}\phi\phi(t)\exp\Big\{-\int \mathrm{d}^d x\int \mathrm{d}t\Big(\bar{\phi}(t')\frac{\partial\phi(t')}{\partial t'} - D\bar{\phi}(t')\nabla^2\phi(t') + 2\lambda\bar{\phi}(t')\phi^2(t') + \lambda\bar{\phi}^2(t')\phi^2(t')\Big) - n_0\bar{\phi}(0)\Big\} \tag{3.55}$$

We can try to integrate over $\bar{\phi}$, as in section 3.1.2, to find a differential equation describing the evolution of the number of particles in the system. However, the term $\lambda\bar{\phi}^2\phi^2$ in (3.55) is quadratic in $\bar{\phi}$, and so the integral over $\bar{\phi}$ cannot be done immediately. Instead, we can use the identity, valid for a pure imaginary variable $\zeta$,

$$\int \mathrm{d}\zeta \frac{e^{-\zeta\bar{\phi}}e^{\zeta^2/4\lambda\phi^2}}{2\phi\sqrt{\lambda\pi}} = \frac{1}{2\phi\sqrt{\lambda\pi}}\int \mathrm{d}\zeta e^{(\zeta-2\lambda\phi^2\bar{\phi})^2/4\lambda\phi^2 - \lambda\phi^2\bar{\phi}^2} = e^{-\lambda\phi^2\bar{\phi}^2}, \tag{3.56}$$

to rewrite (3.55) as

$$\langle n(t)\rangle = \frac{1}{Z}\int \mathrm{D}\bar{\phi}\mathrm{D}\phi\mathrm{D}\zeta\phi(t)\exp\Big\{\int \mathrm{d}^d x\int \mathrm{d}t\Big(\bar{\phi}(t')\frac{\partial\phi(t')}{\partial t'} - D\bar{\phi}(t')\nabla^2\phi(t') + 2\lambda\bar{\phi}(t')\phi^2(t') - \bar{\phi}(t')\zeta\Big) - n_0\bar{\phi}(0)\Big\}P'[\zeta] \tag{3.57}$$

with

$$P'[\zeta] \propto e^{\int \mathrm{d}x\mathrm{d}t\zeta^2/4\lambda\phi^2}. \tag{3.58}$$

Here, $\zeta$ is now a random function; the identity (3.56) has been used at each point $(x,t)$. The functional $P[\zeta]$ gives the weight of each function $\zeta$. Making a change of variables $\frac{\zeta}{\phi} \to \zeta$ turns this into

$$\langle n(t)\rangle = \frac{1}{Z}\int \mathrm{D}\bar{\phi}\mathrm{D}\phi\mathrm{D}\zeta\phi(t)\exp\Big\{\int \mathrm{d}^d x\Big[\int \mathrm{d}t\Big(\bar{\phi}(t')\frac{\partial\phi(t')}{\partial t'} - D\bar{\phi}(t')\nabla^2\phi(t') + 2\lambda\bar{\phi}(t')\phi^2(t') - \bar{\phi}(t')\phi(t')\zeta\Big) - n_0\bar{\phi}(0)\Big]\Big\}P[\zeta] \tag{3.59}$$

with

$$P[\zeta] = \frac{e^{\int \mathrm{d}x\mathrm{d}t\zeta^2/4\lambda}}{2\sqrt{\lambda\pi}}. \tag{3.60}$$

The probability of finding a value $\zeta$ at a single point $(x,t)$ is given by

$$P(\zeta(x,t)) = \frac{e^{\zeta^2/4\lambda}}{2\sqrt{\lambda\pi}}. \tag{3.61}$$

The integral in equation (3.56) only converges for $\zeta$ pure imaginary, so that if it is interpreted as a stochastic noise, the noise function takes on a random purely imaginary value, at every point in space and time. The fact that the noise term is imaginary is why simply adding a real noise to the mean field equation, as one might expect, will not produce the correct results.

The correlation between the noise function at different points $(x,t)$ and $(x',t')$ can be calculated from the probability distribution (3.60). For $x \neq x'$ or $t \neq t'$, the noise is uncorrelated, as

$$\begin{aligned} \langle \zeta(x,t)\zeta(x',t') \rangle &= \frac{1}{4\lambda\pi} \int_{-i\infty}^{i\infty} \mathrm{d}\zeta(x,t)\mathrm{d}\zeta(x',t')\zeta(x,t)\zeta(x',t') \\ &\quad \times e^{\zeta^2(x,t)/4\lambda} e^{\zeta^2(x',t')/4\lambda} \\ &= 0. \end{aligned} \tag{3.62}$$

This is true as long as either $x \neq x'$ or $t \neq t'$. The noise correlation for $x = x'$ and $t = t'$ is given by

$$\langle \zeta(x,t)\zeta(x,t) \rangle = \frac{1}{2\sqrt{\lambda\pi}} \int_{-i\infty}^{i\infty} \mathrm{d}\zeta(x,t)\zeta^2(x,t) e^{\zeta^2(x,t)/4\lambda} = -2\lambda. \tag{3.63}$$

In discretized space, the noise correlation is thus given by

$$\langle \zeta(x,t)\zeta(x',t') \rangle = -2\lambda \delta_{x,x'}\delta_{t,t'} \tag{3.64}$$

and with $t$ and $x$ continuous,

$$\langle \zeta(x,t)\zeta(x',t') \rangle = -2\lambda \delta(x-x')\delta(t-t'). \tag{3.65}$$

The imaginary nature of the noise function produces the negative sign in front of the correlator. It will turn out that only this two-point correlation will be needed in the rest of the calculation.

The integral over $\bar{\phi}$ can now be done to produce

$$\langle n(t) \rangle = \frac{1}{Z} \int \mathrm{D}\zeta \int \mathrm{D}\phi \; \phi(t) \; \delta\left[ \frac{\partial \phi}{\partial t'} - D\nabla^2\phi + 2\lambda\phi^2 - \phi\zeta - n_0\delta(t') \right] P[\zeta]. \tag{3.66}$$

If the integral over $\mathrm{D}\phi$ is done, then

$$\langle n(t) \rangle = \int \mathrm{D}\zeta \phi_{\mathrm{sol'n}}(t) P[\zeta] \tag{3.67}$$

where $P[\zeta]$ is the probability distribution for a noise history (3.60), and $\phi_{\mathrm{sol'n}}(t)$ solves

$$\frac{\partial\phi}{\partial t'} - D\nabla^2\phi + 2\lambda\phi^2 - \phi\zeta - n_0\delta(t') = 0. \tag{3.68}$$

This all means that to calculate $\langle n(t)\rangle$, we need to solve (3.68) for a given noise history $\zeta(x',t')$, and then average over all possible functions $\zeta$, weighted by $P[\zeta]$. A solution to (3.68) can be written down in terms of $G(x,t)$, the Green function for the diffusion equation:

$$\begin{aligned}\phi &= \int \mathrm{d}x' G(x-x',t)n_0 \\ &\quad + \int \mathrm{d}x'\mathrm{d}t' G(x-x',t-t')\Big(-2\lambda\phi^2(x',t') + \phi(x',t')\zeta(x',t')\Big).\end{aligned} \tag{3.69}$$

In $d$ spatial dimensions, the Green function is

$$G(\mathbf{x},t) = \left(\frac{1}{4\pi Dt}\right)^{d/2} e^{-x^2/4Dt}\Theta(t). \tag{3.70}$$

Fourier and Laplace transforming this gives the Green function in $(\mathbf{k},t)$ and $(\mathbf{k},\omega)$ space:

$$G(\mathbf{k},t) = e^{-Dk^2t}\Theta(t), \tag{3.71}$$

$$G(\mathbf{k},\omega) = \frac{1}{Dk^2 - i\omega}. \tag{3.72}$$

A series solution can now be developed by iteration: first, neglecting the noise, substitute the solution for $\lambda = 0$ into the interaction term, and then repeat, to produce

$$\begin{aligned}\phi &= \int \mathrm{d}x' G(x-x',t)n_0 + \int \mathrm{d}x'\mathrm{d}t' G(x-x',t-t') \\ &\quad \times(-2\lambda)\int \mathrm{d}x_1 G(x'-x_1,t')n_0 \int \mathrm{d}x_2 G(x'-x_2,t')n_0 + \ldots \quad .\end{aligned} \tag{3.73}$$

To avoid writing many formulae like this, a diagrammatic notation is used. Each Green function is represented as a line, with time going to the left, and so the second term in the series (3.73) is represented by

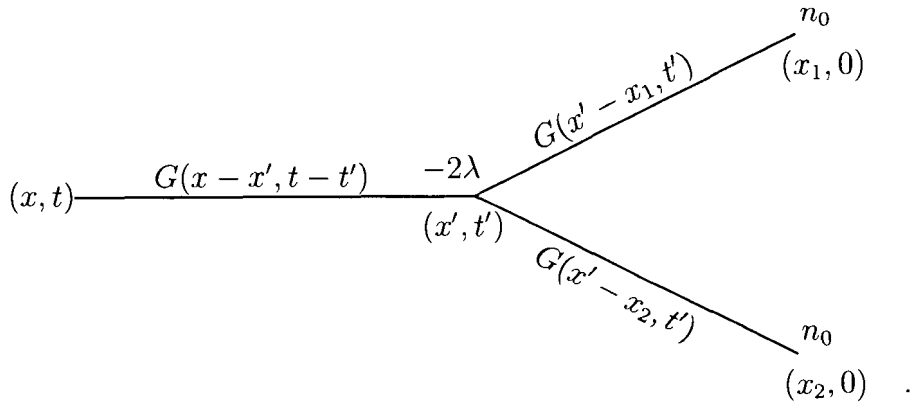


Without the noise, the complete set of diagrams is

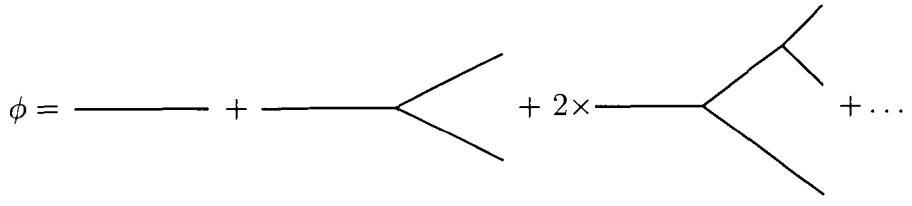


The spatial integrals over the Green functions give 1, so to order $\lambda^2$,

$$\phi(t) \approx n_0 - 2\lambda n_0^2 \int_0^t \mathrm{d}t' + 2(2\lambda)^2 n_0^3 \int_0^t \mathrm{d}t' \int_0^{t'} \mathrm{d}t_1 = n_0(1 - 2\lambda n_0 t + (2\lambda n_0 t)^2). \quad (3.74)$$

But without noise, (3.68) is just the mean field equation discussed in section 1.1.1, so the sum of this set of diagrams is just the solution

$$\phi = \frac{n_0}{1 + 2n_0\lambda t} \quad (3.75)$$

to the noiseless mean field equation.

The noise term adds some additional diagrams. Any term with just one factor of $\zeta$ will vanish when integrated over $\zeta$ (as $\langle\zeta\rangle = 0$), so the first term with a non-zero contribution is

$$-2\lambda \int \mathrm{d}x_1 \mathrm{d}t_1 G(x - x_1, t - t_1) \int \mathrm{d}x_2 \int \mathrm{d}t_2 G(x_1 - x_2, t_1 - t_2)\zeta(x_2, t_2)$$
$$\times \int \mathrm{d}x_3 G(x_2 - x_3, t_2) n_0 \int \mathrm{d}x_4 \mathrm{d}t_4 G(x_1 - x_4, t_1 - t_4)\zeta(x_4, t_4)$$
$$\times \int \mathrm{d}x_5 G(x_4 - x_5, t_4) n_0 \tag{3.76}$$

which is represented by the diagram

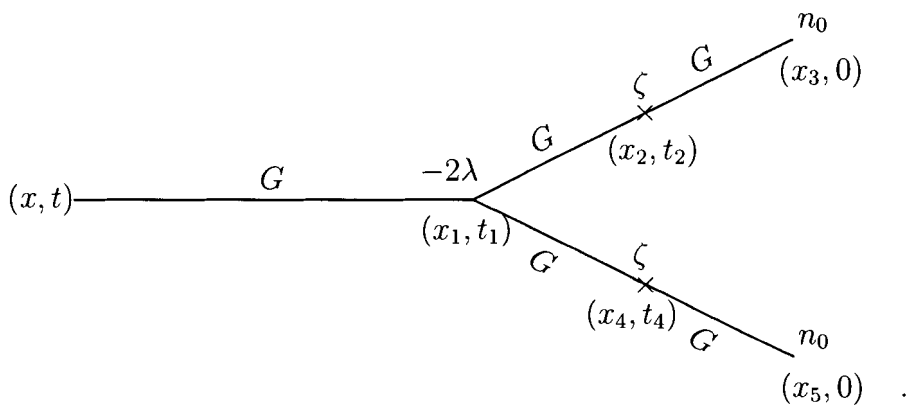


The full expansion of the series is then (dropping the terms which will give zero when integrated over $\zeta$)

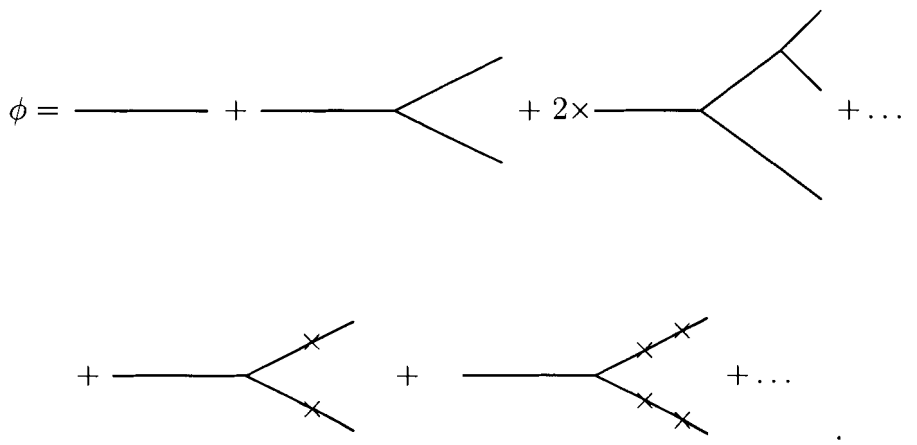

When the diagrams in the second line are integrated over $\zeta$, the delta function in the noise-noise correlation function (3.65) forces the noise factors to be at the same point, so that, for example, the diagram representing (3.76) becomes

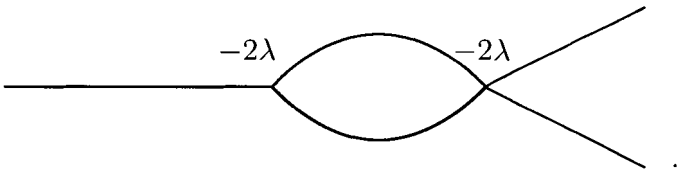


Many of these diagrams with loops contain divergent parts. These must be handled using renormalization group techniques. This calculation will be presented in the next chapter.

# Chapter 4

# Renormalization Group Calculations

In this chapter we will give the renormalization group calculations done on both models studied here. In the case of an annihilation reaction alone both the power law decay of the number of particles and the amplitude of this power law may be calculated. Our calculation of these quantities is given in some detail. When a branching reaction is added, the calculation becomes more difficult. Here, the most important result is the identification of a critical Lévy exponent at which an absorbing phase at finite branching rate becomes possible. This is calculated in section 4.2. The result for the exponent governing the steady-state density is also given in this section.

## 4.1 Annihilation Reaction

In this section we will develop a perturbative solution to the Langevin equation derived in the previous chapter and calculate the average density $n(t)$ of particles remaining in the system as a function of time. Both the exponent and the amplitude of the power-law decay of the density will be calculated. Some terms which appear in this expansion are divergent, and so renormalization group techniques will be used to calculate finite physical quantities. The divergent integrals will be regulated using dimensional regularization: divergent integrals in the dimension of interest are replaced

by integrals in $d$ dimensions. This makes it possible to isolate the divergent quantities in an expansion in $\epsilon = d_c - d$, where $d_c$ is the dimension at which the integrals considered first become divergent.

The procedure used here differs from usual renormalization group calculations in some details and follows that used by Lee [9] in his study of the annihilation reaction with normal diffusion. Since the initial density $n_0$ is not small, it must be included to all orders, as was observed in reference [38]. This can be done using a response function formalism described by Janssen [39] and de Dominicis [40].

To implement the renormalization group, we will first calculate the flow function $\beta$ for the annihilation rate. This can be done to all orders, due to the simple way in which the annihilation rate is renormalized by fluctuations. A dimensionless renormalized annihilation rate can then be defined, and its fixed points can be determined from $\beta$. As usual in a renormalization group calculation, an arbitrary momentum scale $\kappa$ is introduced at this point. Any physical result cannot depend on this arbitrary scale, and so a renormalization group equation can be written to express the lack of dependence of $n(t)$ on $\kappa$. The solution to this equation relates the observable density at one time $t$ to that at another time $t'$. A perturbative approach is then used to calculate this density, in which the number of loops in the diagrams calculated determines the order of the expansion. In this calculation, divergent terms that appear at each order in the number of loops are cancelled by terms coming from the tree diagram calculation when the bare annihilation rate is replaced by the renormalized annihilation rate. We will be calculating the amplitude of the density decay to next-to-leading order, so only the first two terms need be retained in an expansion.

Before beginning the calculation, it is useful to examine the dimensions of quantities appearing in the theory. In terms of a momentum scale $\kappa$, the engineering dimensions can be chosen to be

$$[\phi] = [\kappa^d], \qquad [x] = [\kappa^{-1}], \qquad [Dt] = [\kappa^{-\sigma}], \qquad [\lambda] = [\kappa^{\sigma - d}]. \tag{4.1}$$

Here the notation $[\cdot]$ means "the dimension of the quantity $\cdot$." There is some choice in the definition of these dimensions, as in the field theory the dimensions of the fields $\phi$ and $\overline{\phi}$ may be changed together. However, this choice is the most natural, in keeping

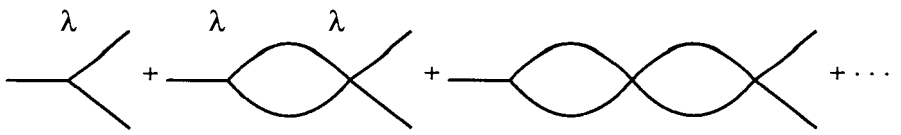


Figure 4.1: The diagrams which contribute to the renormalized annihilation rate $\lambda_R$.

with the interpretation of $\langle\phi\rangle$ as the density of particles. Since the diffusion constant $D$ and the time $t$ never appear alone, but only in the combination $Dt$, the diffusion constant will be absorbed into the time and will not appear in this chapter. It may be restored in any formula by replacing $t$ with $Dt$. It will reappear in the next chapter in which simulations are discussed, as it is varied for some of the simulations.

The annihilation rate becomes dimensionless when $d = d_c = \sigma$, so the parameter $\epsilon$ for an expansion about the critical dimension is $\epsilon = \sigma - d$. The dimensionless coupling constant (or annihilation rate) is then $g = \kappa^{-\epsilon}\lambda$. We will be working in Fourier-Laplace transformed coordinates $(\mathbf{k}, s)$, with $[s] = [t^{-1}]$. A renormalization point at a momentum scale $\kappa$ can then be chosen by evaluating quantities at $(\mathbf{k}, s) = (\mathbf{0}, \kappa^\sigma)$.

### 4.1.1 Renormalized Annihilation Rate

The renormalized annihilation rate can be calculated by examining truncated versions of the diagrams shown in figure 4.1, and is given by the sum of integrals

$$\lambda_R(\mathbf{k}, t) = \lambda\delta(t) - I(\mathbf{k}, t) + \int \mathrm{d}t' I(\mathbf{k}, t - t')I(\mathbf{k}, t') + \ldots \tag{4.2}$$

with

$$I(\mathbf{k}, t) = 2\int \frac{\mathrm{d}^d\mathbf{k}_1}{(2\pi)^d}\int \frac{\mathrm{d}^d\mathbf{k}_2}{(2\pi)^d}(2\pi)^d\delta(\mathbf{k} - \mathbf{k}_1 - \mathbf{k}_2)e^{-k_1^\sigma t}e^{-k_2^\sigma t}. \tag{4.3}$$

The Langevin equation or field theory here is simple enough that this sum represents all diagrams with one leg to the left and two to the right. Only diagrams of this form may be constructed using the two verticies available.

Since we have chosen to renormalize at $(\mathbf{k}, s) = (\mathbf{0}, \kappa^\sigma)$, we can evaluate this integral at $\mathbf{k} = \mathbf{0}$. After integration over $\mathbf{k}_2$, making use of the $\delta$-function, the

integrand depends only on the magnitude of $\mathbf{k}_1$, and so the integral can be written as

$$I(\mathbf{k}=\mathbf{0},t) = \frac{2}{(2\pi)^d} K_d \int \mathrm{d}k_1 k_1^{d-1} e^{-2k_1^\sigma t}. \tag{4.4}$$

Here, $K_d$ is the surface area of a sphere in $d$ dimensions, $K_d = \frac{2\pi^{d/2}}{\Gamma(d/2)}$. Performing the integral gives

$$\begin{aligned} I &= \frac{1}{\sigma}\frac{2^{1-d/\sigma}}{(2\pi)^d} K_d t^{-d/\sigma} \int \mathrm{d}u u^{\frac{d}{\sigma}-1} e^{-u} && (4.5)\\ &= Ct^{-d/\sigma} && (4.6) \end{aligned}$$

with

$$C = \frac{1}{\sigma}\frac{2^{2-d/\sigma}}{(4\pi)^{d/2}}\frac{\Gamma(\frac{d}{\sigma})}{\Gamma(\frac{d}{\sigma})}. \tag{4.7}$$

The Laplace transformed annihilation rate

$$\lambda_R(\mathbf{k}=\mathbf{0},s) = \int \mathrm{d}t \lambda_R(\mathbf{k}=\mathbf{0},t) e^{-st} \tag{4.8}$$

is a geometric sum, with the multiplicative factor given by the Laplace transform of $I$:

$$I(\mathbf{k}=\mathbf{0},s) = \int \mathrm{d}t C t^{-d/\sigma} e^{-st} = C\Gamma\left(\frac{\epsilon}{\sigma}\right) s^{-\epsilon/\sigma}. \tag{4.9}$$

The Laplace transformation makes it possible to sum all the diagrams to give

$$\lambda_R(\mathbf{0},s) = \frac{\lambda}{1+\lambda C\Gamma(\frac{\epsilon}{\sigma})s^{-\epsilon/\sigma}}. \tag{4.10}$$

We now need to choose a momentum $\kappa$ as the renormalization point. The dimensionless bare annihilation rate is, as discussed above, $g = \kappa^{-\epsilon}\lambda$, and the dimensionless renormalized coupling is $g_R = \kappa^{-\epsilon}\lambda_R$. From the dimensional analysis earlier, we should replace $s$ by $\kappa^\sigma$, so the dimensionless renormalized annihilation rate is

$$g_R = \frac{\kappa^{-\epsilon}\lambda}{1+\kappa^{-\epsilon}\lambda C\Gamma(\frac{\epsilon}{\sigma})}. \tag{4.11}$$

As the scale at which we renormalize changes, this coupling constant changes. The dependence of the coupling on the momentum is given by a flow function, conventionally called $\beta$. The flow function for the renormalized annihilation rate is

$$\beta = \kappa\frac{\partial g_R}{\partial \kappa} = -\epsilon g_R + \epsilon C\Gamma\left(\frac{\epsilon}{\sigma}\right) g_R^2. \tag{4.12}$$

This has a fixed point at $g_R = 0$, and a non-trivial fixed point at

$$g_R = g_R^* \equiv \frac{1}{C\Gamma(\frac{\epsilon}{\sigma})}. \tag{4.13}$$

The fixed point at $g_R^*$ is the stable one for $d < \sigma$.

The renormalized and unrenormalized dimensionless couplings are then related, using (4.11), by

$$g = \frac{g_R}{1 - \frac{g_R}{g_R^*}} \approx g_R + \frac{g_R^2}{g_R^*}. \tag{4.14}$$

### 4.1.2 Renormalization Group Equation

The choice of the point $\kappa$ at which to renormalize should not affect physical results, so density is independent of $\kappa$

$$\left[\kappa\frac{\partial}{\partial\kappa} + \beta(g_R)\frac{\partial}{\partial g_R}\right] n_R(t, g_R, n_0, \kappa) = 0, \tag{4.15}$$

and dimensional analysis gives

$$\kappa\frac{\partial}{\partial\kappa}n_R = \left[\sigma t\frac{\partial}{\partial t} - dn_0\frac{\partial}{\partial n_0}, +d\right] n_R \tag{4.16}$$

so that

$$\left[\sigma t\frac{\partial}{\partial t} - dn_0\frac{\partial}{\partial n_0} + \beta(g_R)\frac{\partial}{\partial g_R} + d\right] n_R = 0 \tag{4.17}$$

or

$$\left[\frac{\partial}{\partial \ln t} - \frac{dn_0}{\sigma}\frac{\partial}{\partial n_0} + \frac{\beta(g_R)}{\sigma}\frac{\partial}{\partial g_R} + \frac{d}{\sigma}\right] n_R = 0. \tag{4.18}$$

This differential equation can be solved using the method of characteristics to relate $n_R(t)$ to that at an earlier time. The total derivative of $n_R$ is

$$\frac{\mathrm{d}n_R}{\mathrm{d}\ln t} = \frac{\partial n_R}{\partial \ln t} + \frac{\partial n_R}{\partial n_0}\frac{\mathrm{d}n_0}{\mathrm{d}\ln t} + \frac{\partial n_R}{\partial g_R}\frac{\mathrm{d}g_R}{\mathrm{d}\ln t}. \tag{4.19}$$

Choose a path through $(n_0, g_R)$ space parametrised by $t$ such that

$$\frac{\mathrm{d}n_0}{\mathrm{d}\ln t} = \frac{dn_0}{\sigma} \tag{4.20}$$

and

$$\frac{\mathrm{d}g_R}{\mathrm{d}\ln t} = \frac{\beta(g_R)}{\sigma}. \tag{4.21}$$

Inserting (4.19), (4.20) and (4.21) into (4.18),

$$\frac{\mathrm{d}n_R}{\mathrm{d}\ln t} = -\frac{dn_R}{\sigma}. \tag{4.22}$$

The solution to the set of equations (4.20)—(4.22) relates $n_R$ at two different times $t$ and $t'$. We can choose $t'$ to take any convenient value, and it is useful to choose $t' = \kappa^{-\sigma}$. The solution is then given by

$$n_R(t, n_0(t), g_R(t)) = \kappa^{-d} t^{-d/\sigma} n_R(t = \kappa^{-\sigma}, n_0(\kappa), g_R(\kappa)) \tag{4.23}$$

with $n_0(\kappa)$ and $g_R(\kappa)$ related to $n_0(t)$ and $g_R(t)$ through solutions to equations (4.20) and (4.21), which are

$$n_0(\kappa) = \kappa n_0(t) t^{d/\sigma} \tag{4.24}$$

and

$$g_R(\kappa) = g_R^* \left[1 + \frac{g_R^* - g_R(t)}{g_R(t)\kappa^d t^{\epsilon/\sigma}}\right]^{-1}. \tag{4.25}$$

Note that $n_0(t) \sim t^{-d/\sigma}$, which implies that a large $n_0$ limit can be taken to take a large $t$ limit; higher order terms in $n_0$ correspond to sub-leading terms in $t$ at large $t$. Also note that the large-$t$ limit of $g_R$ is simply $g_R^*$.

### 4.1.3 Density

We must now calculate the right-hand side of (4.23) to determine the density of particles as a function of time. This will be done as a perturbation series in the number of loops in the diagrams included at each order. In the calculation of the density we will need two "classical" quantities. These are calculated without including the effects of fluctuations and so correspond to classical quantities in a field theory. They are calculated using only tree diagrams, with no loops.

The classical density will be represented by a dashed line in diagrams and is given by the sum of all tree diagrams with one leg to the left. As can be seen from figure 4.2,

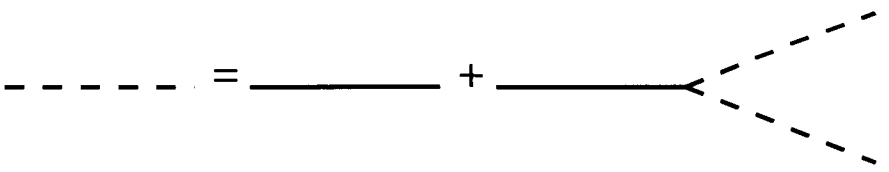

Figure 4.2: A graphical demonstration that the classical density, which is the sum of all tree diagrams and is represented by a dashed line, is given by the integral equation (4.26).

it is given by the integral equation

$$n_{\rm cl}(t) = G_0(\mathbf{k}=0,t) + \int {\rm d}t' G_0(\mathbf{k}=0,t-t') n_{\rm cl}^2(t') G_0(\mathbf{k}=0,t') \tag{4.26}$$

where $G_0$ is the bare diffusion Green function. The classical density is thus the same as the mean-field solution:

$$n_{\rm cl} = \frac{n_0}{1+2n_0\lambda t}. \tag{4.27}$$

We need the long time limit of this term, which is

$$n_{\rm cl} \approx \frac{1}{2\lambda t}. \tag{4.28}$$

This will be used below to replace density lines in diagrams and is also the first term in an expansion in the number of loops, corresponding to the set of all tree diagrams with no loops. Each diagram in this sum is renormalized by the vertex corrections calculated in section 4.1.1. To the required order, the renormalized tree level contribution can be found by replacing $\lambda$ by the bare dimensionless annihilation rate $g$, $\lambda = \kappa^\epsilon g$, and then expanding $g$ in the renormalized coupling as in equation (4.14), $g \approx g_R + \frac{g_R^2}{g_R^*}$

$$n^{(0)} \approx \frac{1}{2\kappa^\epsilon t g_R} - \frac{1}{2\kappa^\epsilon t g_R^*}. \tag{4.29}$$

This is then the tree-level contribution to the right-hand side of (4.23) and so must be evaluated at $t = \kappa^{-\sigma}$ and multiplied by $\kappa^{-d} t^{-d/\sigma}$ to give a contribution to $n_R(t)$:

$$n^{(0)}(t) = \left[\frac{1}{2g_R} - \frac{1}{2g_R^*}\right] t^{-d/\sigma}. \tag{4.30}$$

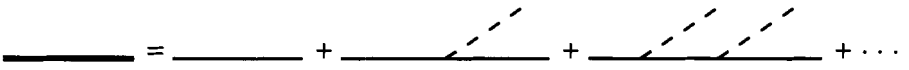

Figure 4.3: The classical response function, represented by a heavy line, is defined by a sum of diagrams with a propagator and increasing numbers of added density lines.

The classical response function will be represented by a heavy line in diagrams and is given by the sum of diagrams with a single propogator with any number of attached classical density lines, as shown in figure 4.3. In the field theoretic approach, the response function is given by

$$G(\mathbf{k}, t_2, t_1) = \langle \overline{\phi}(-\mathbf{k}, t_2)\phi(\mathbf{k}t_1)\rangle, \tag{4.31}$$

where the average is over the action 3.52. The classical version of the response function does not include the last term in the weight, which is non-linear in $\overline{\phi}$. The response function will be defined here by diagrammatic expansion and will be useful in writing the sum of all diagrams with a fixed number of loops.

The classical response function is

$$\begin{aligned} G_{\rm cl} &= e^{-k^\sigma(t_2-t_1)} + \int_{t_1}^{t_2} \mathrm{d}t' e^{-k^\sigma(t_2-t')} 2(-2\lambda) n_{\rm cl}(t') e^{-k^\sigma(t'-t_1)} + \\ &\quad \int_{t_1}^{t_2} \mathrm{d}t'' \int_{t_1}^{t''} \mathrm{d}t' e^{-k^\sigma(t'-t_1)} (2)(-2\lambda) n_{\rm cl}(t') e^{-k^\sigma(t''-t')} \times \\ &\qquad (2)(-2\lambda) n_{\rm cl}(t'') e^{-k^\sigma(t_2-t'')} \\ &\quad + \cdots \end{aligned} \tag{4.32}$$

$$\begin{aligned} &= e^{-k^\sigma(t_2-t_1)} \Big\{ 1 - 4\lambda \int_{t_1}^{t_2} \mathrm{d}t' n_{\rm cl}(t') + \\ &\quad (4\lambda)^2 \int_{t_1}^{t_2} \mathrm{d}t' n_{\rm cl}(t') \int_{t'}^{t_2} \mathrm{d}t'' n_{\rm cl}(t'') + \cdots \Big\}. \end{aligned} \tag{4.33}$$

The integrals are over the region $t_1 < t' < t'' < \cdots < t_2$, but can be extended to the full range $t_1 < t' < t_2$, $t_1 < t'' < t_2$, $\cdots$ by dividing by $l!$, where $l$ is the number of density lines inserted (the number of times integrated over). This then becomes the

expansion of an exponential,

$$G_{\rm cl}(\mathbf{k},t_2,t_1) = e^{-k^\sigma(t_2-t_1)}\exp\left\{-4\lambda\int_{t_1}^{t_2}{\rm d}t n_{\rm cl}(t)\right\} \quad (4.34)$$

$$= e^{-k^\sigma(t_2-t_1)}\left(\frac{1+2n_0\lambda t_1}{1+2n_0\lambda t_2}\right). \quad (4.35)$$

The diagram in figure 4.4 includes all diagrams with one loop. It represents the first correction to the density:

$$n^{(1)} = (-2\lambda)\int {\rm d}^d\mathbf{k}\int_0^t {\rm d}t_2\int_0^{t_2}{\rm d}t_1 G_{\rm cl}(0,t,t_2)G_{\rm cl}^2(\mathbf{k},t_2,t_1)(-2\lambda)n_{\rm cl}^2(t_1) \quad (4.36)$$

As discussed in section 4.1.2, the large $n_0$ limit gives the large $t$ behaviour,

$$n^{(1)} \approx \frac{1}{t^2}\int {\rm d}^d\mathbf{k}\int_0^t {\rm d}t_2\int_0^{t_2}{\rm d}t_1\left(\frac{t_1}{t_2}\right)^2 e^{-k^\sigma(t_2-t_1)}. \quad (4.37)$$

The integrals over $k$ may be done using dimensional regularization, and give

$$n^{(1)} \approx C\frac{1}{(1-d/\sigma)(2-d/\sigma)^2(3-d/\sigma)}t^{-d/\sigma} \quad (4.38)$$

with $C$ defined in equation (4.7). Expanding the (possibly divergent) terms in the denominator in $\epsilon$ gives

$$n^{(1)} \approx C\frac{1}{2}\left(\frac{\sigma}{\epsilon}-\frac{5}{4}\right)t^{-d/\sigma}. \quad (4.39)$$

The fixed point coupling $g_R^*$ may be introduced using an approximation to the gamma function

$$1/g_R^* = C\Gamma(\epsilon/\sigma) \approx C(\sigma/\epsilon-\gamma), \quad (4.40)$$

with $\gamma \approx 0.5772$ Euler's constant. This then implies $\sigma/\epsilon \approx 1/(Cg_R^*)+\gamma$, and so

$$n^{(1)} \approx \left[\frac{1}{2g_R^*}+C\left(\gamma-\frac{5}{4}\right)\right]t^{-\frac{d}{\sigma}}. \quad (4.41)$$

Just as for $n^{(0)}$, this is a contribution to the right-hand side of (4.23), and must be evaluated at $t=\kappa^{-\sigma}$ and multiplied by $\kappa^{-d}t^{-d/\sigma}$ to give a contribution to $n_R(t)$. However, this procedure does not change the form of this term. The term proportional to $1/g_R^*$ is divergent as $\epsilon\to 0$, and is cancelled by a term coming from the tree level

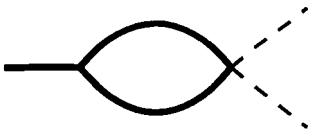

Figure 4.4: This diagram includes all diagrams with one loop. The heavy lines represent the classical response function, and the dashed lines represent the classical density.

contribution $n^{(0)}$ expanded to second order in $g_R$, as given by equation (4.30). Adding these terms gives the density

$$n(t) = At^{-\frac{d}{\sigma}} \tag{4.42}$$

with

$$A \approx \frac{1}{2g_R(\kappa)} + C\left(\gamma - \frac{5}{4}\right). \tag{4.43}$$

Since we want the long-time behaviour of the density, $g_R(\kappa)$ may be replaced by its large-$t$ value, from (4.25), of $g_R^* = (C\Gamma(\sigma/\epsilon))^{-1}$. Using the expansion for the gamma function in (4.40) and the value of $C$ from (4.7), we see

$$A \approx \frac{2^{1-d/\sigma}}{(4\pi)^{d/2}\sigma} \frac{\Gamma\left(\frac{d}{\sigma}\right)}{\Gamma\left(\frac{d}{2}\right)} \left[\frac{\sigma}{\epsilon} - \frac{5}{2}\right]. \tag{4.44}$$

This is the renormalization group prediction for the amplitude of the density decay in time. The next correction to this term is proportional to $\epsilon$. This prediction for the amplitude will be compared to simulation results in chapter 5. The exponent $d/\sigma$ in equation (4.42) is also a prediction of the renormalization group calculation.

## 4.2 Branching and Annihilation Reactions

In this section, we will use the renormalization group methods of the previous section to analyse a system in which particles are allowed to branch, creating two new "offspring" particles. The action we will study is derived in chapter 3 and is given by

$$S = \int \mathrm{d}^d x \Big[ \int_0^T \mathrm{d}t [\hat{\phi}(\mathbf{x},t)[\partial_t - D_A\nabla^\sigma]\phi(\mathbf{x},t) - \lambda[1 - \hat{\phi}(\mathbf{x},t)^2]\phi(\mathbf{x},t)^2$$

$$+ \mu[1 - \hat{\phi}(\mathbf{x},t)^2]\hat{\phi}(\mathbf{x},t)\phi(\mathbf{x},t)] - \phi(\mathbf{x},\tau) - n_0\hat{\phi}(\mathbf{x},0)\Big]. \quad (4.45)$$

The results of this calculation will be compared to simulations in chapter 5. The simulations are of a model in one dimension, so we will summarize the results of the calculation in one dimension here. In one dimension, we will find that for $\sigma < \sigma_c' = 3/2$, the branching reaction is relevant at the annihilation fixed point. This means that in this regime the critical point is at zero branching rate $\mu = 0$, and the dynamics at criticality are described by the model with annihilation alone. For $\sigma > \sigma_c$, the branching reaction is irrelevant at the annihilation fixed point, and the associated rate $\mu$ flows to zero under the renormalization transformation. This means that there may be range of values of $\mu$ over which the model is described by the pure annihilation model; this range is given by the range over which the branching rate flows to zero. The critical point is governed by a different fixed point, and so may be described by different exponents. This fixed point is not accessible using the methods described in this thesis.

The approach used to calculate the critical behaviour of a system with both branching and annihilating reactions will be slightly different from that used in the previous section. The shift from $\hat{\phi}$ to $\bar{\phi}$ done in section 3.1.3 should not be done here, as it obscures a symmetry of the field theory related to parity conservation: except for terms which depend explicitly on the initial or final state, the action (4.45) is invariant under the simultaneous change of the sign of both $\hat{\phi}$ and $\phi$. After this shift is done, it is usual to drop the higher order terms which appear, which causes the symmetry to be lost. Since this shift should not be done, it is difficult to derive the Langevin equation which would be used to generate a perturbative expansion, in an analysis similar to that done in the pure annihilation case. Here, we will study the field theory directly. Fortunately, the shift is useful only in the calculation of what are called "inclusive" quantities, whose operator representations include operators at all lattice sites, such as the total density of particles. "Exclusive" quantities, such as the probability that a particular lattice site is occupied exclusive of the state of the rest of the system, can be calculated in the unshifted theory. In fact, in the calculation below the correlation function being calculated will not be explicitly specified. All

results will be derived from an examination of the scaling of couplings appearing in the theory. The renormalization group equations derived below do not depend on which correlation functions are calculated.

For the more general problem with branching to $m$ offspring, the only term in the action which changes is the one related to the branching rate, proportional to $\mu$. The new term is

$$S_{B_m} = \int \mathrm{d}x \int_0^\tau \mathrm{d}t \mu_m [1 - \hat{\phi}^m(\mathbf{x}, t)] \hat{\phi}(\mathbf{x}, t) \phi(\mathbf{x}, t). \tag{4.46}$$

Notice that for odd $m$ this term is not invariant under the change of sign of $\hat{\phi}$ and $\phi$. This means that the shift $\hat{\phi} \to \bar{\phi} + 1$ may be done. The resulting field theory describes the directed percolation universality class and is discussed in [41]. For $m$ even but larger than two, the reaction with $m = 2$ is generated under renormalization, and so the theory with $m = 2$ describes the behaviour of all models with $m$ even.

Using the field theory directly changes the derivation of the perturbation series in some ways. Rather than using the perturbative expansion of the solution to a Langevin equation, the diagrammatic expansion is derived by expanding the action about the action with no interaction terms, containing only terms linear in $\hat{\phi}$ and $\phi$. All quantities can be easily calculated in the non-interacting theory, by Gaussian integration. Higher order terms are written as expectation values of the nonlinear terms, evaluated with respect to the linear action. The propagators and vertices appearing in a diagrammatic expansion are then derived to represent the terms in this expansion. The results of this derivation can be seen by inspection of the action: there are two vertices corresponding to the annihilation rate, from the terms $\lambda\phi^2$ and $-\lambda\bar{\phi}^2\phi^2$, and one vertex corresponding to the annihilation rate, from the term $\mu\bar{\phi}\phi^3$. The fact that the shift is not made changes the diagrammatic expansion slightly, as can be seen by examining the action (4.45). The first vertex corresponding to the annihilation rate differs from that used in the pure annihilation problem: it no longer has a leg to the right, as it corresponds to the term $\lambda\phi^2$ in the action. The diagrammatic representations of the annihilation reactions are shown in figure 4.5.

The engineering dimensions of most quantities appearing in this field theory have already been given in section 4.1. Only the branching rate $\mu$ is new, and is of dimension

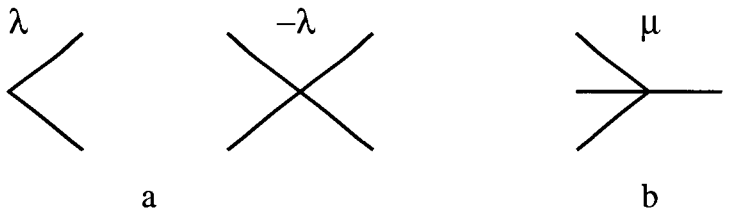


Figure 4.5: The vertices associated with annihilation (a) and with branching (b) in a diagrammatic expansion.

$[\mu] = [\kappa^\sigma]$, in terms of the same arbitrary momentum scale $\kappa$. Power counting thus predicts that the upper critical dimension is again $d_c = \sigma$, the dimension at which the annihilation rate becomes dimensionless.

In keeping with the direct use of the field theory, we will use a more field-theoretic notation in this section. This will also make a comparison with the calculation of the normal diffusion case, done in [11], more straightforward. A field-theoretic approach to the renormalization group can be found in several books on critical phenomena, such as [42]. The renormalization of coupling constants, as done in section 4.1 for the annihilation rate, can be handled by defining renormalization constants $Z$ relating renormalized and un-renormalized couplings. The calculation of renormalization group flow functions is similar to the calculation in section 4.1 and will not be given here. Only the results will be presented.

The dimensionless renormalized annihilation coupling is defined by

$$\ell = Z_\lambda \lambda C_d \kappa^{-\epsilon} / D_A, \tag{4.47}$$

with $\epsilon = d_c - d = \sigma - d$ and

$$C_d = \frac{\Gamma(d/\sigma)}{\Gamma(d/2)} \frac{\Gamma(2 - d/\sigma)}{2^{d-1}\pi^{d/2}}. \tag{4.48}$$

The one loop renormalization factor $Z_\lambda$ is then

$$Z_\lambda = 1 - \frac{\lambda}{D_A} \frac{C_d \kappa^{-\epsilon}}{\epsilon}. \tag{4.49}$$

This factor is calculated by performing the integrals which are represented by the diagrams in figure 4.6. This result for $Z_\lambda$ is simply the result (4.10) for the annihilation

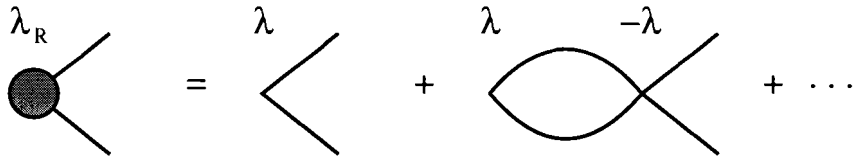


Figure 4.6: The diagrams which contribute to the renormalized annihilation rate $\lambda_R$ in the field theoretic calculation. Note that time flows from right to left, as in the previous chapter.

rate in the pure annihilation model, with only the first two terms in the sum retained, and re-interpreted with the new definition, (4.47), of the dimensionless renormalized annihilation rate. The $\beta$ function is now given by

$$\beta_\ell(\ell) \equiv \kappa \frac{\partial \ell}{\partial \kappa} = \ell(d - \sigma + \ell), \tag{4.50}$$

with fixed points at $\ell = 0$ and $\ell = \ell^* = \epsilon = \sigma - d$. In section 4.1, the same result was derived for the $\beta$ function to all orders in the annihilation rate, by summing all contributions to the renormalized annihilation rate. The $\beta$ functions in this section and in section 4.1 differ only due to the differing definitions of the renormalized annihilation rate; if the same definition were used here as in section 4.1, they would have the same form. The result (4.50) is thus exact at the annihilation fixed point, as the result in section 4.1 is the exact $\beta$ function at the annihilation fixed point. Just as in the pure annihilation problem, the Gaussian fixed point at $\ell = 0$ is stable for $d > \sigma$, while for $d < \sigma$ the non-trivial $O(\epsilon)$ fixed point at $\ell = \ell^*$ is stable.

The one loop renormalization group eigenvalue for the branching process at the annihilation fixed point determines whether the branching process is relevant at this fixed point. Defining the dimensionless renormalized branching rate as

$$s = Z_\mu \mu \kappa^{-\sigma} / D_A, \tag{4.51}$$

the one loop renormalization factor,

$$Z_\mu = 1 - 3 \frac{\lambda}{D_A} \frac{C_d \kappa^{-\epsilon}}{\epsilon}, \tag{4.52}$$

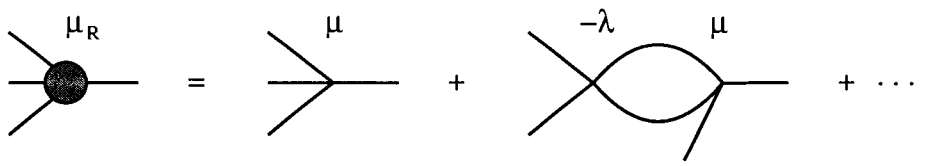


Figure 4.7: The diagrams which contribute to the renormalized branching rate $\mu_R$.

is computed from the diagrams in figure 4.7. The $\zeta$ function, describing the flow of the branching rate under renormalization, is therefore

$$\zeta_\mu \equiv \kappa \frac{\partial}{\partial \kappa} \ln \frac{s}{\mu} = -\sigma + 3\ell + \mathcal{O}(\ell^2). \tag{4.53}$$

Thus, the renormalization group eigenvalue for the branching process at the annihilation fixed point is, at one loop,

$$y_\mu = -\zeta_\mu(\ell^*) = \sigma - 3\epsilon = 3d - 2\sigma. \tag{4.54}$$

Cardy and Täuber [11] performed this calculation for the normal diffusion model, where $\sigma = 2$. In their case, the result (4.54) indicates that for dimensions larger than $d_c' = 4/3$, the branching rate is relevant at the annihilation fixed point. The branching rate flows away from zero, and so the system will be in its active phase, with a steady-state density of particles in the long time limit, for almost all values of the couplings. Only where the branching rate is exactly zero is the model described by the pure annihilation fixed point. In this regime, any non-zero branching rate will grow under renormalization, resulting in a steady state density of particles. In dimensions less than 4/3, the branching rate becomes irrelevant at the annihilation fixed point. In this régime, for some range of branching rates, the branching rate flows to zero and the behaviour is given by the behaviour at the pure annihilation fixed point. A new inactive phase, with a power law decay to zero particles, becomes possible. Using a different expansion, a truncated loop expansion in fixed dimension, Cardy and Täuber predicted that the critical annihilation rate should be discontinuous at $d_c'$, jumping from zero to some finite value.

With anomalous diffusion, the branching process is relevant at the annihilation fixed point for

$$\sigma < \sigma_c'(d) = 3d/2, \tag{4.55}$$

to one loop. In $d = 1$, this is true for $\sigma < \sigma_c'(d = 1) = 3/2$. As in the mean field case, there should be an active phase for all nonzero values of the branching rate $\mu$, for sufficiently small $\sigma$. The field theory studied in section 4.1 describes the dynamics at this critical point, as it occurs for zero branching rate. As $\mu$ increases away from zero, there will be new behaviour related to the branching reaction, as this is a relevant perturbation in this regime. The density decay at the pure annihilation fixed point, calculated in the previous section, is given by $n(t) \sim t^{-d/\sigma}$ (for $d < \sigma \leq 2$). In [43] it is shown that at criticality the density should decay as $t^{-\beta_{\text{dens}}/\nu_\parallel}$. Here $\beta_{\text{dens}}$ and $\nu_\parallel$ are critical exponents which describe the behaviour close to but not exactly at the critical point, as defined in section 1.1.1. $\beta_{\text{dens}}$ controls the dependence of the steady state density on the distance to the critical point, and $\nu_\parallel$ controls the correlation length in the temporal direction. Matching this result to the Lévy annihilation case we have $\beta_{\text{dens}} = d\nu_\parallel/\sigma$.

The exponent $\beta_{\text{dens}}$ may be calculated from the renormalization group eigenvalue $y_\mu$. Cardy and Täuber show that in this régime $\beta_{\text{dens}}$ is given by $\beta_{\text{dens}} = d/y_\mu$. This is shown by solving the renormalization group equation to show that the density has a scaling form and then demanding that at large times the time-dependence cancels. This then fixes the dependence of the asymptotic density on the branching rate. The eigenvalue $y_\mu$ is given in equation (4.54) so that $\beta_{\text{dens}} = d/(3d - 2\sigma)$.

When $\sigma > \sigma_c'(d)$, the branching reaction becomes irrelevant at the Lévy annihilation fixed point. For any value of $\sigma$, this regime may be present only for $d$ lower than a critical dimension. The highest possible value of this new critical dimension occurs for normal diffusion. From equation (4.55), it is given by $d < d_c'(\sigma = 2) = 4/3$, to one loop order. For any dimension lower than $d_c'(\sigma)$, the critical branching rate $\mu_c(\sigma, d)$ should become nonzero. For $0 < \mu < \mu_c(\sigma, d)$, the branching will be asymptotically irrelevant, and this phase will again be governed by the exponents of the pure Lévy annihilation universality class described in section 4.1. The different possibile regions

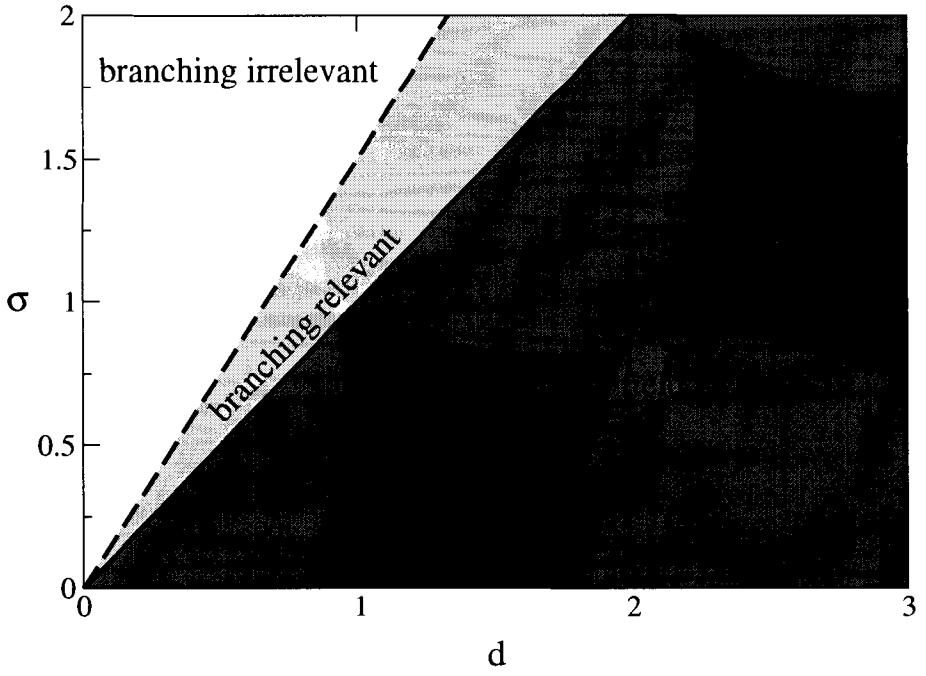


Figure 4.8: Regions of different behaviours in the $\sigma, d$ plane. Mean field exponents are observed below the solid line (dark grey region). Below the dashed line the branching rate is relevant at the annihilation fixed point, and so the critical point is at zero branching rate. Above the dashed line the branching reaction is relevant at the annihilation fixed point, and so there may be an active phase for some finite values of $\mu$.

are summarized in figure 4.8. At $\mu = \mu_c(\sigma, d)$ there should then be a non-trivial transition to an active phase. As was the case for the short-ranged model, this transition is inaccessible to controlled perturbative expansions and is governed by exponents different from either the pure annihilation model or the model with branching to an odd number of offspring. The expansion in $\epsilon$ only applies to the critical point of the model which includes branching from the upper critical dimension down to $d_c'(\sigma) = 2\sigma/3$, to one loop order. This is due to the fact that the expansion is around the pure annihilation fixed point $\mu = 0$. Once the critical point moves to a fixed value of $\mu$, the expansion must be done about this new fixed point. This cannot be done in the $\epsilon$-expansion in the number of dimensions, as this must be done about the fixed point at the upper critical dimension. For $d < d_c'(\sigma)$, the $\epsilon$ expansion describes only the

behaviour at zero branching rate. The new transition at a non-zero branching rate is not governed by exponents calculated from this expansion.

Note that a "precursor" of the critical inactive phase present for $\sigma > \sigma_c'(d)$ is already evident in the $\sigma < \sigma_c'(d)$ regime. Using the above analysis, we see that $\beta_{\text{dens}} = d/y_\mu = d/(3d - 2\sigma)$ for $\sigma < \sigma_c'(d)$ (to one loop). Hence, to this order, as $\sigma \to \sigma_c'(d) = 3d/2$ from below, $\beta_{\text{dens}}$ diverges. This implies that for a fixed small value of the branching, the active phase has a decreasing density as a function of $\sigma$, as $\sigma$ is increased toward $\sigma_c'(d)$. Finally at $\sigma = 3d/2$ (to one loop order) an entire critical inactive phase opens up.

All of this analysis has implications for the model with normal diffusion. The behaviour of the model with normal diffusion as the dimension is lowered from $d = 2$ to $d = 1$ is analogous to the behaviour of the model with Lévy flights in fixed $d = 1$, as the Lévy index $\sigma$ is raised from $\sigma = 1$ to $\sigma = 2$. In particular, to one loop order, the region $1 < \sigma < \sigma_c'(d = 1) = 3/2$ for the $d = 1$ model with anomalous diffusion contains the direct analogue of the inaccessible universality class present in model with normal diffusion for $d_c' \approx 4/3 < d < 2$. The analogue of the transition predicted in the model with normal diffusion at $d = 4/3$ may be directly studied in a simulation of the model with Lévy flights. The results of simulations of this model are presented in the next chapter.

# Chapter 5

# Simulations

Several simulations were done and compared with the renormalization group results discussed in previous chapters. The model simulated is very similar to that described by the M-equation (3.1). A set of particles are allowed to move on a one-dimensional lattice, with appropriate reactions at each time step. We will present the results of simulations of both systems discussed in the previous chapter and show that the predictions of the renormalization group are seen in these simulations.

In the model with pair annihilation alone the decay of the density of particles in this model should be given by the power law decay calculated in using the renormalization group in section 4.1.3. We will see that the renormalization group calculation does very well at predicting the exponent and that the $\epsilon$-expansion for the amplitude $A$ is good for small $\epsilon$. The small-$\epsilon$ region is explored by taking $\sigma$ slightly larger than 1.

When a branching reaction is added a phase transition appears as the branching probability is varied. The renormalization group calculation in section 4.2 predicts, for this one-dimensional simulation, that for $\sigma < 3/2$ there will be an active phase for any non-zero branching rate. For $\sigma > 3/2$, an inactive phase becomes possible at finite branching rate. This will be seen in the simulations. For $\sigma < 3/2$ the renormalization group calculations give a numerical estimate of the exponent $\beta_{\text{dens}}$, governing the dependence of the steady-state density on the distance to the critical point. This exponent has been calculated in simulations in this region, and will be compared to the renormalization group calculation. The renormalization group techniques used in

the previous chapter make no predictions about the exponents near the new critical point that emerges for $\sigma > 3/2$. Simulations may be done in this region, and the results of these simulations are given below.

The system simulated differs from that studied analytically in that only one particle is allowed to occupy a lattice site. If a particle moves to an occupied site, both particles are annihilated. There has been some discussion of whether this single-occupation condition is an important difference from the model studied using field theoretic techniques. In the systems studied here, the difference seems likely not to be important for several reasons. First, since the annihilation rate is renormalized and flows to a fixed point, the bare annihilation rate does not appear in the final result, and so the fact that particles annihilate with probability one should not change the results. Second, at and near the critical point, the density is small, so the probability that two particles are at the same site is very small in either case. Third, one of the important differences in one dimension is that, in models where diffusion proceeds by hops only to nearest neighbour sites, particles cannot pass each other, which is not the case in the simulations done here. This feature is one reason for the fact that some models can be solved exactly in one dimension. It can also create significant differences in long-time behaviour. For example, the two-species annihilation reaction $A+B \rightarrow \emptyset$ has, in general, asymptotic behaviour different from the single-species reaction. However, if the initial condition is alternating $A$ and $B$ particles, then if particles cannot pass each other, the two-species reaction behaves in the same way as does the single-species reaction. In the simulations done here, particles may move more than one lattice site in a single hop, and so different particles may pass each other. In any case, the agreement between the simulation results and the field-theoretic calculation indicates that the universal properties of both kinds of models are the same.

## 5.1 Anomalous Diffusion With Pair Annihilation

For the pair annihilation problem, all simulations were done on a one-dimensional lattice, which, at the beginning of the simulation, contained $10^7$ sites, each occupied by a single particle. Each time that the number of particles fell below 1000, the system

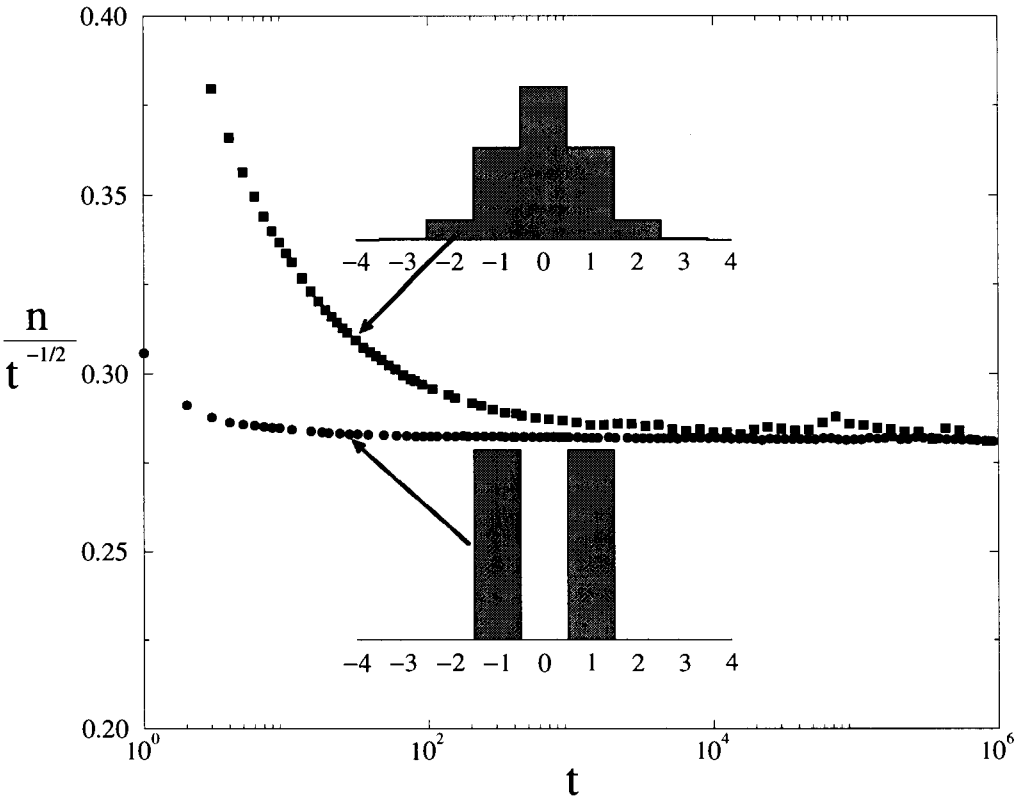


Figure 5.1: The density of particles for the pair annihilation process with normal diffusion. The two curves differ in the distribution of hop lengths taken at each step; these distributions are shown. Particles may hop only a single site in the lower distribution, while they may hop several sites, with the length of the hop chosen from a discrete version of a Gaussian, in the upper distribution.

was doubled by appending an exact copy of the current configuration of particles. While this does make the system momentarily periodic, the two halves subsequently evolve in different ways. This allowed the simulation to continue to large times without large statistical fluctuations in the density. The number of times that it was necessary to double the system size varied, depending on $\sigma$. For $\sigma = 1.05$, the final system size was $L = 2^9 \times 10^7$.

The locations of the particles were stored in two different ways. Early in each simulation run, when there were many particles, the occupation numbers of the entire

lattice were stored, with a single bit indicating whether or not each site was occupied. In each time step, a random lattice site was chosen and, if the site was occupied, the particle there was moved. Late in the simulation, this became inefficient, and so only the indices of occupied sites were stored. An occupied site was chosen from this list to undergo diffusion. In each time step, each particle would, on average, move once; in the later stage of the simulation, when only the indices of occupied sites were stored, the time was incremented by one over the number of particles after each move.

All simulations for the pair annihilation problem were done with the full Lévy distribution, with hop distances generated by equation (2.24). This is unlike the method used to generate the long-range hops in the simulations of the branching process described below, where a simple power law distribution was used. The full Lévy distribution was used here so that it would be simpler to identify the anomalous diffusion constant, and so that the asymptotic form of the distribution of hops was reached more quickly. However, due to the fact that the simulations were performed on a lattice, it was necessary to rescale slightly the distances generated to produce the correct limit of the probability distribution for small $k$. Since one of the quantities calculated analytically is the amplitude of the power law of the decay in time, which depends on the anomalous diffusion constant, it was important that this quantity was correct.

The time taken to reach the asymptotic power law depends on the irrelevant scaling variables. Figure 5.1 shows the particle density divided by its long-time power-law form, for normal diffusion implemented in two different ways. For the lower curve, each hop is taken a single lattice spacing either to the left or to the right with probability $\frac{1}{2}$, while for the upper curve, the distribution of hops more closely resembles a Gaussian. Both distributions have the same second moment, and so the coefficient of the $k^2$ term in the field theory or the Langevin equation is the same in both cases. If particles diffused according to these two distributions, with no reactions, the long time distributions of the particle positions would be identical. However, the coefficients of terms higher order in $k$, which are irrelevant in the renormalization group sense, are different. This leads to quite different crossover behaviours.

In the case of anomalous diffusion, long crossovers made it quite difficult to observe

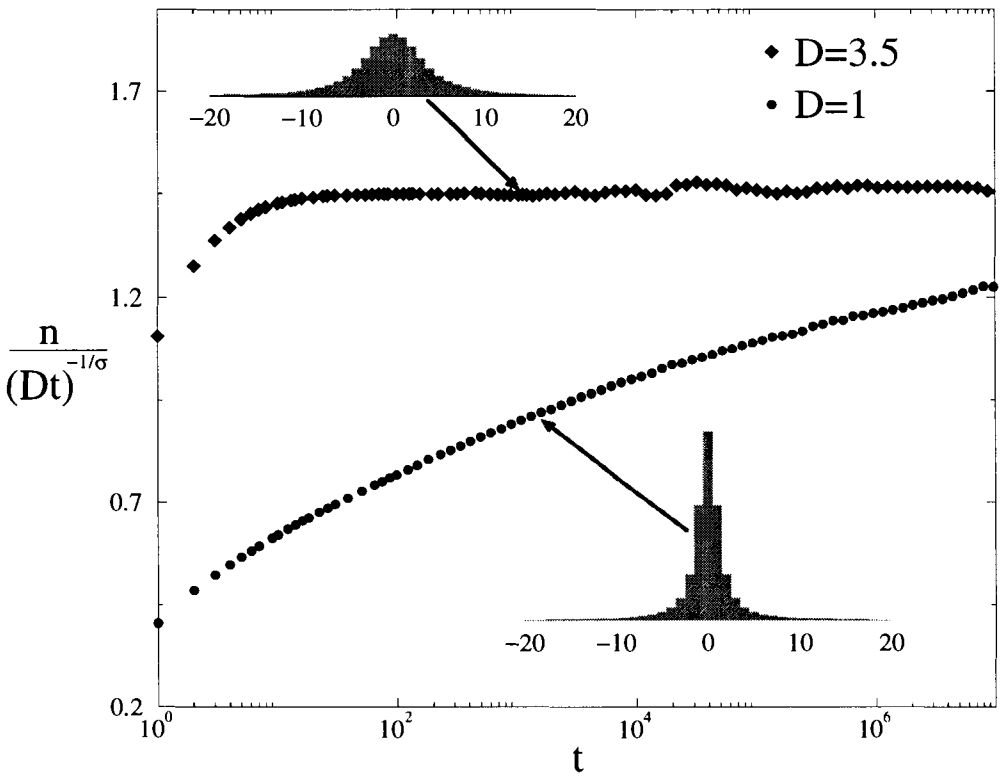


Figure 5.2: The density of particles for the pair annihilation process with anomalous diffusion, with $\sigma = 1.1$.

the long-time behaviour for some values of $\sigma$ and $D_A$. In this case, since it was simplest to perform all simulations for a given $\sigma$ with the same distribution, the crossover was reduced by changing the anomalous diffusion constant $D_A$. This will change the coefficient of the $k^\sigma$ term appearing in the action as well as the coefficients of all higher order terms. The density decays for two different anomalous diffusion constants are shown in figure 5.2.

The fact that the value shown for $\frac{n}{(D_A t)^{-1/\sigma}}$ is constant over seven decades for $D_A = 3.5$ shows that the exponent is essentially exact. The amplitude $A$ of the power law is easy to extract from this data. $A$ can also be extracted from the data for

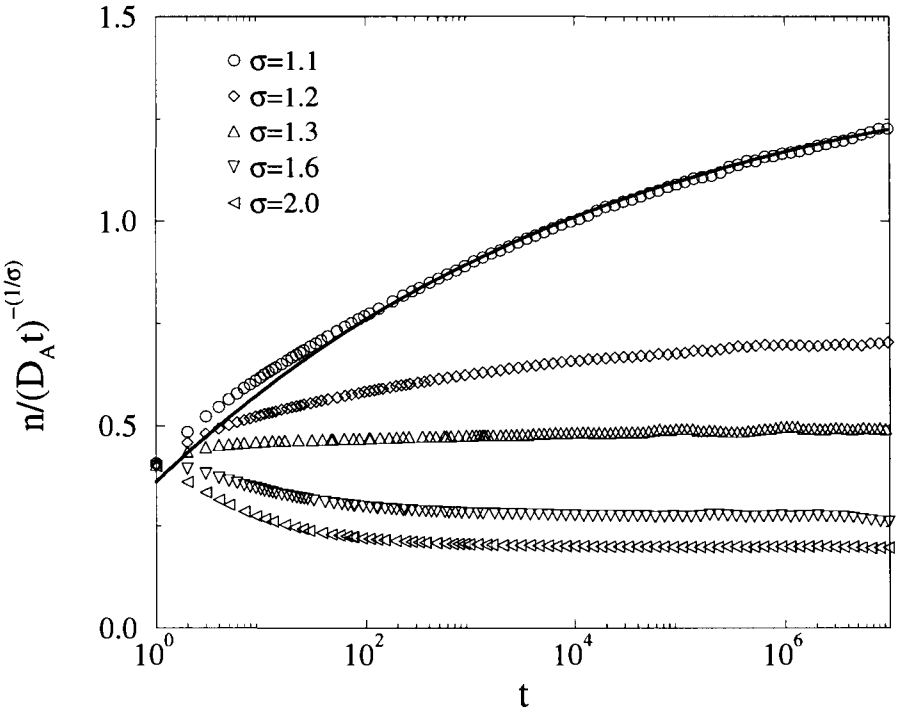


Figure 5.3: The density of particles for the pair annihilation process with anomalous diffusion, for several values of $\sigma$, and $D_A = 1$. The time taken to cross over to the long-time behaviour varies significantly as $\sigma$ is varied. The solid line is a fit to the form of equation (5.1), with the parameters extrapolated to $t \to \infty$.

$D_A = 1.0$, by fitting to an assumed crossover scaling form

$$\frac{n(t)}{(D_A t)^{-1/\sigma}} = A(1 - Bt^{-\phi}). \tag{5.1}$$

To obtain the long-time value of the amplitude, the fit was done over many ranges with differing starting times and extrapolated to $t \to \infty$.

Figure 5.3 shows the density decay for several values of $\sigma$. The crossover to the asymptotic behaviour is clearly strongly dependent on the anomalous diffusion constant. It is possible to extract a value for the amplitude $A$ from this data by using the crossover form of equation 5.1, and these values are similar to the values extracted

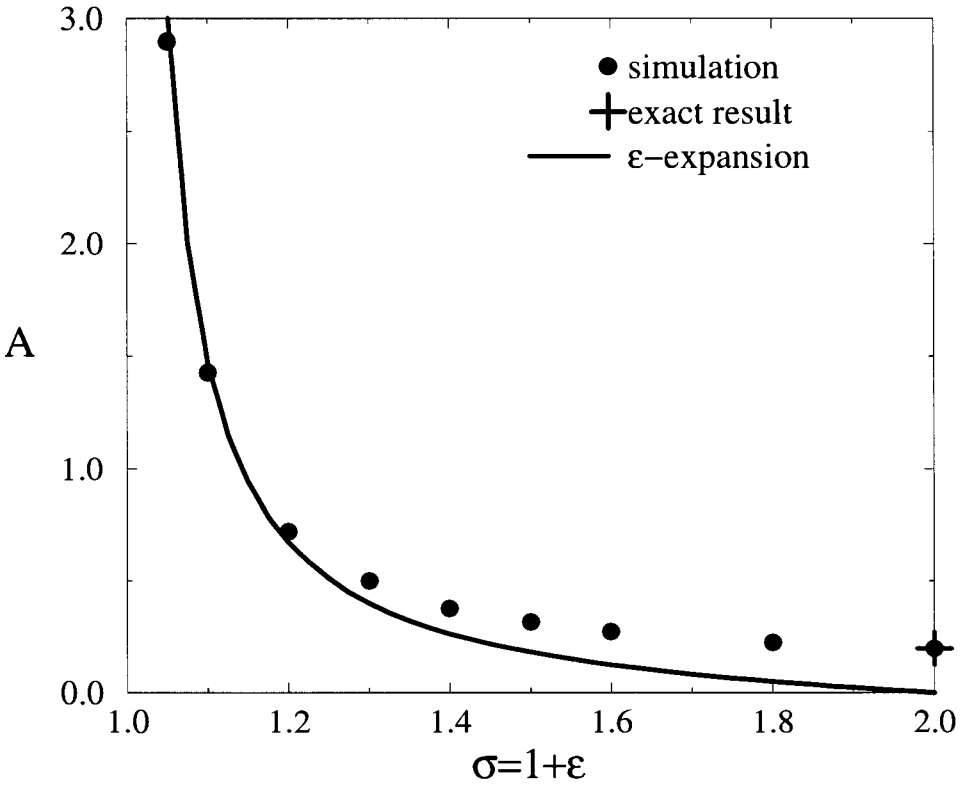


Figure 5.4: The amplitude of the power law decay of the density of particles determined in simulation (circles), compared with the renormalization group prediction of equation (4.44). Also shown is the exact result [44] for the normal diffusion case (cross).

from simulations with different values of $D_A$, chosen to produce much shorter crossover regions.

As can be seen in figure 5.3, the time taken to cross over to the asymptotic density decay varies significantly for fixed diffusion constant. This is why the simulations at different values of $D_A$ shown in figure 5.2 were originally performed; it is difficult to see that the density decay at $D_A = 1$ is converging to a power law for values of $\sigma$ close to 1.

The prediction for the amplitude is compared to simulation results in figure 5.4. The agreement between the $\epsilon$-expansion for the amplitude and the simulation result becomes quite good for small $\epsilon$, as expected for this asymptotic power series expansion.

An exact result for $A$ is available for the case of nearest-neighbour hops [44], and is also shown in the figure. This result is the same as the simulation result for $\sigma = 2$, as it should be. The hop length distribution for $\sigma = 2$ is a Gaussian, with width $\sqrt{2D}$. The field theory describing motion according to this distribution differs from that describing motion by single hops in the coefficients of powers of $k$ beyond $k^2$, but the renormalization-group calculation indicates that $A$ is a universal quantity, independent of the coefficients of higher powers of $k$. The fact that these amplitudes are equal in the long time limit can also be seen in figure 5.1, where the results of simulations in which particles hop a single site and in which particles may take longer hops chosen from a broader distribution are compared.

| $\sigma$ | $D_A$ | $A$ |
|---|---|---|
| 1.05 | 6.5 | 2.9 |
| 1.05 | 1.0 | 2.9 |
| 1.1 | 3.5 | 1.45 |
| 1.1 | 1.0 | 1.43 |
| 1.2 | 1.0 | 0.72 |
| 1.3 | 1.0 | 0.51 |
| 1.4 | 1.0 | 0.38 |
| 1.5 | 1.0 | 0.32 |
| 1.6 | 1.0 | 0.275 |
| 1.8 | 1.0 | 0.227 |
| 2.0 | 1.0 | 0.199 |

Table 5.1: The amplitude $A$ of the power law decay of the density of particles for the pure annihilation reaction. The values for $A$ for $D_A = 1$ and $\sigma < 1.2$ were determined from a fit to a crossover function (5.1), while the other values could simply be read off from the simulation data (see figures 5.2 and 5.3.)

## 5.2 Annihilation and Branching Reactions

Simulations of the process with anomalous diffusion, annihilation, and branching were also performed. Here, two different types of simulation were performed, with different

initial conditions. In the first set of simulations, the initial state was an almost empty lattice, with two particles placed at the lattice sites at $\pm 1$. In this case, since the number of particles is always small, only the position of each particle needs to be stored. These positions were stored as integers, so the effective lattice size was limited only by the number of integers, $2^{64} \approx 1.8 \times 10^{19}$ on the 64-bit computer used. This kind of simulation is often referred to as a "dynamical" or "time-dependent" simulation. The second set of simulations, like the simulations of the process with annihilation alone, were done on a lattice of size $10^7$, with an initial condition of full occupation; every site contained a single particle. These simulations were done for $\sigma < 1.5$ to determine the steady-state density as a function of the distance from the critical point, and thus the exponent $\beta_{\text{dens}}$. Periodic boundary conditions were used for both kinds of simulation.

At each time step, a randomly chosen particle was allowed either to branch, with probability $1 - p$, or to move, via a long-range jump, with probability $p$; $p$ was the only parameter in the simulations. The number of particles at each lattice site was restricted to zero or one: thus, when a particle moved to an occupied site, both particles were annihilated. At each branching step, a particle produced two offspring, which occupied the two sites to the immediate left or right of the original particle, with the side chosen randomly. As pointed out in reference [45], this method of choosing occupied sites is necessary since if the newly occupied sites are chosen symmetrically about the original site, then the short-ranged branching and annihilating random walk model is in its inactive state for all $p < 1$. This is also true of the anomalous diffusion problem, with long-ranged transport of particles, as the transition to an active state occurs at a higher $p$ than in the normal diffusion case.

Each time a particle moved, the distance was chosen from a pure power law distribution, as described in chapter 2. As mentioned there, this distribution is not a Lévy stable distribution, but the power law tails do cause its limiting distribution, at late times, to become one.

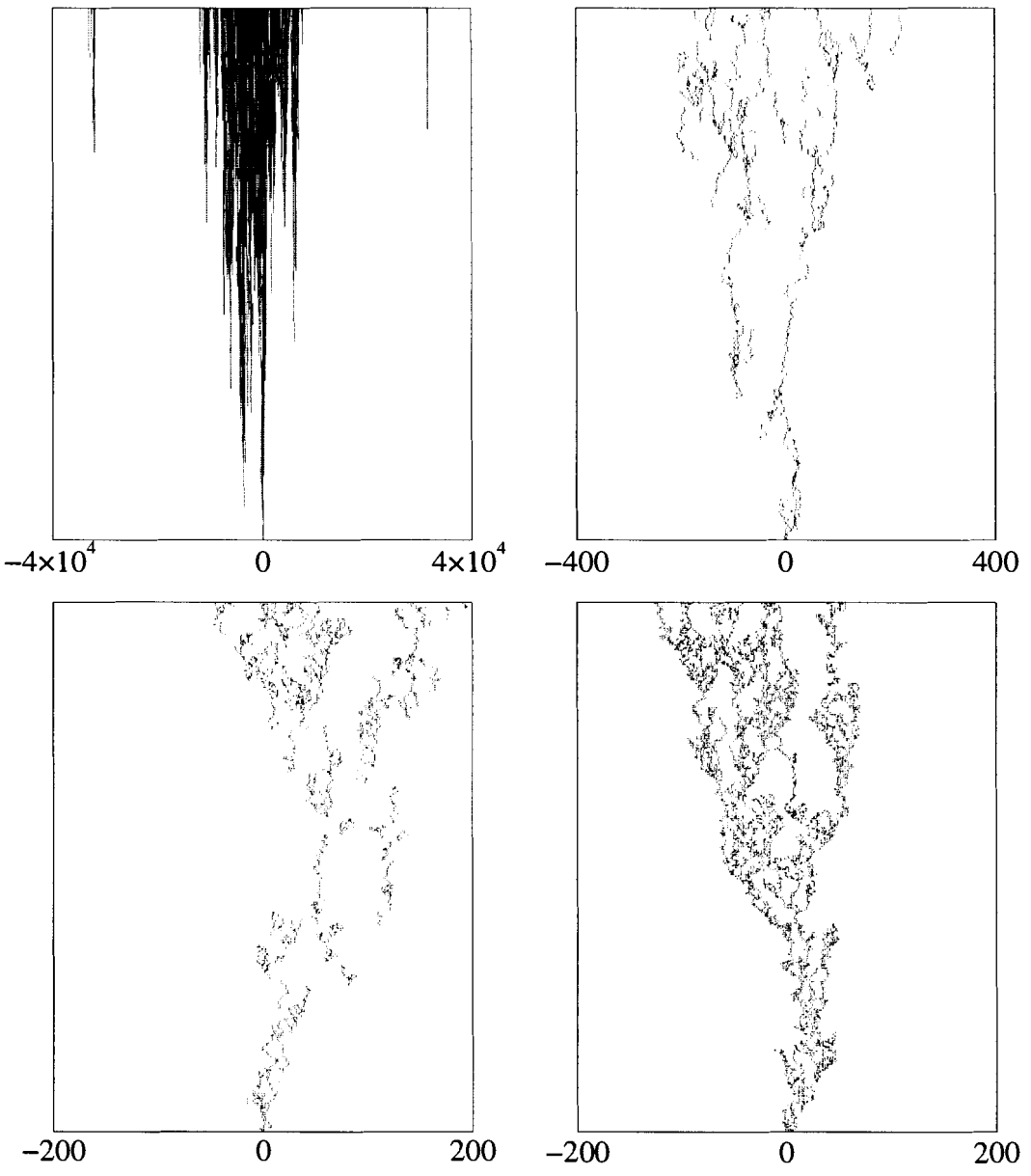


Figure 5.5: Sample runs at various values of $\sigma$, with time evolution running up the page. All runs are for 500 time steps. The top two frames show $p = 0.9$, at $\sigma = 1.0$ and $\sigma = 1.5$, from left to right. The lower left frame shows $\sigma = 1.9$, $p = 0.77$, and the lower right frame shows the model with normal diffusion (nearest-neighbour hops) at $p = 0.46$. Notice the large change in scale between the first and last frame.

### 5.2.1 Dynamical Simulations

The simulations performed beginning from a small "seed" of two particles were done to examine the critical point, in the region where it is not accessible to the renormalization group calculation of chapter 4. Examples of single runs at different values of $\sigma$ and with $p$ about 10% away from the critical point, in the active phase, are shown in figure 5.5.

The simulations were averaged over at least $2 \times 10^6$ runs with the same initial condition, but with different sequences of random numbers determining the dynamics, and were run for times between $2 \times 10^4$ and $2 \times 10^5$ timesteps. A number of different quantities were measured as functions of time in these simulations: the fraction $P(t)$ of runs surviving to time $t$, the number $N(t)$ of particles in the system, averaged over all runs, and a mean squared spreading distance $R^2(t)$. Since the usual arithmetic mean of the positions squared diverges for simulations done with Lévy flights, the geometric mean was measured instead. These quantities should all follow power law behaviour

$$P(t) \sim t^{-\delta}, \tag{5.2}$$

$$N(t) \sim t^{\theta}, \tag{5.3}$$

$$R^2(t) \sim t^{2/z}, \tag{5.4}$$

at the critical point, where the transition from an active to an absorbing state occurs. Away from the critical point, there will be deviations from power law behaviour. We will be interested in these exponents for $\sigma > \sigma_c'$, and so the renormalization group method discussed in the previous chapter makes no predictions about their values.

Simulations were performed at several values of $p$ for each value of the Lévy parameter $\sigma$. For each of the measured quantities, a "local exponent" was defined; for example, for the survival probability,

$$-\delta(t) = \frac{\ln \frac{P(t)}{P(\frac{t}{b})}}{\ln b}. \tag{5.5}$$

Here $b$ is an arbitrary parameter. The value of $b$ should not affect the results. Once the asymptotic power law behaviour is reached, $\delta(t)$ is independent of $b$. In the analysis

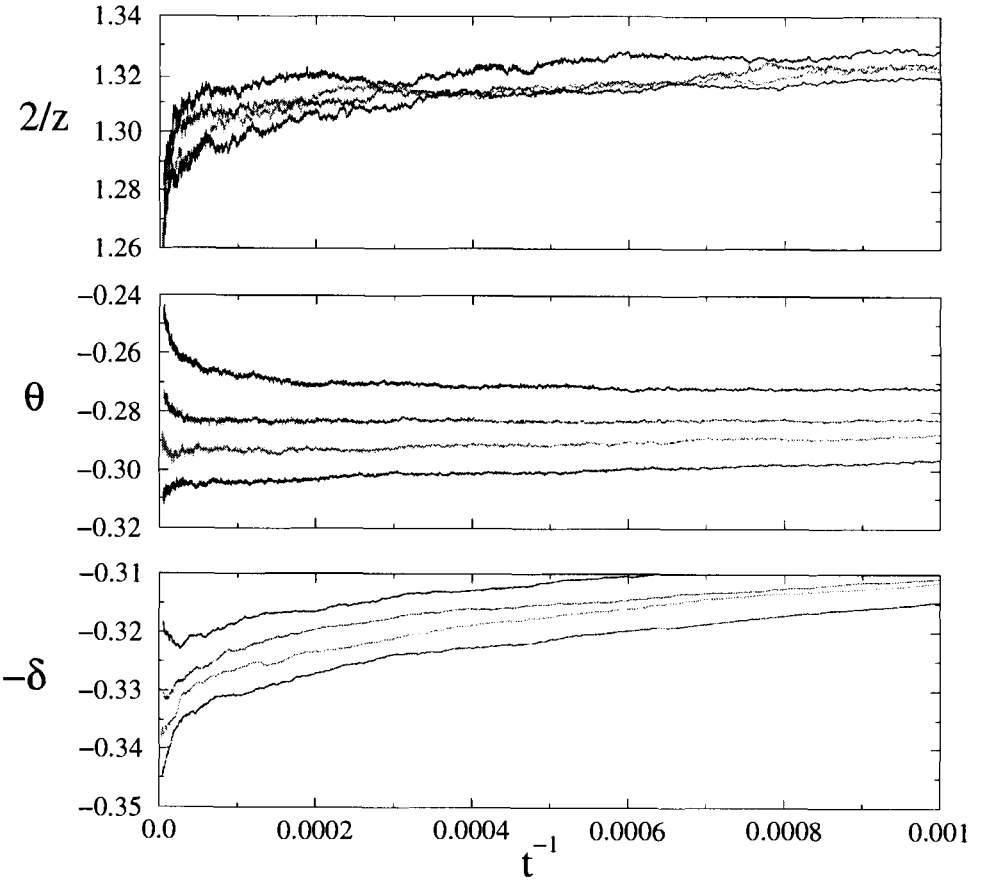


Figure 5.6: The effective local exponents, as in equation (5.5), for $\sigma = 1.6$. The exponents are plotted against $1/t$ to extract the $t \to \infty$ limit. The curves correspond to values of $p$, from top to bottom, of 0.985, 0.988, 0.99, and 0.992.

done here, $b = 5$ was used. This local exponent was then plotted as a function of $1/t$. At the critical point, this should yield a straight line for small $1/t$, with the $t \to \infty$ value the estimated asymptotic exponent, while away from $p_c$ the fact that these quantities do not behave as power laws produces curvature in the plot. Figure 5.6 shows an example of this analysis, for $\sigma = 1.6$.

As can be seen in figure 5.6, there appears to be some curvature in the local values of the exponents for any value of the hopping probability $p$. This made it difficult to determine the exponents to any better accuracy than done here. The values shown in table 5.2 are the best values, with the error the range to the values that are definitely

above and definitely below the transition.

| $\sigma$ | $p_c$ | $\delta$ | $\theta$ | $z$ |
|---|---|---|---|---|
| 1.525 | 0.997(2) | 0.32(1) | -0.30(1) | 1.53(2) |
| 1.55 | 0.992(4) | 0.32(2) | -0.30(2) | 1.53(2) |
| 1.6 | 0.990(2) | 0.33(2) | -0.30(2) | 1.56(2) |
| 1.65 | 0.974(2) | 0.32(2) | -0.26(2) | 1.55(2) |
| 1.7 | 0.955(2) | 0.32(2) | -0.24(2) | 1.59(2) |
| 1.8 | 0.918(2) | 0.32(2) | -0.18(2) | 1.59(2) |
| 1.9 | 0.863(2) | 0.32(2) | -0.14(1) | 1.63(2) |
| 2.0 | 0.804(1) | 0.305(5) | -0.085(5) | 1.68(2) |
| 2.5 | 0.6185(2) | 0.285(5) | -0.005(5) | 1.72(1) |
| RW | 0.5104(2) | 0.287(3) | 0.001(3) | 1.74(1) |

Table 5.2: The measured critical probabilities and exponents for various values of $\sigma$. The number in parentheses is an estimate of the error in the last figure. The row labeled RW gives the results for normal diffusion, with a nearest-neighbour random walk.

The data presented in table 5.2 and shown in figure 5.7 are consistent with a value very close to $\sigma = \sigma_c'(d = 1) = 3/2$ for the emergence of the critical Lévy annihilation phase at nonzero branching. This is in good agreement with the one loop result for $y_\mu$ in section 4.2, and provides some evidence that this one loop result may in fact be exact, as it was for the normal diffusion case.

The measured exponents changed by rather small amounts over the range of $\sigma$ studied. As discussed in chapter 4, the exponents at $\sigma = \sigma_c'(d = 1)$, $p = 1$, can be calculated for the pure Lévy annihilation model, and, assuming $\sigma_c'(d = 1) = 3/2$, are given by $\delta = -\theta = 1/3$, $z = 3/2$. If the exponents are to change monotonically as $\sigma$ is varied, then they are confined to a relatively small range of values between the exponents for branching and annihilating particle model with normal diffusion and those for pure annihilation with Lévy flights.

The numerical evidence is consistent with a smooth movement of the critical value $p_c$ away from unity as $\sigma$ is increased above 3/2 (see figure 5.7). Although a discontinuous jump in $p_c$ at around $\sigma = 3/2$ cannot be completely ruled out, any such

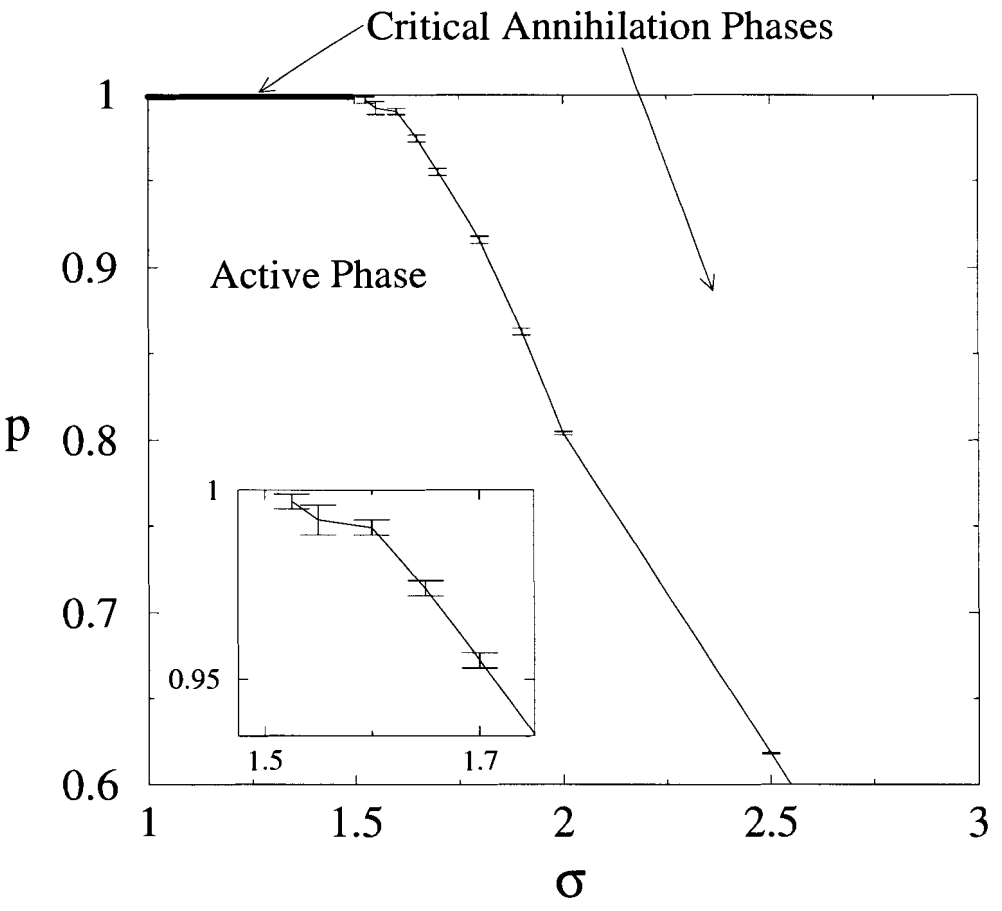


Figure 5.7: Phase diagram for the system of branching and annihilating random walkers with power-law hopping in $d = 1$. The inset shows a blowup of the region near $\sigma_c'(d = 1)$.

jump would have to be smaller than about $10^{-3}$. This finding has consequences for the analogous short-ranged model. In that case the analogue of the point at $\sigma = \sigma_c'(d = 1) \approx 3/2$ is the second critical dimension found at $d_c' \approx 4/3$. The uncontrolled truncated loop expansion used to analyse this point in [11] predicted a discontinuous jump of the critical point as dimension $d$ is lowered through $d_c'$. However, the above numerical evidence would indicate that a smooth movement of the critical point is more likely. Given the uncontrolled nature of the truncated loop expansion, any failure to accurately capture the behaviour close to $d_c'$ would not, perhaps, be very surprising. Nevertheless, these results provide numerical evidence for one of the

main conclusions of reference [11], the presence of a second critical dimension $d_c'$.

### 5.2.2 Steady-State Simulations

Additional simulations were done beginning with a fully occupied lattice of $10^7$ sites. Figure 5.8 shows the time dependence of the density of particles in this kind of simulation. This figure shows results for normal diffusion, in which each particle moves a single site in each timestep. For $p < p_c$, the density reaches a constant value. For $p > p_c$, the density decays with the same power law as it does in a system of particles which have only an annihilation reaction, and for $p = p_c$, the decay is a different power law. This figure can be compared to the mean-field result shown in figure 1.1. The two figures are qualitatively similar, although the mean-field treatment does not yield the correct exponent for the decay at criticality, and does not predict the phase corresponding to the pure annihilation fixed point. The renormalization group treatment of chapter 4 does predict a range of values of the branching rate over which an active phase should appear, and also that the density decay in this region should be governed by the same exponent as the density decay in a model with only an annihilation reaction. The renormalization group treatment done here does not predict the value of the exponent governing the density decay at the critical point, where the branching reaction first becomes a relevant perturbation.

Figure 5.8 clearly shows the behaviour predicted by the analytic calculation. The top two curves show the density decaying to its steady-state value, which depends on the probability of branching. The third curve shows the density decaying, apparently as a power law for the entire length of the simulation. The lowest two curves show the density decaying to zero, with the same power law as in the model with annihilation alone.

On the "active" side of the transition, below $p_c$, the number of particles decays to a steady-state value. To compare with the renormalization-group results of chapter 4, this steady-state density was determined for several values of $\sigma$ close to 1 and for $p$ close to 1. The dependence of this steady-state density on the distance to the critical point can then be used to determine the exponent $\beta_{\text{dens}}$. This exponent should be

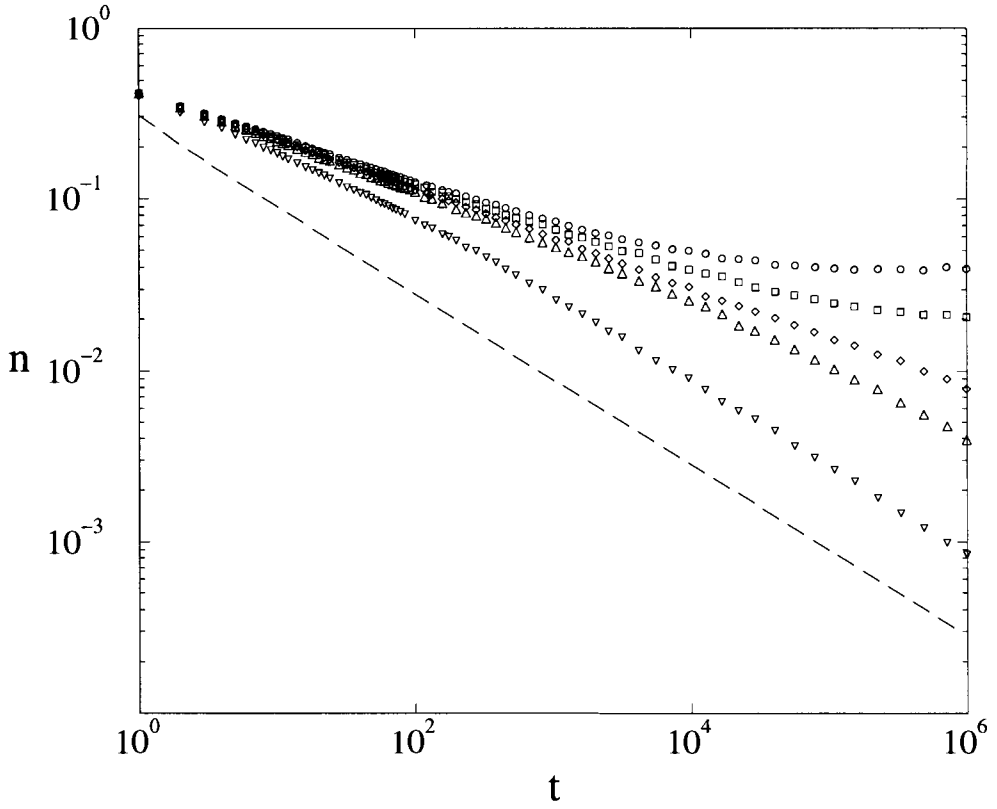


Figure 5.8: The density of particles as a function of time for branching and annihilating random walkers, with normal (single-site steps each timestep) diffusion. The probability of branching decreases from top to bottom. The dashed line shows simulation results for the the annihilation reaction only.

given, to lowest order, by the renormalization-group results for $\sigma < 1.5$, before the point at which the branching rate becomes irrelevant. The renormalization group predection for $\beta_{\text{dens}}$ is $\beta_{\text{dens}} = 1/(3 = 2\sigma$. The results of these simulations are shown in table 5.3, with calculated values for $\beta_{\text{dens}}$ shown for comparison.

The values measured in simulations differed from the analytic results by between 5 and 25%. There are several possible reasons for this discrepancy. First, for small $\sigma$, finite size effects may become more important; the power-law tails of the hop length distributions mean that it is possible for the particles to wrap around the system in a short time, and so appear in positions that are closer to their original location than they should be. Second, as $\sigma \rightarrow \sigma_c$, $\beta_{\text{dens}}$ becomes large, and so the steady-state

| $\sigma$ | $\beta_{\text{dens}}$ (measured) | $\beta_{\text{dens}}$ (theory) |
|---|---|---|
| 0.7 | 1.0 | 1 (mean field) |
| 0.9 | 1.1 | 1 (mean field) |
| 1.1 | 1.3 | 5/4=1.25 (one loop) |
| 1.3 | 1.8 | 5/2=2.5 (one loop) |

Table 5.3: The exponent $\beta_{\text{dens}}$ determined in simulations of the steady-state density of a system of size $10^7$, close to $p_c$.

density changes rapidly near $p_c$. This then means that to cover a reasonable range in $p$, systems with very small steady-state densities must be studied, which in turn means both that long runs must be done to reach these densities, and that there are large fluctuations, which must be averaged over. Another possible source of error is the use of a power law distribution of step lengths for these simulations, rather than the distributions used in the simulations of the pure annihilation model, which more closely resemble a Lévy distribution. While the density for the power law distribution should become the same as that observed with a Lévy distribution with the same power law tail, there may be a long crossover which these simulations could have missed.

## 5.3 Conclusions

In the previous chapter, renormalization group methods were used to provide a characterization of the universal behaviour of several different reaction-diffusion systems, with anomalous diffusion. In these calculations several strong predictions about the behaviour of these systems were made. For the problem with annihilation alone, the exact exponent of the density decay and an $\epsilon$-expansion for the amplitude of this decay could be calculated. For the problem with both branching and annihilation reactions, the renormalization group results predict the existence of a threshold for the appearance of an absorbing phase as either the dimensionality or the power law tail of the step length distribution are varied. These results also provide an estimate

for the value of the exponent governing the steady-state density close to the critical point, for some values of $\sigma$.

The simulations described in this chapter provide confirmation of these predictions for a specific model. The power law decay at the critical point with annihilation alone has the exponent predicted by the renormalization group, and the $\epsilon$-expansion can be used as an approximation to the amplitude valid close to $\epsilon = 0$. Since the use of anomalous diffusion makes it possible to vary the critical dimension, this régime of small $\epsilon$ may be explored in a simulation. The renormalization group prediction of the appearance of an absorbing phase for non-zero branching rate as $\sigma$ is varied is also observed in simulations, at exactly the value of $\sigma$ predicted. The agreement with the prediction for $\beta_{\text{dens}}$, the exponent controlling the steady-state density, shown in table 5.3 is less impressive; this may be due to important higher order terms, or may be due to simulation problems.

These results show that renormalization group methods are an effective tool to classify the behaviour of some systems far from equilibrium. The use of anomalous diffusion here makes it possible to examine regions of parameter space which would not be otherwise accessible to simulation and to examine the region of small $\epsilon$, to make stringent comparisons between analytic and simulation results. The simulations also provide numerical estimates of the values of critical exponents at the critical point which emerges at large values of $\sigma$, and is not accesible to the renormalization group calculation done here.

# Chapter 6

# Rheology

## 6.1 Introduction

Any material will respond to an external force. A viscous fluid will flow at a rate proportional to the force, while an elastic solid will deform with the extent of deformation proportional to the force. In an elastic solid, all the energy added by an external force is stored, and may be recovered when the force is released. In a viscous fluid, all the energy added is dissipated as heat. Between these two idealized extremes are viscoelastic materials, which exhibit both behaviours, storing some added energy and dissipating some. In fact, any material can exhibit both the flow characteristic of a fluid and the elastic deformation characteristic of a solid when probed with forces at different frequencies. It is perhaps better to speak of viscous or elastic behaviour of a material in a certain situation, rather than characterizing a material as viscous or elastic.

The study of the mechanical properties of viscoelastic materials under flow is called rheology. The goal of a theory of the rheology of a material is a constitutive relation between the stress imposed on a sample and its rate and state of deformation, or strain. Different relations express either the stress in terms of the strain or the strain in terms of the stress; these two approaches are useful in different situations. In some cases, it is not enough to specify the current state of either the stress or the strain to determine the other; the relation between them may depend on the

history of the material studied. There is a general formalism used to describe these relations, which will be discussed in this chapter. There are several books which discuss rheology; those consulted while writing this chapter include [46], [47] and [48]. Some rheological phenomena specific to soft materials are discussed in [49].

The external forces on a volume element of a sample are described by the stress tensor $\sigma$. The element $\sigma_{ij}$ of the stress tensor gives the force in the $\hat{i}$ direction on a unit area with a normal pointing in the $\hat{j}$ direction. Similarly, the deformation, or strain, of a volume element is described by another tensor, $\gamma$.

In most of the rest of this chapter, we will be interested in shear deformations only, with shear deformation in only one plane. As is often done in the rheological literature, we will use $\sigma$ to denote not the entire stress tensor, but the non-zero off-diagonal element $\sigma_{xy}$, and similarly $\gamma$ will denote the only non-zero elements of the deformation tensor, $\gamma \equiv \gamma_{xy} = \gamma_{yx}$.

## 6.2 Shear Flow

If a fluid is placed between parallel plates and the plates are pulled in opposite directions, the fluid will flow in response to this shear stress. The velocity of the fluid at each plate should be equal to that of the plate, as no-slip boundary conditions apply to most fluids. There must then be a gradient in the fluid velocity in the $y$ direction, normal to the plates. This flow pattern is called planar Couette flow, or simple shear flow. If the fluid has a non-zero viscosity, the velocity of each plate will be proportional to the applied force, for small enough forces. As particles move in the $y$ direction, their velocities in the $x$ direction change to that of the local flow velocity, and so there must be forces acting on them to maintain the velocity gradient. The energy supplied to the fluid by the external forces causes every velocity component to increase, and so is dissipated as heat. In an experiment, the fluid may be maintained at constant temperature by contact with a reservoir at the boundary.

The forces applied to the fluid are given by the stress tensor $\sigma$. Here we will consider only shear flow, with $\sigma_{xy}$ the only non-zero off-diagonal element of $\sigma$. For small flow rates, the relation between the flow rate and the stress is linear. The shear

flow rate $\dot{\gamma} = \frac{\partial v_x}{\partial y}$ is then related to the shear stress by

$$\sigma_{xy} = \eta\dot{\gamma}, \tag{6.1}$$

where $\eta$ is the coefficient of shear viscosity of the fluid.

## 6.3 Linear Viscoelasticity

For most materials, there is a region of linear response, where the theory of linear viscoelasticity describes the behaviour of the material under strain. In the linear regime, a superposition principle holds: if a stress can be written as a sum of two other stresses, then the response to the total stress is given by the sum of the responses to the smaller stresses.

As a step toward the goal of a general constitutive equation, rheologists determine the relationship between stress and strain for several simple situations. In the linear regime, this leads to a number of rheological functions describing a material. Each of these functions contains all information about the shear flow properties of the material, but different functions are useful in different situations. In the next section, we will discuss some of these rheological functions.

### 6.3.1 Rheological Functions

One simple deformation is a single step in the strain, so that the strain is zero before $t = t_0$ and some finite value $\gamma_0$ for $t > t_0$. In this case, the stress will be related to the strain by

$$\sigma(t) = G(t - t_0)\gamma_0, \tag{6.2}$$

where $G(t)$ is some function characterizing the material studied called the relaxation modulus. This form is required by the assumption that the stress and strain are linearly related and by the assumption that the material is in equilibrium before the deformation occurs. As long as the material is in equilibrium, $G$ cannot depend on $t_0$ alone, only on the time since the deformation occurred. $G(t)$ is zero for $t < 0$, as the relation between stress and strain must be causal.

If a general time-dependent deformation $\gamma(t)$ is made, the stress will be given by

$$\sigma(t) = \int_{-\infty}^{t} \mathrm{d}t' G(t-t')\dot{\gamma}(t'). \tag{6.3}$$

To derive (6.3), the strain history $\gamma(t)$ may be broken into intervals during which the strain is constant, and the stress response to this strain will be given by (6.2). These stresses may then be added using the superposition principle, as long as the material is studied in the linear regime.

In some experiments, the strain is an oscillating function at frequency $\omega$. As is often done, oscillatory functions are represented by complex exponentials, so $\gamma(t) = \gamma_0 e^{i\omega t}$. Calculations are carried out in the complex domain, and the real part is taken at the end of the calculation. In rheological literature this is not explicitly stated, but it is understood that all quantities must be real. The stress is then given by

$$\sigma(t) = G^*(\omega)\gamma_0 e^{i\omega t}. \tag{6.4}$$

In (6.4), $G^*$ is a complex shear modulus, given by

$$G^*(\omega) = i\omega \int_0^{\infty} \mathrm{d}t G(t) e^{-i\omega t}. \tag{6.5}$$

The factor $i\omega$ appears because $\gamma(t)$ rather than $\dot{\gamma}(t)$ appears in (6.4). Here, $G^*(\omega) \equiv G'(\omega) + iG''(\omega)$ (with $G'$, $G''$ real functions of $\omega$) is a complex function of the frequency. The stress required to produce a specified strain will, in general, have both in-phase and out-of-phase components. $G'(\omega)$ is called the storage modulus, or dynamic rigidity, and gives the in-phase response, while $G''(\omega)$ is called the loss modulus. The energy dissipated as heat in an oscillatory shear experiment is related to $G''(\omega)$.

There are many other equivalent ways of describing the rheological behaviour of a material. For example, one could specify the complex viscosity $\eta^*$, where the stress in oscillatory shear is given by

$$\sigma(t) = \eta^*(\omega)\dot{\gamma}(t), \tag{6.6}$$

so that $\eta^*$ is given by $\eta^* = G^*/i\omega$. Simply writing $\gamma$ in terms of $\sigma$ gives another rheological function, the complex creep compliance,

$$\gamma(t) = J^*(\omega)\sigma(t). \tag{6.7}$$

The creep compliance $J(t)$ describes the motion of a sample after a step increase in strain; $\gamma(t) = J(t)\sigma_0$ if $\sigma(t)$ is a step function of height $\sigma_0$ at $t = 0$.

Finally, one could specify part of the complex modulus, typically $G'(\omega)$, and the loss angle $\delta$, defined by

$$\tan\delta = \frac{G'}{G''}. \tag{6.8}$$

The loss angle gives the phase shift between the stress and the strain, so that if $\gamma(t) \sim e^{i\omega t}$, then $\sigma(t) \sim e^{i(\omega t+\delta)}$, or, equivalently, $G^*(\omega) = f(\omega)e^{i\delta}$.

### 6.3.2 Modelling

One way to model the possible responses to a stress history is to write a differential equation relating the stress and the strain [46, 47], though treatments of linear viscoelasticity quickly move beyond this description. A general form of this relationship is

$$\left(1 + \alpha_1\frac{\partial}{\partial t} + \alpha_2\frac{\partial^2}{\partial t^2} + \ldots + \alpha_n\frac{\partial^n}{\partial t^n}\right)\sigma = \left(\beta_0 + \beta_1\frac{\partial}{\partial t} + \beta_2\frac{\partial^2}{\partial t^2} + \ldots + \beta_m\frac{\partial^m}{\partial t^m}\right)\gamma \tag{6.9}$$

with $n = m$ or $n = m - 1$. A Hooke's law elastic solid is given by the special case $\beta_0 = G$, with all other parameters zero, so that $\sigma = G\gamma$, while a Newtonian fluid is given by the special case $\beta_1 = \eta$, so $\sigma = \eta\dot{\gamma}$.

A slightly more complicated model is the Maxwell model, with $\beta_1 = \eta$ and $\alpha_1 = \tau$. This describes a viscoelastic fluid with a single relaxation time $\tau$. The stress and strain are then related by solving

$$\sigma + \tau\dot{\sigma} = \eta\dot{\gamma}. \tag{6.10}$$

This is solved by

$$\sigma(t) = \frac{\eta}{\tau}\int_{-\infty}^{t} \mathrm{d}t' e^{-(t-t')/\tau}\dot{\gamma}(t'). \tag{6.11}$$

The relaxation function for the Maxwell model is then

$$G(t) = \frac{\eta}{\tau}e^{-t/\tau}, \tag{6.12}$$

while the complex modulus $G^*$, from 6.5, is

$$G^* = \frac{i\omega\eta}{1 + i\omega\tau}. \tag{6.13}$$

The real part of $G^*$,

$$G' = \frac{\eta\tau\omega^2}{1 + \omega^2\tau^2}, \tag{6.14}$$

has a high frequency limit $G'(\omega \to \infty) = \eta/\tau$, showing that at high frequencies a Maxwell material behaves like an elastic solid with a shear modulus $G = \eta/\tau$. The real part of the complex viscosity,

$$\eta'(\omega) = \frac{\eta}{1 + \omega^2\tau^2}, \tag{6.15}$$

has a low frequency limit $\eta'(\omega \to 0) \to \eta$, so the Maxwell material behaves like a viscous fluid at low frequencies.

Each of the differential equations describing a rheological model has a mechanical model equivalent. The mechanical models are equivalent to the rheological ones in the sense that the relation between the force applied to and the extension of the mechanical model is the same as the relation between the stress and the strain of the rheological model. In the case of the Maxwell model, the mechanical equivalent is given by a spring and a dashpot (in which the applied force and the rate of extension are proportional) attached in series. This can then be generalized by attaching springs and dashpots with different spring constants and relaxation times together, in a variety of ways. It can be shown that any one of these general models is equivalent to a generalized Maxwell model, in which pairs of springs and dashpots in series are attached in parallel. The stress is given by summing the contributions of these elements:

$$\sigma = \sum_i^n \frac{\eta_i}{\tau_i} \int_{-\infty}^t \mathrm{d}t' e^{-\frac{(t-t')}{\tau_i}} \dot{\gamma}(t') \tag{6.16}$$

With a finite number of Maxwell modes, the generalized Maxwell model is often used as a fitting form to represent experimental data. This form may also be generalized to a continuous spectrum of relaxation times, so that the stress is given by the integral

$$\sigma(t) = \int_0^\infty \mathrm{d}\tau \frac{N(\tau)}{\tau} \int_{-\infty}^t \mathrm{d}t' e^{-(t-t')/\tau} \dot{\gamma}(t'), \tag{6.17}$$

where $N(\tau)\mathrm{d}\tau$ is the contribution to the viscosity of the material of the Maxwell modes near $\tau$. A relaxation function $\phi(t)$ is defined as

$$\phi(t-t') = \int_0^\infty \mathrm{d}\tau \frac{N(\tau)}{\tau} \exp(-(t-t')/\tau), \tag{6.18}$$

so that

$$\sigma(t) = \int_{-\infty}^{t} \mathrm{d}t' \phi(t-t')\dot{\gamma}(t'). \tag{6.19}$$

Comparing this with equation 6.3, it can be seen that $G(t) = \phi(t)$ in the linear regime. This does not constrain the possible form for $G(t)$; almost any $G(t)$ may be obtained with the correct choice of $N(\tau)$.

### 6.3.3 Useful Limits

The response of the material to certain external perturbations is given by the relaxation function $G(t)$. This generalizes the usual shear viscosity and shear modulus, which give the relations between stress and either strain rate or strain when they are independent of time. The relaxation function contains these static material properties in certain limits. The shear viscosity is defined in steady shear, when $\dot{\gamma}$ is constant. In this case, from equation (6.3), $\sigma(t) = \dot{\gamma}\int_{-\infty}^{t} \mathrm{d}t' G(t-t')$. The viscosity is given by the ratio of the steady state stress to the steady state shear rate, if both are small and time-independent, so the shear viscosity is

$$\eta \equiv \frac{\sigma}{\dot{\gamma}} = \int_0^\infty \mathrm{d}t G(t) = \lim_{\omega\to 0} G^*(\omega)/i\omega = \lim_{\omega\to 0} \eta^*(\omega). \tag{6.20}$$

Similarly, the static shear modulus $G$ is defined when the ratio of the shear stress to the strain is constant. If there is a steady state value of $G$, then $G(t)$ as defined in equation (6.2) must approach a constant at large $t$, and

$$G = \lim_{t\to\infty} G(t). \tag{6.21}$$

Most fluids have a largest relaxation time $\tau$, so that for large $t$ the relaxation modulus depends on $t$ as $G(t) \sim e^{-t/\tau}$. This then implies that at low frequencies $G' \sim \omega^2$ and $G'' \sim \omega^1$. This behaviour can be seen in the Maxwell model above.

## 6.4 Non-linear Viscoelasticity

The linear effects described above were first investigated by Newton, and a fluid exhibiting only these effects is known as a Newtonian fluid. If the deformation imposed on a sample becomes large enough, the linear theory described above no longer applies, and non-Newtonian effects appear. This can occur for oscillatory deformations if the amplitude of the oscillations is large, or for steady flow if the flow rate is high.

For a relatively simple fluid, such as water, the non-Newtonian regime cannot be reached at experimentally accessible rates of continuous flow. Only in computer simulations can this regime be seen. For complex fluids, such as colloidal suspensions, polymer melts, and gelling materials, the non-linear regime can be studied in experiments.

The theory of non-linear viscoelasticity is significantly less well developed than the linear theory; most of what is known about non-linear viscoelastic media is phenomenological. In the non-equilibrium molecular dynamics simulations described in chapter 9, only the non-linear regime may be explored, as the flow rate must be very high to produce a noticeable signal in the short time of the simulation. We will, therefore, briefly discuss some of what is known about the non-linear viscoelastic regime.

### 6.4.1 Non-linear Flows

In a fluid driven beyond the linear regime, the shear stress is no longer required to be a linear function of the shear rate. This is described by introducing a shear-rate-dependent viscosity $\eta(\dot{\gamma})$, so the relation between stress and strain in steady shear flow is now

$$\sigma = \eta(\dot{\gamma})\dot{\gamma}. \tag{6.22}$$

Calculation of $\eta(\dot{\gamma})$ for a general fluid is difficult. There are several approaches which attempt to constrain the possible form of $\eta(\dot{\gamma})$ on very general grounds, which are discussed in books on rheology [46, 47]. These approaches are sufficiently general so

as to allow a wide range of possible functions. However, there are several phenomenological forms which are often used to fit data. One of the more common is the Cross equation

$$\frac{\eta(\dot{\gamma}) - \eta_\infty}{\eta_0 - \eta_\infty} = \frac{1}{1 + (K\dot{\gamma})^m}. \tag{6.23}$$

This form will be used to extrapolate shear-rate-dependent viscosities determined in simulations to zero shear rate.

Another non-linear effect which is observed in complex fluids is the development of normal stress differences. In an equilibrium fluid all of the diagonal elements of the stress tensor must be equal. To linear order in the shear rate, this must still be true, as a change in the sign of the shear rate should not change the sign of the diagonal elements of the stress tensor. Normal stress differences must then appear only to order $\dot{\gamma}^2$. If the overall pressure is fixed, two normal stress differences may be defined in 3 dimensions. These are known as the first and second normal stress differences:

$$N_1 = \sigma_{xx} - \sigma_{yy}, \qquad N_2 = \sigma_{yy} - \sigma_{zz}. \tag{6.24}$$

Since $N_1$ and $N_2$ must be of order $\dot{\gamma}^2$ or higher, the properties of the material are usually characterized by specifying the first and second normal stress coefficients, defined by

$$N_1 = \Psi_1\dot{\gamma}^2, \qquad N_2 = \Psi_2\dot{\gamma}^2. \tag{6.25}$$

For many materials, these normal stress coefficients are in fact observed to become constants at low shear rates [50]. At higher shear rates, the normal stress coefficients become functions of $\dot{\gamma}$, just as $\eta$ does.

# Chapter 7

# Gels

The phenomenology of the gel transition is reviewed in this chapter. The model used to describe the structure of a gel, percolation theory, is discussed in the first two sections. In sections 7.3 and 7.4 the formation and viscoelastic properties gels are discussed, while the results of other theoretical approaches are given in section 7.5.

## 7.1 Percolation

A common model to describe the microscopic structure of a disordered material is the percolation model. In this model, a perfect lattice is diluted by the random deletion of sites or bonds between sites. Removal of sites is called site percolation, while removal of bonds is called bond percolation. Most of the important quantities are independent of which model is chosen, and in this thesis we will discuss only bond percolation. Each bond is taken to be present in the diluted lattice with probability $p$, which is the only control parameter of the model. Each bond is taken to be present or absent as an independent random variable, with no correlations between bonds. The behaviour of various geometric quantities of the remaining set of bonds resembles in many ways the behaviour of physical properties near a phase transition. There is a critical bond probability, $p_c$, above which there is always a percolating cluster, meaning that there is a cluster of lattice sites connected by bonds which extends from one side of the lattice to the other. This transition is only sharp in the thermodynamic limit, where

the system size $L$ goes to infinity; for finite $L$, the transition is rounded off. Below the critical point, there exist only finite clusters. These clusters have a characteristic size $\xi$, which depends on the distance from the critical point, and follows a power law, $\xi \sim (p - p_c)^{-\nu}$. This correlation length is defined by the probability that a site a distance $x$ away from a chosen site belongs to the same connected cluster. The similarity between this model and critical phenomena in statistical physics has led to intensive study of percolation theory, as an example of an easily understood model. The percolation problem can, in fact, be mapped onto a limit of a standard model in statistical mechanics, the $q = 1$ limit of the $q$-state Potts model [21]. Much more about the percolation problem can be found in several books [51] and [52]; a brief description of some facts about this problem, including the mapping to the Potts model, may be found in [53].

In addition to the correlation length $\xi$, all other geometric properties of the model scale as powers of the distance from the critical point. This gives a set of critical exponents which are universal, in the sense that they do not depend on the details of the model. The exponents of site and bond percolation are the same, and the exponents do not depend on the lattice which has been chosen for dilution. As in thermal critical phenomena, there is an upper critical dimension above which all exponents take on mean field values. For the percolation problem, the upper critical dimension is 6, so the physical dimension, 3, is far from the critical dimension. Mean field exponents are also realized on another lattice, the Bethe lattice. A Bethe lattice, also known as a Cayley tree, has a tree-like structure. Each vertex is attached to a fixed number of branches, but there are no loops formed of bonds connected to each other.

Not all of these exponents describing the geometric structure are independent; there exist several scaling relationships between them. These scaling relations should apply not only to networks constructed by independently adding bonds between neighbouring sites but also to other networks of bonded sites. These scaling relations reduce the number of independent exponents describing the static structure of percolation clusters to two. Once two exponents have been measured, the universality class of the structure is fixed.

| | definition | $d = 2$ | $d = 3$ | Mean Field |
|---|---|---|---|---|
| $\alpha$ | $N \sim \lvert p - p_c \rvert^{2-\alpha}$ | -2/3 | -0.62 | -1 |
| $\beta$ | $P \sim (p - p_c)^{\beta}$ | 5/36 | 0.41 | 1 |
| $\gamma$ | $S \sim \lvert p - p_c \rvert^{-\gamma}$ | 43/18 | 1.8 | 1 |
| $\nu$ | $\xi \sim \lvert p - p_c \rvert^{-\nu}$ | 4/3 | 0.88 | 1/2 |
| $\sigma$ | (see caption) | 36/91 | 0.45 | 1/2 |
| $\tau$ | $n_s \sim s^{-\tau}$ at $p_c$ | 187/91 | 2.18 | 5/2 |

Table 7.1: The values of the exponents governing various structural quantities in the percolation problem. $N$ is the total number of clusters, $P$ is the probability that a randomly chosen site belongs to the infinite cluster, $S$ is the mean cluster size, $\xi$ is the correlation length, and $n_s$ is the number of clusters of $s$ connected sites. $\sigma$ controls the cluster size distribution away from $p_c$, with $n_s \sim s^{-\tau} e^{-cs}$, and $c \sim \lvert p - p_c \rvert^{1/\sigma}$. There is thus a cutoff in the cluster size distribution, with a characteristic cluster size which scales as $M_{\text{char}} \sim \lvert p - p_c \rvert^{-1/\sigma}$.

## 7.2 Modelling Materials

Once a random structure has been constructed, by deleting bonds from a regular lattice in a completely uncorrelated way or by some other method, the resulting structure may be used as a model for a disordered material. The earliest use of percolation theory was to study randomly packed grains, like coffee in a filter, through which a fluid could pass if there was a spanning cluster of open space between grains. This picture of fluid flow through randomly connected channels has also been used to model the motion of oil through sand. The same diluted lattice has also been used as a model for a conductor with random insulating impurities. The bonds are taken be conducting, and the dependence of the conductivity of a sample on the number of impurities may be calculated from the dependence of the resistance on the number of bonds. The percolation model has also been used to model the structure of a material close to its gel point, at which it experiences a transition from a liquid to a solid. The predictions of this model will be discussed in the rest of this thesis.

In the percolation picture of a randomly linked fluid, the sites of a lattice are taken to be the monomers that will make up the crosslinked material. At low $p$, a

few monomers are bonded into dimers and trimers. As $p$ increases, larger and larger clusters are formed, forming branched polymers. Eventually a single giant molecule spans the entire reaction vessel. At this point, the crosslinked material has formed a disordered solid state. Since the bonding process is taken to occur between each pair of neighbouring sites completely independently, the scaling of the geometric properties of the large molecules in the fluid state and the spanning cluster in the solid state are given by the critical exponents of percolation theory. In the next few sections, we will discuss the experimental results on the scaling of these geometric properties and how well approximated they are by the predictions of percolation theory, as well as results of experiments measuring the viscoelastic properties of these crosslinked materials.

## 7.3 Gels

Gels are divided into two classes, chemical gels and physical gels, according to the nature of the crosslinks between monomers. Chemical gels are created when the monomers form permanent covalent bonds and are stable against changes in thermodynamic parameters. Physical gels are formed when the bonds between the units which make up the gel are due to some other physical mechanism. Since the bonds are not chemical bonds, they may be destroyed by changes in thermodynamic parameters such as temperature; physical gels are often called "reversible" or "weak" gels. For example, in block copolymers one of the blocks may phase segregate and create junctions linking different polymer chains. Physical gels can also arise through the formation of microcrystalline regions containing parts of several polymer chains, or when several polymer chains form a helix, linking several chains at one point. These gels are often created in solution with a solvent.

The materials the structure of which is best described by percolation theory are gels made from the polycondensation of short monomers. We will discuss experiments on several of these. A large number of experiments have been performed to study the structural exponents of gelling materials, almost all on the sol side. See p. 130 in [54] for a list of experimental exponent values, most consistent with the theoretical predictions. It seems that at least some gels have structures which are described by

percolation theory.

### 7.3.1 Gel Formation

The fact that the structure of some gels is well described by percolation is not *a priori* obvious. In some ways, the gelation process is much like percolation: bonds between the elements which make up the gel are added randomly, and it seems likely that there is very little correlation between the presence or absence of two possible bonds. However, during the gelation, these elements are moving, and so the structure of a gel might be expected to resemble that created by the aggregation of particles. There are several models of aggregation which produce different static structures. However, these models do not seem to describe gels. Martin and Adolf [55] describe a theoretical model of an aggregation process in which aggregation of clusters is governed by a Smoluchowski equation for the time-evolution of the number $N_m$ of clusters of size $m$,

$$\frac{\mathrm{d}N_m}{\mathrm{d}t} = \frac{1}{2}\sum_{i+j=m} N_i K_{ij} N_j - N_m \sum_{j=1}^{\infty} K_{ij} N_j. \tag{7.1}$$

The rates for the reactions of clusters of size $i$ and $j$ are given by the kernel $K_{ij}$. Since this Smoluchowski equation contains a set of undetermined rates, many different structures may be obtained by varying these rates. If a structure so obtained does obey a scaling relation, the static exponents describing the cluster size distribution is likely to differ from those of percolation. The Smoluchowski theory does not make strong predictions about the structure of the clusters formed in gelation.

From the Smoluchowski equation, it is difficult to see why so many gels have structures which are described by percolation theory. The Smoluchowski approach does have some limitations. It is a mean-field approach, in which fluctuations are neglected, and contains no information about the spatial motion of the clusters. Another physical feature which is not included in the Smoluchowski description is the fact that close to the gel point, as the viscosity becomes large, the motion of molecules and clusters of molecules becomes very slow. This may explain why the percolation model, in which crosslinking happens much faster than the motion of particles, describes the structure of gels. It is possible that a more complete description of the

gelation process may help to explain the usefulness of percolation theory.

## 7.4 Experiments on Viscoelastic Properties of Gels

While the static structures of at least some systems close to the sol-gel transition seems to be well described by percolation theory, the situation for the exponents describing the dynamic properties of these systems is far less clear. Systems with similar static properties seem to have quite different dynamics. In most cases, the dynamic properties are observed to behave as power laws close to $p_c$, with $\eta \sim (p_c - p)^{-s}$ on the fluid side of the transition, the shear modulus $\mu \sim (p - p_c)^t$ on the solid side, and the dynamic viscosity $G^*(\omega)$ scaling as $\omega^{-u}$ at $p_c$. In this section we will briefly discuss the results of experiments to determine these exponents.

Lusignan *et al.* [56] studied a series of randomly branched polyesters. These branched polymers were prepared from adipic acid and trimethylolpropane. These chemicals form permanent bonds and create a chemical gel. The structure of the samples were characterized by measuring the weight-averaged molecular mass $M_w$, which scales as $(p-p_c)^{-\gamma}$, as well as the largest molecular mass $M_{\max}$. The largest mass $M_{\max}$ as measured in an experiment should be proportional to the characteristic largest mass $M_{\text{char}}$ of clusters in percolation theory, which scales as $M_{\text{char}} \sim (p-p_c)^{-1/\sigma}$. Since it is experimentally difficult to determine the distance to the critical point of a given sample, measuring several different scaling properties is useful in determining exponents in a way which does not require the distance to the critical point to be measured. Using a scaling law, the exponent $\tau$ was determined for these polymers, as $\tau = 2.17 \pm 0.07$, consistent with the exponent for percolation. Further evidence that these polymers had structural properties given by percolation theory came from measurements of the number distribution of polymers of mass $M$. This was fit to a functional form using the percolation values of $\sigma$ and $\tau$ as well as two free parameters setting the overall scale and a characteristic mass, yielding good fits.

The viscoelastic properties of these polymers were determined by oscillatory strain experiments, and by measuring the creep of stressed samples. The exponents were determined to be $s/\gamma = 0.760 \pm 0.038$, $s\sigma = 0.620 \pm 0.076$, $t/\gamma = 1.52 \pm 0.18$,

$t\sigma = 1.23 \pm 0.25$, and $u = 0.659$. Using the percolation values for $\sigma$ and $\gamma$, the dynamical exponents can be extracted, and are shown in table 7.2.

Pectin, which is a biopolymer found in plants and used in making fruit jellies, can form a gel when divalent cations such as calcium are added. The density of crosslinks can be controlled by the concentration of calcium added. This gel is thermoreversible, and so should be classified as a physical gel. However, a strained sample on the gel side of the transition does not relax for several days, indicating that the bonds remain for long times. The fact that the bonds are temporary does mean that it is difficult to characterize the structure of the polymers. It is impossible to dilute the sample, either to separate out polymers of different masses and count them or to perform a scattering experiment. For this system, the structure of the clusters has not been experimentally determined. Axelos and Kolb [57] measured the rheological exponents of a pectin gel near its gel point, using both steady state shear flow and oscillatory measurements; these exponents are shown in table 7.2.

A group of experimentalists in France has performed extensive work on polycondensation of diisocyanate and triol, both with and without solvent, to form a polyurethane gel. Each triol molecule is a trifunctional polymer, which can form bonds with another triol using the difunctional diisocyanate as a bridge. The extent of the reaction, giving the number of crosslinks, was controlled by varying the fraction of diisocyanate. In [58] the authors used neutron scattering on diluted samples to find $\tau = 2.2 \pm 0.04$, and in [59], they used light scattering to find $\gamma = 1.71 \pm 0.06$, consistent with percolation theory. In several other papers [60, 61, 62], they present the results of various measurements of mechanical and viscoelastic properties of these branched polymers. Their results are given in table 7.2.

The same group has performed experiments on styrene formed by radical copolymerization. They seem not to have determined the exponents governing the structural properties of these samples, although in [59] they mention other work on radical copolymerized samples which gave results within experimental error of percolation values. In [60], they present the results of rheological experiments done on several samples of this gel; their results are shown in table 7.2. The results shown in this paper do show considerable scatter in estimated exponent values for different gel samples.

Another group, Devreux *et al.* [63], has performed experiments on a silica gel. A gel was condensed from a silicon alkoxide, called TEOS, in two different catalysis conditions. At low $p$H, they observed a crossover; the behaviour of the dynamical properties far from the gel transition differed significantly from that close to the transition. The exponents found close to the gel transition are given in table 7.2. This group seems not to have determined the exponents characterizing the static structure, and used the gel time as a measure of the distance to the gel point. They assume that the gel time is proportional to the extent of reaction; this assumption is supported by NMR data. The exponent $s$, giving the power-law decay of the complex viscosity, is independent of this assumption, and requires only that the gel point be identified correctly.

| system | $s$ | $t$ | $u$ | Ref. |
|---|---|---|---|---|
| polyester | $1.36 \pm 0.09$ | $2.71 \pm 0.3$ | $0.659 \pm 0.015$ | [56] |
| pectin | $0.82 \pm 0.05$ | $1.93 \pm 0.08$ | $0.71 \pm 0.02$ | [57] |
| polycondensate | $0.8 \pm 0.1$ | $3.2 \pm 0.5$ | $0.70 \pm 0.02$ | [62, 61] |
| copolymer | 0.78 | 2.1 | | [60] |
| silica | $0.7 \pm 0.1$ | $2.0 \pm 0.1$ | $0.73 \pm 0.02$ | [63] |

Table 7.2: A summary of experimentally measured exponents governing rheological properties of a variety of gelling materials.

The experimental results shown in table 7.2 vary from one system to another, and it is difficult to see what the important factors control the divergences of viscoelastic properties close to $p_c$. It is not clear at this point what universality classes should describe these viscoelastic properties. This provides a motivation for the simulations done in this thesis. In simulations, the microscopic structure of the material is known and the macroscopic properties may be calculated extract exponents. With enough simulations it should be possible to identify which microscopic features are important in the determination of macroscopic properties.

## 7.5 Theoretical Models of Dynamic Properties

There have been a number of attempts to calculate the dynamic properties of randomly diluted networks and to relate the exponents governing the viscoelastic properties to those describing the static structure. We will describe several of these approaches here.

### 7.5.1 Dynamic Scaling

Some very general statements may be made on the basis of a dynamical scaling argument given in [54]. This argument should hold for any material for which various measurable quantities follow power laws near the critical point. The argument begins with the assumptions that the zero frequency viscosity and shear modulus scale like $\eta = \eta_0(p_c - p)^{-s}$ and $G = G_0(p - p_c)^t$, as discussed above. It further assumes that there is a crossover frequency, $\omega^*$, corresponding to the largest relaxation time. The crossover frequency goes to zero near the gel point, as $\omega^* = \omega_0|p - p_c|^z$. Below this frequency, the material behaves like a fluid or a solid, depending on which side of the gel transition is being studied. Above this frequency, the material is assumed to have a power law decay in the complex modulus, with $G^* \sim (i\omega/\omega_0)^u$, which can be rewritten in terms of the loss angle defined in chapter 6,

$$G^*(\omega) \sim (\omega/\omega_0)^u e^{i\delta} \tag{7.2}$$

with

$$\delta \equiv \arctan\left(\frac{G'}{G''}\right) = \frac{u\pi}{2}. \tag{7.3}$$

It is usually argued that the power law behaviour of the complex modulus is a consequence of the fractal nature of the gel state. The diverging time scale corresponds to a diverging correlation length, and the structure of the clusters are self-similar below the correlation length, and so may be expected to relax in this way. However, the dynamic scaling argument does not depend on this assumption about the structure and should hold as long as the scaling laws above hold.

Using the scaling of $\omega^*$ to replace $p - p_c$ in the scaling of the viscosity and shear modulus, we get $\eta \sim (\omega^*)^{-s/z}$ and $G \sim (\omega^*)^{t/z}$. But $\omega^*$ is the crossover frequency,

below which liquid-like or solid-like behaviour is seen, so $G'(\omega^*) \sim G \sim (\omega^*)^{t/z}$ on the solid side of the transition, and $G''(\omega^*) \sim \omega^* \eta \sim (\omega^*)^{1-s/z}$ on the liquid side. Above $\omega^*$, both of these quantities scale like $\omega^u$. Matching the scaling behaviour at $\omega^*$, it must be the case that $u = t/z$, and $u = 1 - s/z$. This then leads to two relations between the dynamical exponents:

$$u = \frac{t}{s+t} \tag{7.4}$$

and

$$s + t = z. \tag{7.5}$$

These two relations are often used as a consistency check on experimental and simulation results. Any calculated exponents must obey these relations, as the experimental values in table 7.2 do. The relation in equation (7.3) gives another check, as it implies that the ratio of the high-frequency limits of $G'$ and $G''$ should be related to the critical exponent $u$.

### 7.5.2 Vulcanized Rubber

An early model for a disordered solid is the Flory-Stockmeyer model for vulcanized rubber. This is a mean-field model, so the exponents associated with this model should be observed in a high-enough dimensional space and also may be observed far from the critical point. It is now recognized to be in the same universality class as the percolation problem on a Bethe lattice, where loops of bonded particles cannot occur. De Gennes [64] showed that as the polymer chains between crosslinks become longer the critical region in which non-mean-field exponents are observed becomes smaller. This model should describe the properties of randomly crosslinked long chain polymers but not gels and short chain polymers close to the critical point. In the model studied in this thesis, there is a single spring connecting possible junction points in the network, so the critical region should be large; the classical theory should not apply.

### 7.5.3 The Electrical Analogy

The earliest attempts to determine the numerical values of the dynamic exponents for the materials with structures described by percolation theory were made by de Gennes. He argued that the shear modulus should vanish at $p_c$ in the same way as the conductivity of a random resistor network [65] and suggested that the viscosity should diverge in the same way as does the conductivity of a random mixture of conductors and superconductors [66]. In [67], de Gennes presents an argument intended to show that the viscosity of a network with harmonic interactions between particles behaves in the same way as the polarizability of a random network of superconductors and capacitors, and then argues that the conductivity of a mixture of conductors and superconductors should behave in the same way. These two ideas, relating the shear modulus and the viscosity to properties of electrical networks, are referred to as "the electrical analogy" to viscoelastic media. A proof of the equivalence of resistor networks and networks of zero-rest-length springs was given by [68]. This proof fails for springs of finite rest length. However, renormalization group arguments indicate that finite-rest-length springs are effectively the same as zero-rest-length springs at finite temperature. The exponents describing the conductance properties of resistor networks have been measured using a number of different techniques, as done in [69]. If the electrical analogy is correct, the numerically determined scaling exponents for electrical networks can be directly applied to the viscoelastic media. Their values are given in tables 7.3 and 7.4.

### 7.5.4 Rouse Dynamics

The Rouse model is a simple model of a polymer system. The polymer is modelled as a set of beads connected by springs. There are no hydrodynamic or excluded volume interactions between beads. The effects of all other interactions are modelled by neglecting inertia and, instead, using a local drag on each bead. A random force $\xi$ is used to model fluctuations in the force on each particle. If the particles are under shear flow, this can be included by imposing an overall position-dependent velocity

$\mathbf{v}_{\text{ext}}$. The equation of motion for each bead is then

$$\frac{\partial \mathbf{r}_i(t)}{\partial t} = -\frac{k_B T}{\zeta}\frac{\partial H}{\partial \mathbf{r}_i(t)} + \mathbf{v}_{\text{ext}}(\mathbf{r}(t)) + \xi_i(t), \tag{7.6}$$

where $H$ includes only the forces due to springs linking the beads. A harmonic force $H = \frac{d}{2a^2}\sum_{i,j}\Gamma_{ij}\mathbf{r}_i \cdot \mathbf{r}_j$ is often used. Here $\Gamma$ is the connectivity matrix, with $\Gamma_{ij} = 1$ if particles $i$ and $j$ are connected and zero otherwise. The noise term has the usual delta-function correlation $\langle \xi_i^\alpha(t)\xi_j^\beta(t')\rangle = 2\frac{k_B T}{\zeta}\delta_{\alpha\beta}\delta_{ij}\delta(t-t')$. Without the noise term, the beads relax to a steady state with $\partial H/\partial \mathbf{r} = \mathbf{0}$, and the velocity equal to the externally applied velocity.

Since the Rouse model is so simple, it can be solved exactly for linear chains, and is popular as a first approximation for polymer systems. Randomly crosslinked percolation clusters with Rouse dynamics have been used to model a randomly crosslinked solid. Both simple scaling arguments and rigorous calculations have been done, yielding quite different results. Both of these approaches will be discussed below.

### Scaling Arguments

Attempts to calculate the viscosity of Rouse clusters often begin by relating the viscosity to the longest relaxation time of the cluster. The scaling of this relaxation time is then related to the exponents governing the geometrical properties of clusters. In the first paper to relate the viscosity to static exponents [67], de Gennes suggested the scaling relation for Rouse dynamics $s = 2\nu - \beta$. This result has been re-derived in other ways [70], and extended to produce scaling relations for other dynamic exponents, such as $u = d\nu/(d\nu + s)$. The numerical values of these exponents are given in given in tables 7.3 and 7.4.

It has been suggested [71] that the above scaling arguments fail because the internal structure of clusters is governed by another exponent, independent of the usual percolation exponents. This then changes the relaxation spectrum [72], and thus the viscosity.

### Exact Calculation

In a recent series of papers Broderix, Löwe, Müller, and Zippelius [73, 71, 74, 75, 76] have calculated the critical exponents of a model in which the dynamics of monomers are given by the Rouse model. In this calculation, the divergence of the viscosity is related to another exponent describing the behaviour of a resistor network, the crossover exponent $\phi$. This exponent governs the scaling of the resistance between two points on the incipient spanning cluster a distance $r$ apart, with $R \sim r^{\phi/\nu}$. Their calculation produces the scaling law $s = \phi - \beta$. In this work, the calculation of the viscosity begins with an exact mapping onto a network of resistors, here seen to be valid for Rouse dynamics only. The same group has calculated the divergence of the first normal stress coefficient $\Psi_1 \sim (p_c - p)^{-\ell}$. In [71], they derive a scaling relation, $\ell = s\frac{2-u}{1-u}$, and use numerical data for $u$ to find $\ell \approx 4.9$. In [76], a relation between the dynamics of Rouse clusters and diffusion on percolation clusters is used to derive two more scaling relations. These results fix the values of all of the dynamical exponents.

| | $s$ | $t$ | $u$ | $z$ | $\ell$ |
|---|---|---|---|---|---|
| Electrical analogy | 0.67 | 2.0 | | | |
| Scaling Rouse | 1.35 | 0.66 | | | |
| Rouse | 0.71 | | 0.79 | 3.3 | 4.1 |

Table 7.3: Numerical values of theoretical predictions for the scaling exponents in three dimensions. The line labelled "scaling Rouse" is the prediction for the Rouse model using scaling arguments.

| | $s$ | $t$ | $u$ | $z$ | $\ell$ |
|---|---|---|---|---|---|
| Electrical analogy | 1.3 | 1.3 | | | |
| Scaling Rouse | 2.528 | | 0.513 | | |
| Rouse | 1.2 | | 0.7 | 3.8 | 5.0 |

Table 7.4: Numerical values of theoretical predictions for the scaling exponents in two dimensions.

# Chapter 8

# Simulation Techniques

In this chapter we will describe the standard molecular dynamics techniques which we have used in our simulations of a gel. We will briefly describe the derivation of a discrete integration scheme from an equation of motion, as well as the equations of motion used to create shear flow at constant temperature in a non-equilibrium simulation. In section 8.7 we will give the Green-Kubo formula which is used to calculate the viscosity from an equilibrium simulation.

## 8.1 Molecular Dynamics

In a molecular dynamics simulation, a collection of particles is tracked as it moves through phase space following their equations of motion. Given a set of positions and velocities corresponding to a trajectory through phase space, it is then possible to measure a number of collective properties of the system of particles. These properties are measured as a time average, as is done in an experiment. This differs both from most analytical statistical mechanics calculations and from a Monte Carlo simulation, in which a time average is replaced by an ensemble average. A molecular dynamics technique has an advantage over Monte Carlo in that it is possible to calculate properties that depend on the dynamics of the system, such as two-time correlation functions. The quantities of most interest here, the viscosity and normal stress coefficients of the materials studied, depend on the dynamics of the system. The

Green-Kubo expression (given below in section 8.7) for the viscosity in terms of the equilibrium fluctuations makes this clear, as it depends on the time-evolution of the system. The steady-state method of calculating the viscosity described in section 8.4 also requires that the physical dynamics be properly simulated.

The distinction mentioned between a molecular dynamics simulation and a Monte Carlo one is not as sharp as suggested here: most molecular dynamics simulations, including those done in this thesis, are averaged over a selection of initial conditions, and so an ensemble average is performed, while it is possible to extract information about dynamics from some kinds of Monte Carlo. In the first part of this thesis, the time-dependence of macroscopic properties are calculated in Monte Carlo simulations using microscopic dynamics, and the time-dependence of particular models is often of interest in Monte Carlo simulations. However, the molecular dynamics technique does give a very direct way of determining dynamical properties of a physical system, as the physical Newtonian dynamics are explicitly followed. This chapter will describe a few aspects of molecular dynamics important to this thesis. Much more detailed information is available in the many books on the subject, including [77], [78], and [79].

In the simplest kind of molecular dynamics, the configuration of a system of particles evolves through time following Newton's laws. The system then explores a constant energy surface in phase space; the hope is that the system explores enough of this surface so that measurements made are characteristic of the micro-canonical ensemble. This will be called "equilibrium molecular dynamics", to distinguish it from the non-equilibrium techniques discussed later. The state of the system is evolved forward in time by a discrete timestep many times. There are many different discretization techniques. A simple one, used in the simulations done in this thesis, is sometimes called "velocity Verlet". In this algorithm, the positions and velocities of all particles are advanced from time $t$ to time $t + \Delta t$ using

$$\mathbf{x}_i\left(t + \Delta t/2\right) = \mathbf{x}_i(t) + \mathbf{v}_i(t)\Delta t/2 \tag{8.1}$$

$$\mathbf{v}_i(t + \Delta t) = \mathbf{v}_i(t) + \mathbf{F}_i(\{\mathbf{x}(t + \Delta t/2)\})\Delta t/m_i \tag{8.2}$$

$$\mathbf{x}_i(t + \Delta t) = \mathbf{x}_i(t + \Delta t/2) + \mathbf{v}_i(t + \Delta t)\Delta t/2. \tag{8.3}$$

In the notation used here, $\mathbf{x}_i$ and $\mathbf{v}_i$ represent the position and velocity of particle $i$,

while $\{\mathbf{x}\}$ represents the set of the positions of all particles.

There are several advantages to the Verlet method. First, the force evaluation, which is the most expensive step in computer time, is done only once. Second, the positions and velocities are evaluated at the same time, at the beginning and end of the timestep. This makes it easier to calculate quantities which depend on both sets of microscopic variables, such as the stress or the total energy. For an average of the stress itself, this is not so important, as the kinetic and potential contributions are added and so average separately. For two-time stress-stress correlations, however, having the positions and velocities available at the same time is a useful feature. Third, this scheme is time-reversible, as are the underlying dynamical laws. In addition to the fact that this better represents the physical dynamics, this makes it possible to run the simulation backward, so as to check the that the calculation has been done correctly. Fourth, this scheme is symplectic. The symplectic group is a symmetry of the Hamiltonian dynamics we wish to simulate, and maintaining this symmetry is associated with several desirable features. This will be discussed further below. Fifth, it preserves areas in phase space. If an ensemble of systems are started from a volume of phase space, say a constant energy surface, then the volume of phase space occupied by the ensemble at a later time will be the same as at $t = 0$. These last three features are believed to improve energy conservation properties [80].

The evolution of the coordinates and momenta in a Hamiltonian may be regarded as a linear map. The Jacobi matrices of the map over a single timestep are members of a group, called the symplectic group. This fact is related to conservation laws restricting the possible evolution of volumes in phase space. Using an integrator which respects this conservation should produce more accurate results.

While any numerical scheme will exhibit energy fluctuations, it is important that there be no systematic drift in the energy. If the integration scheme is time-reversible, then it seems likely that there will be no drift in energy. If the integrator is not area preserving and, therefore, not time-reversible, then the set of systems in a constant energy surface in phase space will evolve into a different, usually larger, volume. The energy thus cannot be conserved. Time reversibility is also important for overall energy conservation in another way: if an integration scheme is time reversible, it

cannot exhibit a steady drift of the energy over a period of the Hamiltonian simulated. However, the integration time of a typical molecular dynamics simulation is much shorter than the Poincaré time, the recurrence time of the dynamical system, and so a time reversible algorithm could exhibit drift over the course of a simulation.

The more stringent requirement that the integrator be symplectic does constrain the deviation of the energy from a constant, constraining both the noise and the drift in energy. This applies only to errors due to discretization; any errors due to round-off may cause systematic problems.

The lack of energy drift in a symplectic time-reversible algorithm is attributed to the fact that the equations of motion in a symplectic integration scheme can be derived from a Hamiltonian. This Hamiltonian differs from the one which we wish to study by terms which depend on the timestep to some power. Since the symplectic integration scheme conserves a Hamiltonian, which differs from the desired one by a constant, the energy, given by the Hamiltonian we wish to study, is also (almost) conserved. There should be no systematic drift in the energy or other measured quantities, only small fluctuations due to truncation error. See Thijssen [80] for a longer discussion of this point.

The equations of motion for non-equilibrium molecular dynamics done here are not derived from a Hamiltonian, and so the integration scheme need not be symplectic. However, the method described in the next section for the construction of symplectic integration schemes can also be used to construct an integration scheme for a non-Hamiltonian system. This integration scheme will be time reversible and should be stable for large timesteps.

## 8.2 Liouville Operators

The fact that the Verlet algorithm is symplectic and therefore stable for large timesteps was discovered after it was constructed. There is now a systematic method of constructing symplectic algorithms. In this method, one begins by considering the time evolution of a function of the coordinates of the system under the desired dynamics. The state of a system of particles is conventionally denoted by $\mathbf{\Gamma}$, standing for the set

all microscopic variables describing the system. This always includes the positions and momenta of all particles, and may also include other variables, such as the strain of the simulation cell. Any function $f(\mathbf{\Gamma})$ of the microscopic variables depends on time implicitly, through the time dependence of the coordinates, so

$$\frac{\mathrm{d}f}{\mathrm{d}t} = \left(\frac{\partial \mathbf{p}}{\partial t}\frac{\partial}{\partial \mathbf{p}} + \frac{\partial \mathbf{x}}{\partial t}\frac{\partial}{\partial \mathbf{x}}\right) f \equiv i\mathbf{L}f. \tag{8.4}$$

This defines the Liouville operator $\mathbf{L}$. The time derivatives on the right hand side are given by the equations of motion of the system to be simulated. For the usual Newtonian mechanics, they are

$$\frac{\partial \mathbf{p}}{\partial t} = \dot{\mathbf{p}} = \mathbf{F}(\mathbf{x}(t)) \tag{8.5}$$

$$\frac{\partial \mathbf{x}}{\partial t} = \dot{\mathbf{x}} = \frac{\mathbf{p}(t)}{m}. \tag{8.6}$$

The formal solution to (8.4) is

$$f(\mathbf{\Gamma}(t)) = e^{i\mathbf{L}t} f(\mathbf{\Gamma}(0)). \tag{8.7}$$

In this solution, $U(t) \equiv e^{i\mathbf{L}t}$ acts as a classical propagator, in that it acts on any function $f$ to give the function at a later time. In a simulation, the propagator is used to evolve the system forward by a small timestep $\Delta t$ many times, giving

$$\mathbf{\Gamma}(t + \Delta t) = U(\Delta t)\mathbf{\Gamma}(t) \tag{8.8}$$

for each step from $t$ to $t + \Delta t$. This formal solution is not useful as written, as solving for the action of the propagator would be equivalent to solving for the motion of the entire system of particles. If this could be done exactly, then the state of the system could be calculated at any time from the initial condition. However, this can only be done for very simple systems. For systems of many particles, a standard technique is to replace the exact propagator by a product of operators whose action on the state point can be calculated but which differs from the desired propagator by terms which are of higher order in $\Delta t$.

However, (8.8) is a convenient starting place for an approximate solution. The first step in the derivation of an approximation scheme is to split the Liouville operator into two or more pieces, $\mathbf{L} = \mathbf{L}_1 + \mathbf{L}_2$. For example, take $i\mathbf{L}_1 = \frac{\partial \mathbf{p}}{\partial t}\frac{\partial}{\partial \mathbf{p}}$, and $i\mathbf{L}_2 = \frac{\partial \mathbf{x}}{\partial t}\frac{\partial}{\partial \mathbf{x}}$.

This then gives an approximate expression for the propagator

$$U(\Delta t) = e^{i\mathbf{L}\Delta t} \approx e^{i\mathbf{L}_2\Delta t/2} e^{i\mathbf{L}_1\Delta t} e^{i\mathbf{L}_2\Delta t/2}, \tag{8.9}$$

which follows from the Trotter identity given in [77]

$$e^{A+B} = \left(e^{A/2N} e^{B/N} e^{A/2N}\right)^N e^{O(1/N^2)} \tag{8.10}$$

for large $N$. To determine the result of the action of each term in the approximate propagator on $f$, each exponential factor may be Taylor expanded. The exponential factor containing $\mathbf{L}_2$ becomes

$$e^{i\mathbf{L}_2\Delta t} \approx 1 + i\mathbf{L}_2\Delta t + \frac{1}{2}(i\mathbf{L}_2\Delta t)^2 = 1 + \Delta t\dot{\mathbf{x}} \cdot \frac{\partial}{\partial \mathbf{x}} + \dots \ . \tag{8.11}$$

Acting on $f(\mathbf{x}, \mathbf{p})$,

$$e^{i\mathbf{L}_2\Delta t} f(\mathbf{x}, \mathbf{p}) \approx f(\mathbf{x}, \mathbf{p}) + \Delta t\dot{\mathbf{x}} \cdot \frac{\partial}{\partial \mathbf{x}} f(\mathbf{x}, \mathbf{p}) + \dots \ . \tag{8.12}$$

But this is just the Taylor expansion of $f(\mathbf{x} + \Delta t\dot{\mathbf{x}}, \mathbf{p})$, and so

$$e^{i\mathbf{L}_2\Delta t} f(\mathbf{x}, \mathbf{p}) = f(\mathbf{x} + \Delta t\dot{\mathbf{x}}, \mathbf{p}). \tag{8.13}$$

The other exponential factor, $\exp(i\mathbf{L}_1\Delta t)$ with $i\mathbf{L}_2 = \dot{\mathbf{p}} \cdot \frac{\partial}{\partial \mathbf{p}}$, acts similarly, and so

$$e^{i\mathbf{L}_1\Delta t} e^{i\mathbf{L}_2\Delta t/2} f(\mathbf{x}, \mathbf{p}) = f(\mathbf{x} + \dot{\mathbf{x}}\Delta t/2, \mathbf{p} + \dot{\mathbf{p}}\Delta t). \tag{8.14}$$

Since the factor $\exp(i\mathbf{L}_2\Delta t/2)$ is furthest to the right and thus acts on $f$ first, the forces in $\dot{\mathbf{p}}$ are evaluated at the positions of the particles at $t + \Delta t/2$. Finally the last factor of $\exp(i\mathbf{L}_2\Delta t/2)$ acts on the result of applying the previous two operators. The action of these three operators can be represented by the evolution of the coordinates of the system as

$$\mathbf{x}_i\,(t + \Delta t/2) = \mathbf{x}_i(t) + \mathbf{p}_i(t)\Delta t/2m_i \tag{8.15}$$

$$\mathbf{p}_i(t + \Delta t) = \mathbf{p}_i(t) + \mathbf{F}(\{\mathbf{x}(t + \Delta t/2)\})\Delta t \tag{8.16}$$

$$\mathbf{x}_i(t + \Delta t) = \mathbf{x}_i(t + \Delta t/2) + \mathbf{p}_i(t + \Delta t)\Delta t/2m_i. \tag{8.17}$$

This is the "velocity Verlet" algorithm. Splitting the Liouville operator in other ways will result in other algorithms, with similar stability properties. All of the Verlet-equivalent algorithms may be derived in this way. This method of splitting the Liouville operator has also been used to derive new kinds of algorithms. Berne, Tuckerman, and Martyna [81] have used this method to derive multiple-timestep algorithms in which the effects of a slowly varying force are calculated infrequently, while those of a quickly varying force are calculated more often.

## 8.3 Constant Temperature

In an equilibrium simulation, the temperature of the system can be defined by the equipartition theorem, as $\langle mv^2/2 \rangle = dk_B T/2$, for each particle in $d$ spatial dimensions. The average total kinetic energy is thus proportional to the temperature. In a non-equilibrium situation the temperature is not defined. Even close to equilibrium, where it may be a reasonable approximation to consider a local effective temperature, equipartition no longer holds, and there is no general expression for the temperature. However, the kinetic energy can be used as an empirical measure of the temperature. In a flowing fluid, the kinetic temperature calculated using the peculiar velocity (the velocity measured with respect to the local flow velocity) is the temperature that would be measured by a thermometer moving with the local flow velocity. There are other methods of defining the temperature of a non-equilibrium system, which require more simulational effort. For example, a small equilibrium system may be attached to the system of interest and energy allowed to flow back and forth between the two systems. In the simulations done here, the simple kinetic temperature was used.

There are several techniques used to simulate a system at constant temperature. There are stochastic methods, in which a random force is added to the equations of motion. This then simulates the motion of a particle in a bath of smaller particles, which give it random kicks. The size of the random force may be chosen so as to produce a constant average temperature. There are also extended system methods, in which one or more additional degrees of freedom are simulated. These additional degrees of freedom are intended to describe the dynamics of a heat bath attached to

the system. A constant temperature may also be maintained by a Lagrange multiplier, constraining the kinetic energy. Both of the last two techniques were used in these simulations.

The Nosé-Hoover thermostat is an extended-system method. Unlike the constraint method, a Nosé-Hoover thermostat drives the system toward a specified temperature but allows fluctuations in the kinetic energy about the desired average temperature. It was used in these simulations during the equilibration phase. Since the particles were all initially positioned on a lattice, it was necessary to run for a reasonably large number of timesteps to reach a more representative configuration.

The Nosé-Hoover thermostat is based on a Hamiltonian introduced by Nosé [82], in which the many particles simulated are coupled to an additional degree of freedom $s$. This single degree of freedom is intended to represent an external heat bath coupled to the system. Later extensions of this method added additional degrees of freedom to better represent the heat bath [77]. This was not done here, as the Nosé-Hoover thermostat was used only in an early equilibration phase of the simulation, and the single degree of freedom method was sufficient to drive the system to the desired temperature. Hoover [83] rewrote the equations of motion derived from Nosé's Hamiltonian as

$$\frac{\mathrm{d}\mathbf{x}_i}{\mathrm{d}t} = \frac{\mathbf{p}_i}{m_i} \tag{8.18}$$

$$\frac{\mathrm{d}\mathbf{p}_i}{\mathrm{d}t} = \mathbf{F}_i - \zeta \mathbf{p}_i \tag{8.19}$$

$$\frac{\mathrm{d}s}{\mathrm{d}t} = \zeta s \tag{8.20}$$

$$\frac{\mathrm{d}\zeta}{\mathrm{d}t} = \frac{1}{\tau^2}\left(\frac{K(\{\mathbf{p}\})}{K_0} - 1\right). \tag{8.21}$$

Here, $\zeta$ is related to the "momentum" associated with the heat bath and $\tau$ is a relaxation time of the heat bath. $K(\{\mathbf{p}\}) = \sum_i p_i^2/2m$ is the instantaneous kinetic energy, and $K_0 = dNk_BT/2$ in $d$ dimensions is the kinetic energy corresponding to to the desired temperature $T$. The evolution of $s$ itself may be ignored, as it does not influence the motion of the rest of the system. Since the Nosé-Hoover thermostat may be derived from a Hamiltonian, a version of Liouville's theorem determines the

time evolution of the density in phase space, $\rho(\{\mathbf{x}\}, \{\mathbf{p}\}, \zeta)$.

Since the initial condition for each simulation run was generated as a state chosen by evolving forward in time using the Nosé-Hoover thermostat, these initial conditions should then be distributed according to the canonical constant temperature ensemble.

The kinetic temperature was maintained at a constant value during the measurement phase of the simulation using a method called a "Gaussian isokinetic thermostat." The equations of motion for this thermostat are

$$\frac{\mathrm{d}\mathbf{x}_i}{\mathrm{d}t} = \frac{\mathbf{p}_i}{m_i} \tag{8.22}$$

$$\frac{\mathrm{d}\mathbf{p}_i}{\mathrm{d}t} = \mathbf{F}_i - \alpha_g \mathbf{p}_i. \tag{8.23}$$

Here $\alpha_g$ plays a role similar to that of a Lagrange multiplier. It is chosen to be

$$\alpha_g = \frac{1}{2mK(\{\mathbf{p}\})} \sum_{j=1}^{N} \mathbf{F}_j \cdot \mathbf{p}_j; \qquad K(\{\mathbf{p}\}) = \frac{1}{2m} \sum_{j=1}^{N} \mathbf{p}_j \cdot \mathbf{p}_j \tag{8.24}$$

to keep the kinetic energy constant. A little algebra shows that, with these definitions, the time derivative of the kinetic energy $K(\mathbf{p})$ is zero.

## 8.4 Homogeneous Shear Flow

The properties of a flowing fluid can be studied directly by a modified molecular dynamics technique known as non-equilibrium molecular dynamics. There are several methods of creating a shear flow gradient in a simulated fluid. The simplest uses the boundary condition to create a flow. In this technique, the usual Newtonian equations of motion are used, but the boundary condition is modified. The neighbouring cells of the simulation cell in the $y$ direction are thought of as moving relative to the cell. To create a velocity gradient $\dot{\gamma}$ in a cell of size $L$, the cell above must move at a velocity $v_{\mathrm{box}} = \dot{\gamma}L/2$, and that below at $-v_{\mathrm{box}}$. This has two effects. First, the calculation of the forces on a particle is modified. The neighbouring particles of any particle are given not by the usual minimum image convention, but by those particles whose shifted positions are within an interaction distance of the particles. Second,

the motion of particles across a boundary must be handled correctly. When a particle crosses a boundary parallel to the $y$ direction, it is replaced in the simulation box in a position corresponding to its shifted position in the $x$ direction. The $x$ component of the particle velocity must also be changed as it crosses a boundary. If a particle crosses the boundary in the upward direction, it is replaced in the bottom of the simulation cell. It should then be thought of as coming from the cell below the current one and so must have the relative velocity of the upper and lower boundaries, $2v_{\text{box}}$, subtracted. These boundary conditions are known as Lees-Edwards boundary conditions [84].

A steady flow may also be generated by another technique, in which a homogeneous deformation is applied to the system[1]. In this method, the equations of motion are changed to generate a velocity gradient. The new equations of motion are

$$\dot{\mathbf{x}} = \mathbf{p}/m + \hat{\mathbf{i}}\dot{\gamma}x_y \tag{8.25}$$

$$\dot{\mathbf{p}} = \mathbf{F} - \hat{\mathbf{i}}\dot{\gamma}p_y \tag{8.26}$$

$$\frac{\mathrm{d}\gamma_{xy}}{\mathrm{d}t} = \dot{\gamma}. \tag{8.27}$$

Here $\gamma$ is the tensor giving the strain of a unit cube of material. Only the off-diagonal elements $\gamma_{xy}$ and $\gamma_{yx}$ are time dependent.

By eliminating the velocity from the homogeneous shear flow equations of motion, we can see that the second order differential equation governing the evolution of the position is

$$\frac{\mathrm{d}^2\mathbf{x}}{\mathrm{d}t^2} = \frac{\mathbf{F}}{m} + \hat{\mathbf{i}}\frac{\mathrm{d}\dot{\gamma}}{\mathrm{d}t}. \tag{8.28}$$

If the shear rate is a step function, 0 for $t < 0$ and a constant for $t > 0$, then integration of (8.28) over an infinitesimal interval around $t = 0$ sets up an initial velocity gradient; the usual Newtonian equations of motion are then obeyed for $t > 0$. This is identical to the Lees-Edwards method of generating shear flow, so the evolution of the system is the same as it would be with boundary driven flow for steady flow. For non-steady flow, the effect of the boundary is much smaller when the homogeneous deformation technique is used. Another advantage of the homogeneous deformation method, in

[1]This technique is also known as the SLLOD technique, but this expression is so ugly it will not appear elsewhere in this thesis.

both steady and non-steady flow, is that it makes it possible to store the "peculiar velocity," the velocity relative to the local average flow rate, which appears in the equations of motion. For steady shear flow, if the bottom of the simulation cell is thought of as being at $y = 0$ and moving at zero velocity, the peculiar velocity of a particle is given by $(u_x, u_y, u_z) = (v_x - \dot{\gamma}y, v_y, v_z)$. In the simulations done here, the peculiar velocity was stored. This had several advantages. First, there was no need to change the velocity as a particle crossed the $y$ boundary of the system. Second, all quantities which were measured depended on the peculiar velocity rather than the velocity. This included the temperature and the stress tensor. These could then be calculated directly from the peculiar velocity as stored. The homogeneous deformation method should also be useful for more general time-dependent flow, where $\dot{\gamma}$ is time-dependent.

The equations of motion (8.25)–(8.27) are not derived from a Hamiltonian. A set of equations of motion for homogeneous shear flow which are derived from a Hamiltonian does exist. However, these equations do not generate the correct non-linear response, while it is believed that equations (8.25)–(8.27) do, as suggested by [85]. In this paper, it is assumed that if fluid under shear flow may be described by starting with an initial distribution of positions and velocities given by the canonical distribution function for $t < 0$, and then at $t = 0$ transforming the $x$ velocity of each particle to $\dot{x} \rightarrow \dot{x} + \dot{\gamma}y$. It is then shown that the same distribution as produced by this method is given by the homogeneous deformation technique given here. The non-linear effects differ when different algorithms are used, so the Hamiltonian approach must be incorrect. Since we are interested in a non-linear effect, the normal stress difference in a complex fluid under shear flow, it is important to use a method which does correctly reproduce non-linear properties.

In any of these methods of simulating shear flow, the simulation cell heats up as energy added due to the driving force is dissipated. With the aid of a theory for the increase in entropy in shear flow, this may be used to calculate the viscosity of the fluid. However, it is more straightforward, and less theory-dependent, to remove this heat and maintain a constant temperature. In an experiment, the heat is removed at the boundary of the system, where it is in contact with a reservoir, and this may be

done in a simulation. The heat is more commonly removed from the entire system, using the modified equations of motion described in section 8.3.

## 8.5 Shear Flow at Constant Temperature

Putting together the shear flow equations of motion (8.25)–(8.27) with the Gaussian isokinetic constraint (8.22)–(8.23), the equations of motion for a constant kinetic energy simulation of shear flow are

$$\frac{\mathrm{d}\mathbf{x}_i}{\mathrm{d}t} = \frac{\mathbf{p}_i}{m_i} + \hat{\mathbf{i}}\dot{\gamma}x_{yi} \tag{8.29}$$

$$\frac{\mathrm{d}\mathbf{p}_i}{\mathrm{d}t} = \mathbf{F}_i + \hat{\mathbf{i}}\dot{\gamma}p_{yi} - \alpha_g\mathbf{p}_i \tag{8.30}$$

$$\frac{\mathrm{d}\epsilon_x}{\mathrm{d}t} = \dot{\gamma}. \tag{8.31}$$

The Gaussian multiplier must also be modified, to

$$\alpha_g = \frac{1}{2mK(\{\mathbf{p}\})}\sum_{j=1}^{N}(\mathbf{F}_j\cdot\mathbf{p}_j - \dot{\gamma}p_{xj}p_{yj}); \tag{8.32}$$

$K(\{\mathbf{p}\})$ is the same as in (8.24).

## 8.6 Integration Scheme for Shear Flow at Constant Temperature

The Liouville operator technique discussed in section 8.2 can be used to derive a discrete integration scheme for constant temperature shear flow. The algorithm used in the simulations discussed in this thesis was derived in [86]. The set of microscopic variables $\Gamma$ includes the strain $\epsilon$ of the simulation cell as well as the set of positions and momenta of all particles. Only the $\hat{\mathbf{x}}$ component of the strain need be updated for the planar shear flow, and so other components will be suppressed. The Liouville operator for the equations of motion (8.29)–(8.31) is then given by

$$i\mathbf{L} = (\mathbf{p} + \hat{\mathbf{i}}\dot{\gamma}x_y, \mathbf{F} - \hat{\mathbf{i}}\dot{\gamma}p_y - \alpha_g\mathbf{p}, \dot{\gamma})\cdot\left(\frac{\partial}{\partial\mathbf{x}}, \frac{\partial}{\partial\mathbf{p}}, \frac{\partial}{\partial\epsilon_x}\right). \tag{8.33}$$

To derive an approximate discrete integration scheme, this Liouville operator is split into two parts,

$$i\mathbf{L}_1 = (\mathbf{0}, \mathbf{F} - \hat{\mathbf{i}}\dot{\gamma}p_y - \alpha_g\mathbf{p}, 0) \cdot \left(\frac{\partial}{\partial\mathbf{x}}, \frac{\partial}{\partial\mathbf{p}}, \frac{\partial}{\partial\epsilon_x}\right) \tag{8.34}$$

and

$$i\mathbf{L}_2 = (\mathbf{p} + \hat{\mathbf{i}}\dot{\gamma}x_y, \mathbf{0}, \dot{\gamma}) \cdot \left(\frac{\partial}{\partial\mathbf{x}}, \frac{\partial}{\partial\mathbf{p}}, \frac{\partial}{\partial\epsilon_x}\right). \tag{8.35}$$

The same approximate Trotter formula as in section 8.2 can be used with this split Liouville operator. The integration scheme associated with this operator is given by

$$\mathbf{x}(\Delta t/2) = \mathbf{x}(0) + \Delta t\mathbf{p}(0)/2m + \hat{\mathbf{i}}[\Delta t\dot{\gamma}x_y(0)/2 + (\Delta t/2)^2\dot{\gamma}p_y(0)/2m] \tag{8.36}$$

$$\epsilon_x(\Delta t/2) = \epsilon_x(0) + \dot{\gamma}\Delta t/2 \tag{8.37}$$

$$\mathbf{p}(\Delta t) = \mathbf{p}(0) + \Delta t\mathbf{F}(\{\mathbf{x}(\Delta t/2)\}) - \alpha_g\Delta t\frac{\mathbf{p}(\Delta t) - \mathbf{p}(\Delta t)}{2} - \hat{\mathbf{i}}\dot{\gamma}\Delta t\frac{p_y(\Delta t) + p_y(\Delta t)}{2} \tag{8.38}$$

$$\mathbf{x}(\Delta t) = \mathbf{x}(\Delta t/2) + \Delta t\mathbf{p}(\Delta t)/2m + \hat{\mathbf{i}}[\dot{\gamma}x_y(\Delta t/2) + (\Delta t/2)^2\dot{\gamma}p_y(t)/2m] \tag{8.39}$$

$$\epsilon_x(\Delta t) = \epsilon_x(\Delta t/2) + \dot{\gamma}\Delta t/2. \tag{8.40}$$

In (8.38), $\alpha_g$ is given by

$$\alpha_g = \frac{\sum_i[\mathbf{F}_i \cdot (\mathbf{p}_i(\Delta t) + \mathbf{p}_i(0))/2 - \dot{\gamma}(p_{xi}(\Delta t) + p_{xi}(0))(p_{yi}(\Delta t) + p_{yi}(0))/4]}{\sum_i(\mathbf{p}_i(\Delta t) + \mathbf{p}_i(0)) \cdot (\mathbf{p}_i(\Delta t) + \mathbf{p}_i(0))/4}. \tag{8.41}$$

Agreement between (8.38) and (8.41) is obtained by iteration. The discrete equations of motion in (8.36)–(8.40) contain all terms up to order $(\Delta t)^2$, and an iterative scheme need only be correct to this order. We have already neglected terms of higher order, so neglecting them in the iterative solution does not cause any additional error.

This combination of techniques is somewhat unphysical. The heat generated by the shear flow is removed homogeneously, throughout the entire sample. This differs from experiments, in which the heat generated is removed at the boundary. Some simulations [87], using both this method of removing heat and attaching the sample to a heat bath at the boundary, seem to indicate that the results are the same, at least for the small shear rates studied here.

## 8.7 Green-Kubo Formula for the Viscosity

Transport coefficients in the small perturbation regime can often be calculated from the fluctuations in a equilibrium system. This regime is the regime of linear response, in which the response of the system is proportional to the external force driving it. Beyond this regime, the non-equilibrium methods discussed in the rest of this chapter must be used to calculate transport coefficients.

The viscosity in the linear response regime may be calculated from the equilibrium stress-stress correlation function, which measures the correlations between spontaneous fluctuations in the stress $\sigma$ in an equilibrium system. The Green-Kubo expression for the viscosity is

$$\eta = \frac{V}{k_B T} \int_0^\infty \mathrm{d}t \langle \sigma_{xy}(0) \sigma_{xy}(t) \rangle. \tag{8.42}$$

This relation is derived in many books on simulation and on statistical mechanics; see for example [77]. Since the positions and velocities of all particles are calculated in a molecular dynamics simulation, the stress may be calculated as

$$\sigma_{xy} = \frac{1}{V} \left( \sum_i m r_i^x r_i^y + \sum_{i<j} r_{ij}^x F_{ij}^y \right). \tag{8.43}$$

## 8.8 Units

In simulations, it is useful to express all quantities in terms of a system of reduced units, so that most quantities of interest are of order one. The standard set of basic units to use is the unit of length, $\sigma$, the unit of energy, $\epsilon$, and a unit of mass, $m$. These can all be set to one during the simulation, and then any result may be converted back to physical units after the simulation. For example, the unit of temperature is $\epsilon/k_B$. The unit of time has a somewhat special role, as it determines the length of physical time corresponding to the simulation time. Effects which are only noticeable at larger times will not be seen in the simulation. The unit of time is given by $\sigma\sqrt{m/\epsilon}$. If the particles simulated represent single atoms, for example of argon, one unit of simulation time corresponds to about $2 \times 10^{-12}$ seconds. (Numerical values from [77].)

In the case of the steady-state shear simulations presented in chapter 9, the fact that the simulation time corresponds to a large physical time is particularly serious in terms of its effects on comparison with experiment. For a simple fluid, the shear rate must be of order one to produce an observable effect in the simulation, and so the shear rate will be of order $10^{12}$, much higher than is possible in experiments. The non-linear effects seen in simulations cannot be seen experimentally. For polymer solutions and melts, the situation is not so serious, and some of the non-linear effects have been seen.

All other quantities are given in terms of these reduced units. For example, a dimensionless viscosity $\eta$ is given by multiplying the dimensionful quantity $\tilde{\eta}$ by $\sqrt{\epsilon m}/\sigma^2$. All quantities plotted in the next chapter have been made dimensionless in this way.

# Chapter 9

# Molecular Dynamics Simulation Results

In this chapter we present the results of our simulations of a model viscous fluid. After discussing the model simulated, we will show simulation results indicating that the shear viscosity and normal stress differences diverge at the percolation point in both two and three dimensions. We will then conclude with some comments on the relation of this work to experiments and to other calculations, and on possible future simulations.

## 9.1 Model

The model studied in this thesis includes both random bonds and excluded volume interactions between particles. To begin the simulation, all particles are placed on a lattice. Each particle is crosslinked to its neighbours with a probability $p$, with each bond created independently. The structure of the clusters created is thus described by percolation theory, as discussed in chapter 7, and the critical point is given by the bond percolation probability for the lattice. The potential joining bonded particles is given by a harmonic potential around a finite (non-zero) rest length $r_0$, so that

$$V_{\rm cl} = \frac{1}{2}k(r_{ij} - r_0)^2 \tag{9.1}$$

between any pair of bonded particles $i$ and $j$.

The excluded volume interaction is given by a pair potential between every pair of particles, with

$$V_{\rm ev}(r_{ij}) = \epsilon\frac{\sigma}{r^{36}}. \tag{9.2}$$

This potential is cut off at $r_{ij} = 1.5\sigma$. To avoid a discontinuity in either the potential or the force, a smoothing polynomial is used to take the potential to zero by $r_{ij} = 1.51$. This polynomial is in even powers of $r_{ij}$ up to $r_{ij}^4$, and is chosen so that both the potential and the force are continuous everywhere and vanish at $r_{ij} = 1.51$. The length scale $\sigma$ is chosen to be $\sigma = 1$, which simply sets the length scale of the potential. The energy scale is chosen so that $\epsilon = 1$, and the temperature is given by $k_BT/\epsilon = 1$. With the excluded volume interaction alone this model forms a simple liquid at low enough densities. All simulations discussed here are done at densities low enough so that the uncrosslinked fluid is well inside the fluid phase.

For $p = 0$, this model is a simple fluid with interactions close to a hard core fluid. As $p$ increases, clusters of different sizes of bonded particles are produced. The structure of these clusters is exactly that studied in percolation theory. The measurable properties of this model should thus be given by percolation theory results. If there is a universal divergence of the viscosity characteristic of percolation, then it should be possible to see this divergence in our simulations. The same divergence should appear in experiments if it is indeed a universal feature.

## 9.2 Results in Two Dimensions

We will first discuss the results of simulations of two dimensional systems, in which the shear viscosity is measured using both the non-equilibrium molecular dynamics technique described in the previous chapter and the Green-Kubo integral of the equilibrium stress-stress correlation function. These simulations are done beginning with particles on the sites of a triangular lattice, and bonds are added between nearest neighbours. The critical point is thus at the percolation point of two-dimensional bond percolation on a triangular lattice, $p_c = 2\sin(\pi/18) \approx 0.347296$ [51]. The fact

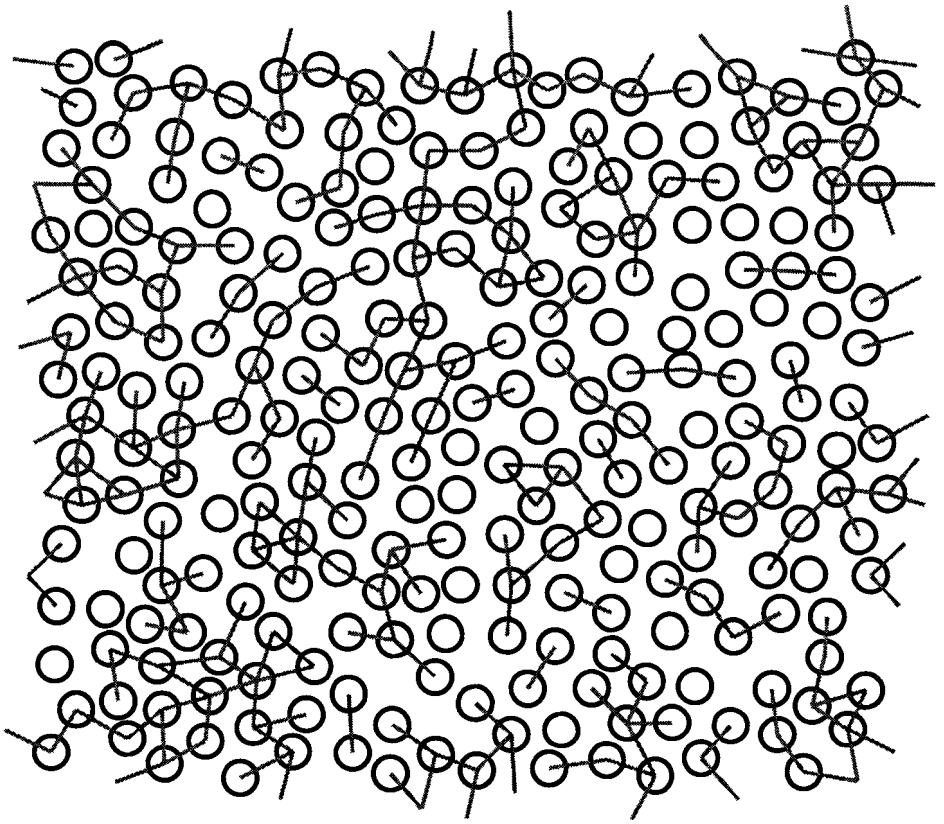

Figure 9.1: A sample configuration of the model in two dimensions after bonding and simulation for many timesteps. The circles represent the repulsive interaction between particles and the lines represent bonds between particles which began as neighbours on the lattice.

that the critical point is known to very high accuracy here makes the analysis much simpler than in experiments: since $p_c$ is known, there is one less parameter to be determined from the data. The lattice constant of the initial triangular lattice is 1.2, and so these simulations are done at a number density $n = N/V = \frac{1}{(1.2)^2 \sin(60)} \approx 0.8$. The rest length of the bond between linked particles is $r_0 = 1.2$, equal to the distance between sites on the triangular lattice. The spring constant of this bond is $k = 40\epsilon/\sigma^2$. All of the simulations of two dimensional systems presented here are done at a single system size, a box of size $L = 32$ particles on each side.

After an initial thermalization period, in which the temperature is set using the

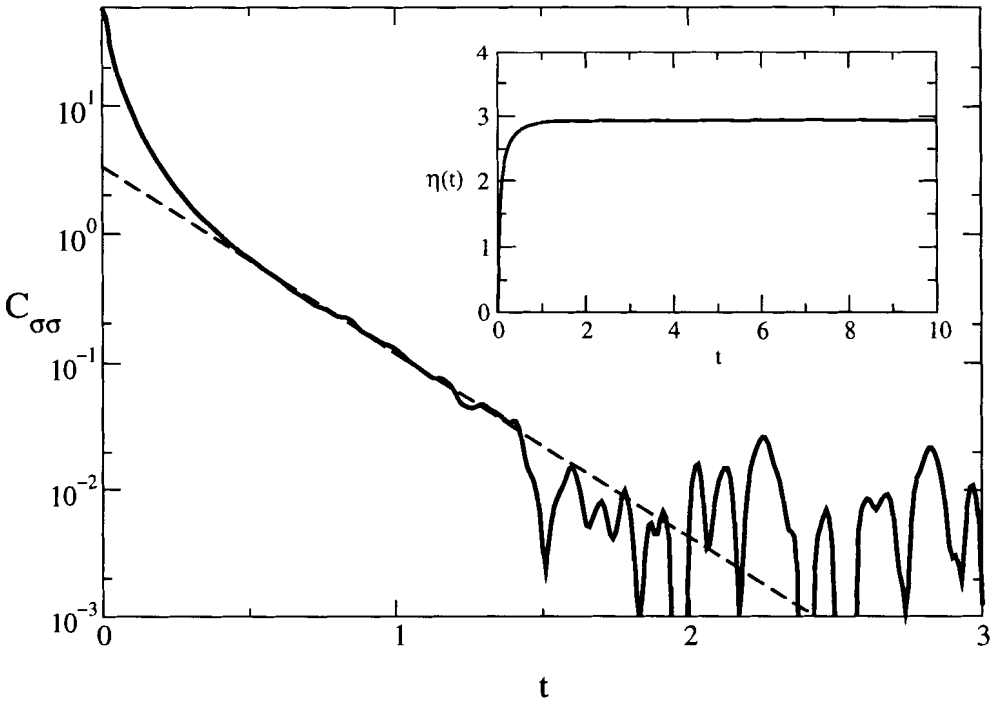


Figure 9.2: The stress-stress correlation function for a fluid with no bonds between particles ($p = 0$). The inset shows the result of the Green-Kubo integral of equation (8.42), with a cutoff at time $t$.

Nosé-Hoover technique, a constant shear flow is imposed on the system. Although the homogeneous shear flow method creates the desired flow profile instantaneously, in these simulations some relaxation time is required for measurable quantities to become stable. To remove the effects of the initial perturbation, between $10^5$ and $10^6$ timesteps were discarded before beginning to the measurement of the stress. After this initial period, the stress was averaged over between $10^5$ (low $p$) and $10^7$ (high $p$ and low $\dot{\gamma}$) timesteps. The stress is also averaged over many different bond realizations: as few as 10 for low $p$, and up to 200 for $p$ close to $p_c$.

Figure 9.2 shows the stress-stress correlation function for a simple fluid with no crosslinks between particles. Here, the correlation function decays as an exponential in time and the numerical integration produces an estimate of the viscosity quite rapidly.

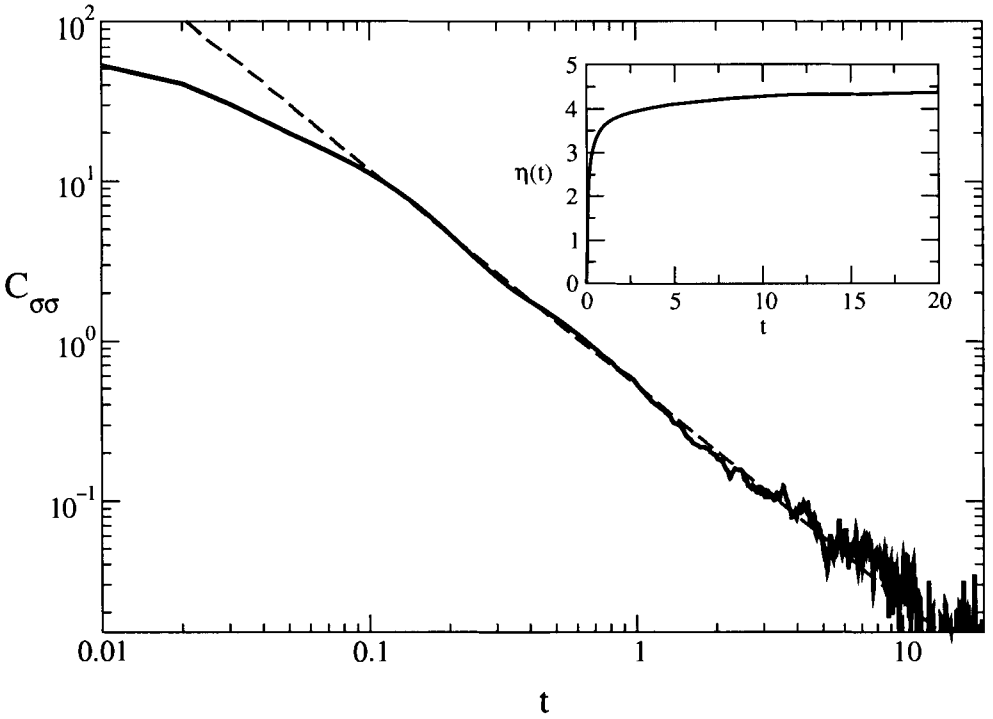


Figure 9.3: The stress-stress correlation function for a crosslinked fluid at $p = 0.1$. Here the relaxation is slower than exponential, and so a simple numerical integration does not converge before the noise of the stress-stress correlation function becomes larger than the signal, as shown in the inset. The straight line on the main figure is a power law fit.

The same stress-stress correlation function for a lightly-crosslinked fluid, with $p = 0.1$, is shown in figure 9.3. In this case, the decay of correlations is much slower. The slow relaxation of the correlation function means that a simple numerical integration does not capture the integral to infinity appearing in the Green-Kubo formula. In this case, the correlation function is fit to a power law, and the remaining integral is added to that determined directly from the data.

The results of non-equilibrium molecular dynamics simulations at $p = 0$ and at $p = 0.1$ are shown in figure 9.4. In these simulations a shear flow at a shear rate $\dot{\gamma}$ is imposed as described in the previous chapter. The stress required to produce this flow is then calculated from the expression giving the stress from the microscopic state

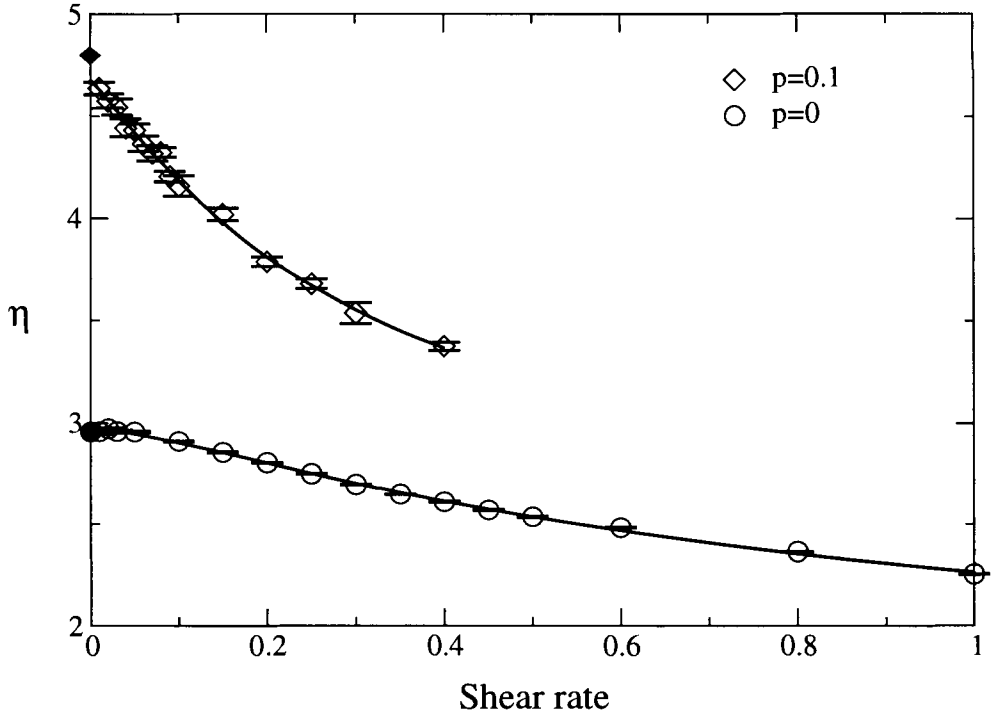


Figure 9.4: The shear viscosity determined in non-equilibrium molecular dynamics simulations as a function of the shear rate $\dot{\gamma}$. The points at $\dot{\gamma} = 0$ (filled symbols) are results from equilibrium simulations. The curves are fits to the Cross equation (6.23), with values of $m = 1.36$ for the $p = 0$ data and $m = 1.14$ for the $p = 0.1$ data.

of the system in equation(8.43). The viscosity at at the imposed shear rate is then calculated by dividing the stress by the shear rate. The results of the equilibrium simulations are also shown, and agree with the extrapolation of the non-equilibrium data to zero shear rate. The difference between the extrapolation of the finite shear rate data and the zero shear rate estimate of the viscosity is not significant, as different fits to the stress-stress correlation function produce values for $\eta$ that differ by about 5%.

The quantity of most interest in these simulations is the zero shear rate viscosity. This must be determined from the non-equilibrium simulation results by extrapolation to zero shear rate. For the $p = 0$ and $p = 0.1$ simulation results shown in figure 9.4, the extrapolation is easy, and any extrapolation procedure produces essentially the same

result. Shown in the figure is a fit to the phenomenological Cross equation discussed in section 6.4.1. Fits to a straight line over the low $\dot{\gamma}$ region or to a Lorentzian plus a constant produce zero shear rate values of the viscosity that differ by less than one percent. Fitting to a Lorentzian is suggested in [88] and has the advantage that the fitting function is symmetric in $\dot{\gamma}$ and is analytic near $\dot{\gamma} = 0$.

The extrapolation is not as easy for higher bond probabilities, as shown in figure 9.5. Here, the Cross equation does represent the data, but the extrapolation to $\dot{\gamma} = 0$ differs significantly from other extrapolations. The Lorentzian and linear fits, which do not represent the data over as large a range, do produce similar extrapolations to $\dot{\gamma} = 0$. For use in later figures, the Lorentzian fits have been used for the extrapolation, and the difference between different extrapolation techniques used to estimate the error.

For $p$ close to $p_c$, the Cross equation fitting function rises significantly beyond the range of the data. The form of the Cross equation allows this kind of behaviour as the exponent in the denominator may become less than one. There are several possible explanations of the failure of the Cross equation to provide both a fit to the data and a reasonable extrapolation. The first is simply statistical. If $\eta$ at the lowest $\dot{\gamma}$ point in a data set is in error and is too high, this will cause the fit to trend up for small values, so the extrapolation to $\dot{\gamma} = 0$ will be poor. Another possible explanation is that the data are not extended to small enough $\dot{\gamma}$. Evidence supporting this possibility comes from fitting data sets at lower $p$ and omitting the smallest $\dot{\gamma}$ values, which can show the same effect. Unfortunately, it is difficult to overcome either of these limitations on the data for this particular model without more computational resources. Another possibility is that there may be a real effect influencing the data. There may be another transition, different from the gel transition we wish to study, in which the functional form of $\eta$ as a function of $\dot{\gamma}$ changes quantitatively. An effect somewhat like this appears near a glass transition, as studied by molecular dynamics simulations, as shown in [89].

The viscosity as a function of $p$ is shown in figure 9.6. In the single system size simulated here, there is very little curvature visible above $p = 0$, which one might expect to differ from the rest of the data. The simple fluid with no bonds should not

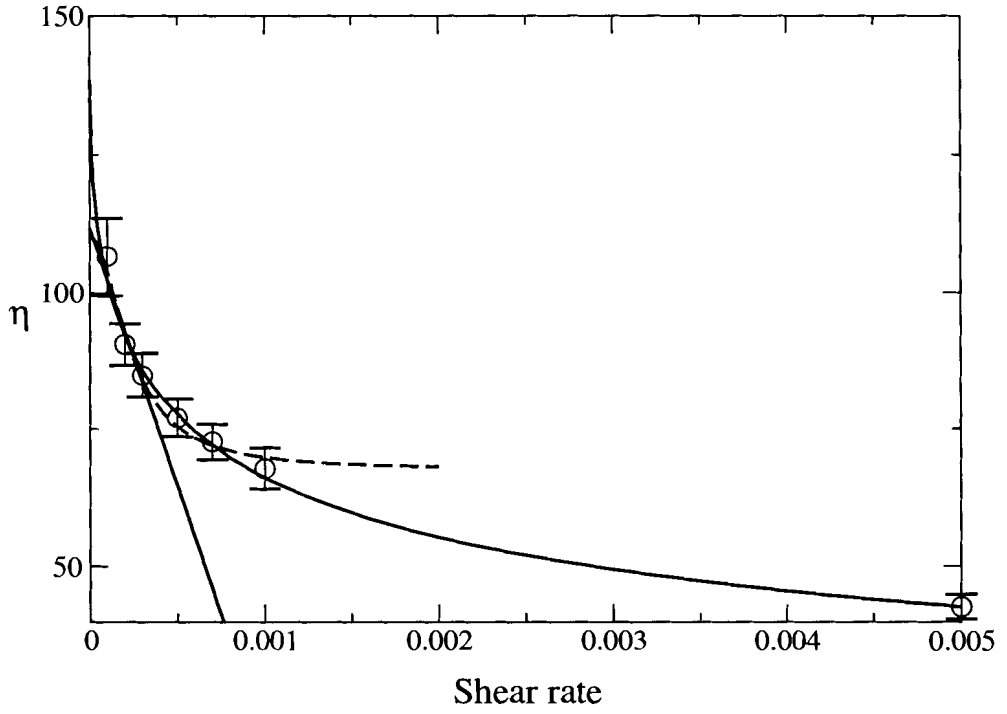


Figure 9.5: The shear viscosity determined in non-equilibrium molecular dynamics simulations as a function of the shear rate $\dot{\gamma}$, at a bond probability $p = 0.3$. Fits are shown to the Cross equation (6.23) (solid curve) and to a Lorentzian (dashed line) as is a linear fit. A value of $m = 0.51$ is used in the fit to the Cross equation.

know about the behaviour near the percolation transition.

### 9.2.1 Normal Stress Difference

Since the simulations done in two dimensions used a non-equilibrium technique, in which the sample is required to flow, a normal stress difference may be measured. In two dimensions there is only one normal stress difference. As discussed in section 6.4.1, the normal stress difference is expected to depend on the shear rate as $N_1 = \Psi_1 \dot{\gamma}^2$. The normal stress coefficient $\Psi_1$ is then a material parameter. An estimate of the normal stress coefficient at a shear rate $\dot{\gamma}$ can be determined by dividing the measured stress difference by $\dot{\gamma}^2$. The dependence of the measured coefficient $\Psi_1$ on the shear rate is shown in figure 9.7. Unfortunately, it does not seem possible to continue the

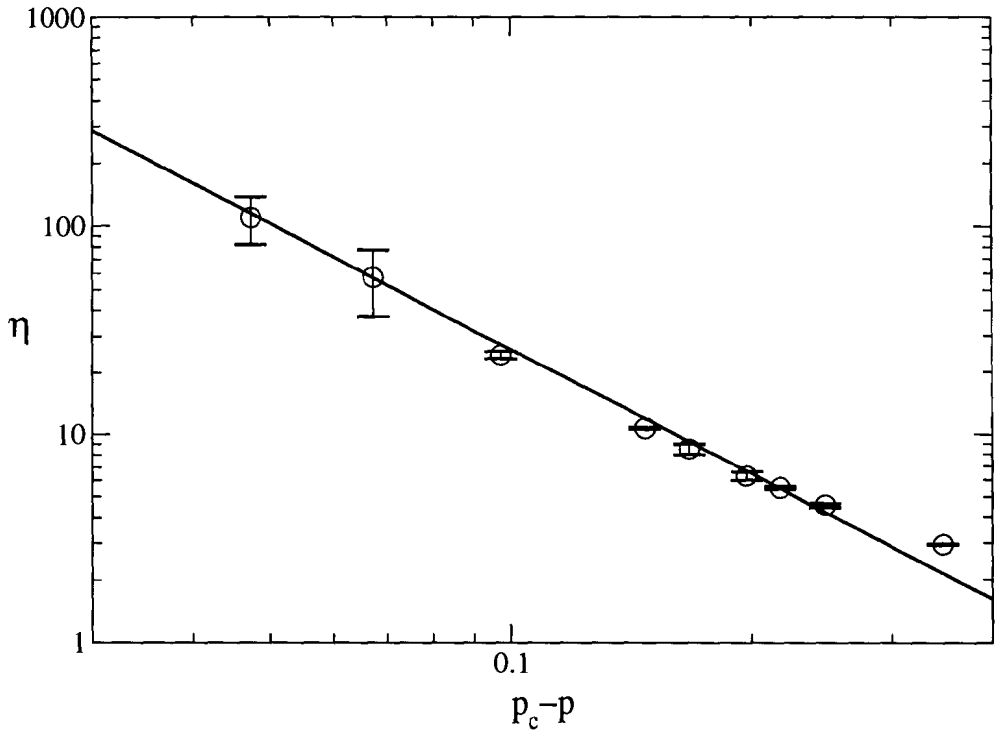


Figure 9.6: The viscosity as a function of $p$ for a crosslinked fluid in two dimensions. The line shows a power law, with exponent $s = 2$.

simulations to low enough $\dot{\gamma}$ for any bond probability to clearly see $\Psi_1$ cross over to an asymptotic value, as seen for the shear viscosity at low $p$.

The divergence of $\Psi_1$ near $p_c$ is shown in figure 9.8. The figure shows a power law behaviour of $\Psi_1$ over much of the range of $p$ simulated. The point at $p = 0$ (furthest to the right in the figure) deviates from this power law, as might be expected: the simple fluid with no bonds should not show the effects of the critical point at $p_c$. The exponent governing the divergence of $\Psi_1$ in two dimensions for this model is $\ell \approx 6$. This is an extremely steep divergence, and should be obvious in an experiment.

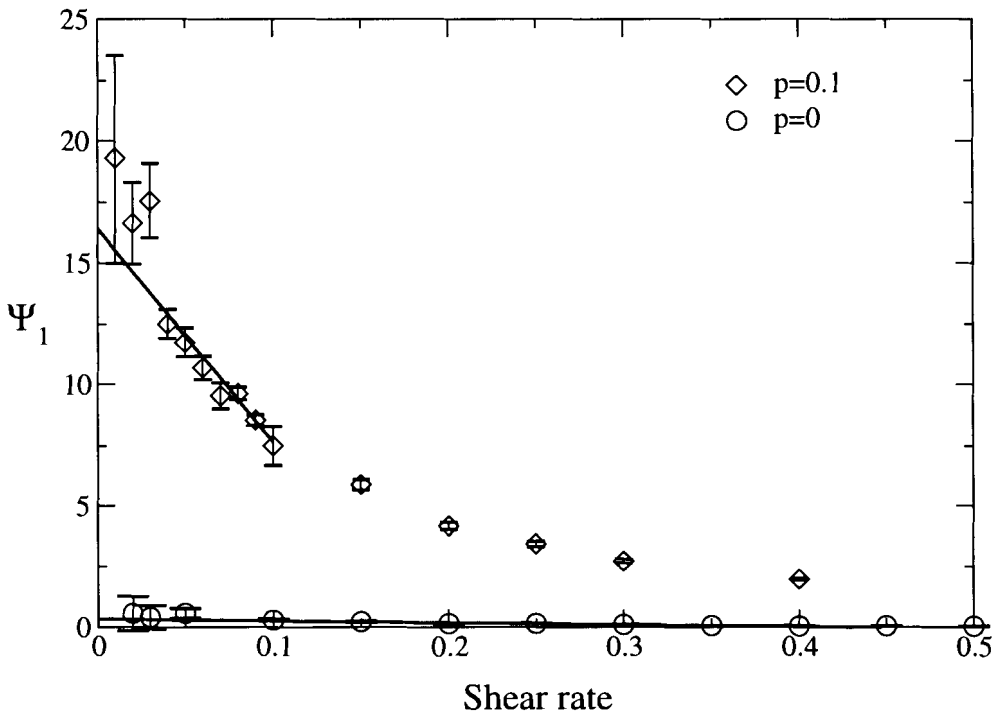


Figure 9.7: The normal stress coefficient $\Psi_1$ as a function of $\dot{\gamma}$ for $p = 0$ and $p = 0.1$.

## 9.3 Results in Three Dimensions

Additional simulations were done of three-dimensional systems, using the equilibrium Green-Kubo technique to calculate the shear viscosity. In these simulations, particles begin on a simple cubic lattice and bonds are added between nearest neighbours on this lattice. The critical point is thus at the critical point of three-dimensional bond percolation on a cubic lattice, so $p_c \approx 0.2488$. These simulations are done at a volume fraction $\Phi = \pi N\sigma^3/6V = 0.4$, or a number density $n = N/V \approx 0.7639$. The rest length of the bond between linked particles is $r_0 = 1.1$. This rest length is chosen so that at zero temperature the bonds are unstretched; it is the distance between the lattice sites on a cubic lattice at the density chosen. The spring constant of this bond is $k = 5\epsilon/\sigma^2$.

Since equilibrium simulations are done close to the percolation point in three

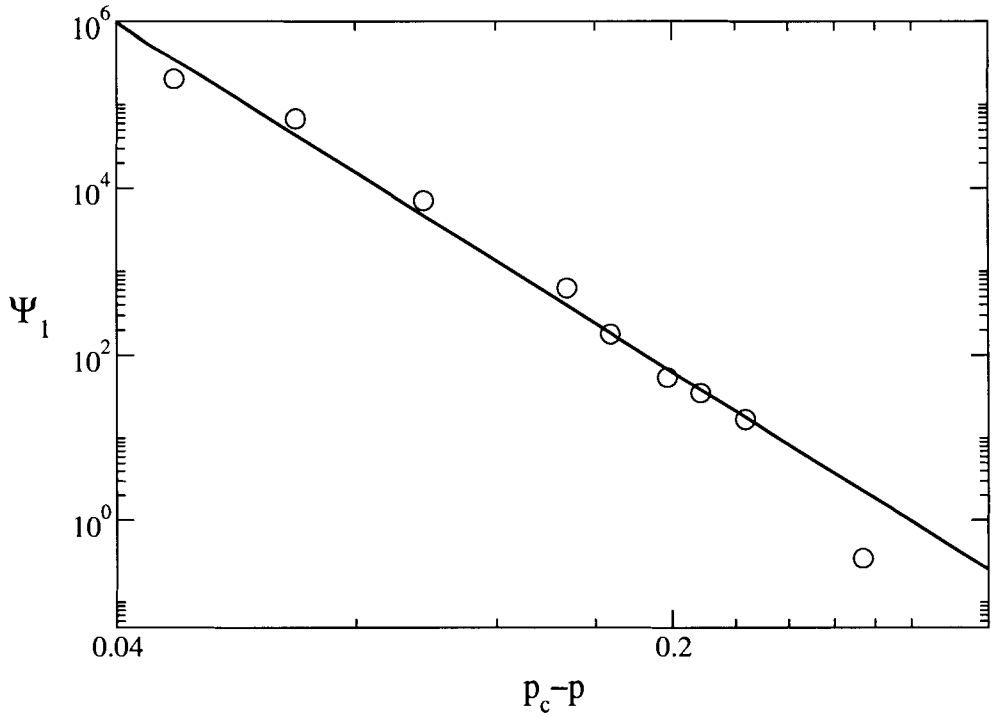


Figure 9.8: The normal stress coefficient $\Psi_1$ as a function of $p_c - p$ as measured in simulations in two dimensions. The line is a power law $\Psi_1 \sim (p_c - p)^{-\ell}$, with $\ell = 6$.

dimensions, the stress relaxation function $G(t)$ may be measured, and then the complex viscosity $\eta^*$ may be calculated. Figure 9.9 shows the real and imaginary parts of $\eta^* = \eta' + i\eta''$ for several values of $p$ close to $p_c$ as functions of the frequency $\omega$. The behaviour of $\eta^*$ is discussed in sections 6.3.3 and 7.5.1. For small $\omega$, the real and imaginary parts behave as $\eta' \sim$ const and $\eta'' \sim \omega$, as they should for a fluid. For larger frequencies, these functions both cross over to a power law $\eta' \sim \eta'' \sim \omega^{u-1}$. This is more evident for $\eta'$ than for $\eta''$, and the crossover to this power law moves to lower frequencies as $p \to p_c$. The line on the figure shows a power law with $u = 0.75$. The loss angle, given by $\tan\delta = \eta''/\eta'$, gives another estimate for $u$, as at high frequencies, $\delta$ should be given by $\delta = u\pi/2$ close to $p_c$. The data for $p = 0.24$ give $u = 0.74$.

As is the case for the two-dimensional simulations, the stress-stress correlation function decays quite slowly. Here, it has been fit with a stretched exponential (shown

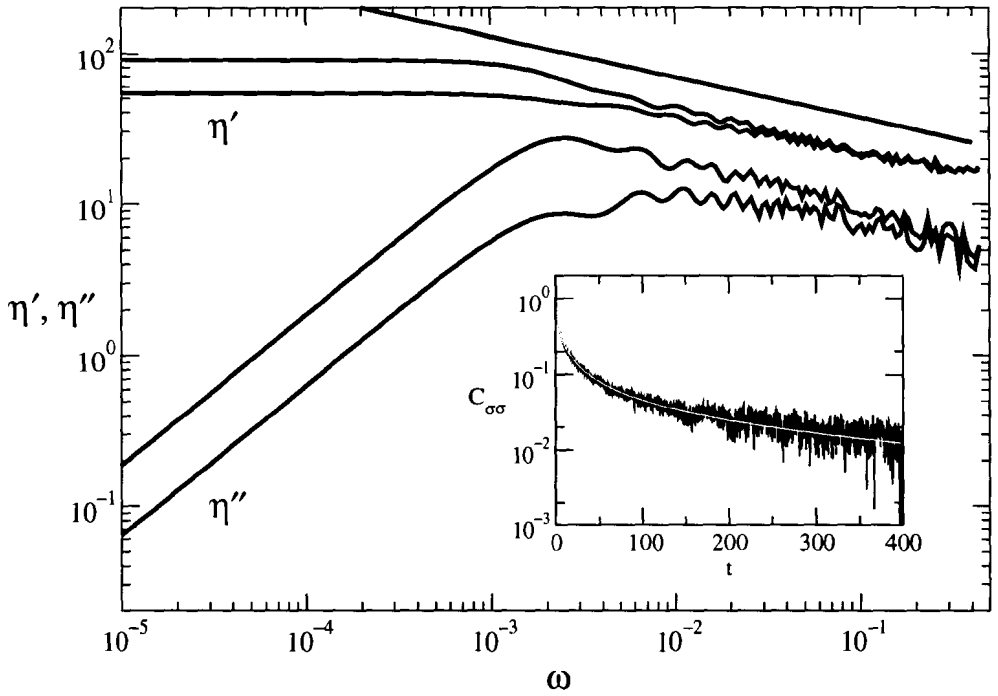


Figure 9.9: The real and imaginary parts of the complex viscosity $\eta^*$ close to $p_c$. The lower curve of each pair is at $p = 0.2$ and the upper curve is at $p = 0.24$. The straight line shows the power law form for large $\omega$; both parts of $\eta^*$ should be proportional to $\omega^{u-1}$. Here, $u = 0.77$. The inset shows the stress-stress correlation function for $p = 0.24$, and a stretched exponential fit to this data (grey line). The exponent in the stretched exponential here is 0.15.

in the inset of figure 9.9). This form is predicted in some theoretical calculations [74] and is expected in any system with a continuous distribution of relaxation times [90], which might be expected to occur here. Clusters of different sizes may have different associated relaxation times and, as the network becomes highly bonded, stressed regions in different clusters may relax with different timescales.

Figure 9.10 shows the data for the shear modulus as a function of bond probability $p$, for several different system sizes. Far from $p_c$, the results are consistent with a power law, with strong finite size effects visible close to $p_c$. To determine the power law governing the behaviour of an infinite system, a finite size scaling analysis has been done. This analysis begins with a form which is assumed to describe the finite

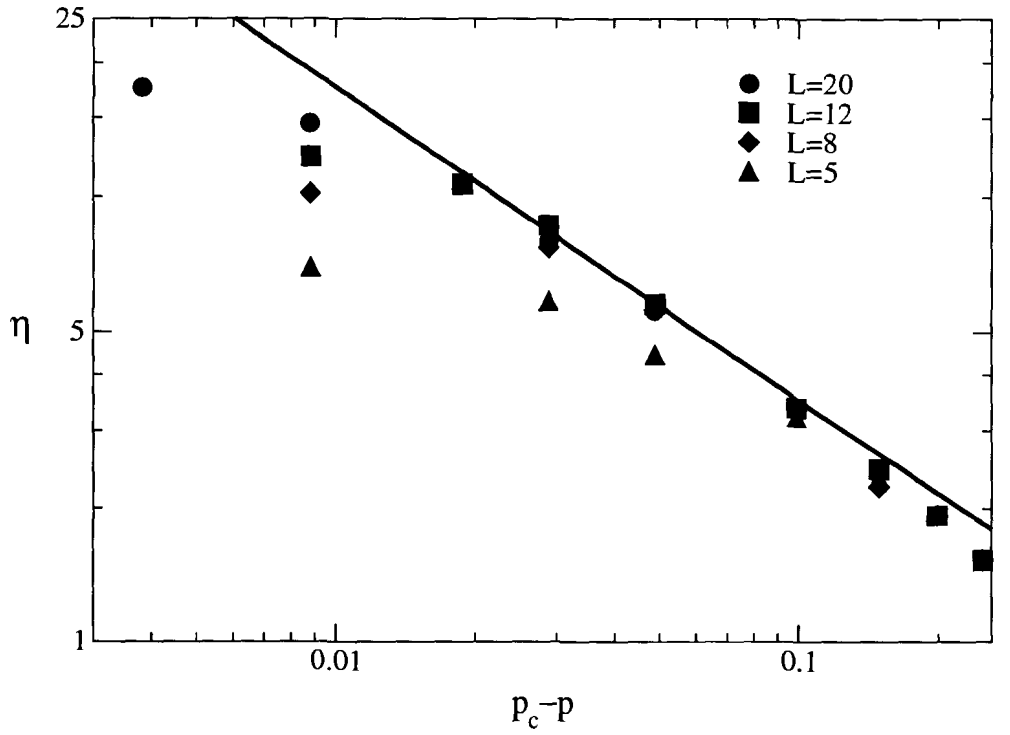


Figure 9.10: The raw data for the viscosity in $d = 3$, as functions of $p_c - p$. The line shows a power law, proportional to $(p_c - p)^{-0.7}$.

size effects on the data. If in the infinite system limit the viscosity scales as

$$\eta \sim (p_c - p)^{-s}, \tag{9.3}$$

then in a finite system of linear size $L$ it should be given by

$$\eta \sim L^{s/\nu} f((p_c - p)^{\nu} L). \tag{9.4}$$

Here, $\nu$ is the correlation length exponent and has been determined in simulations to be $\nu = 0.876$ in three dimensions. This form can be derived using renormalization group methods and should be exact in the large system limit [21, 91]. The scaling function $f(x)$ should behave as $f \sim x^{-s/\nu}$ for large values of $x$, so as to be consistent with the infinite system size limit.

The results of this finite size scaling analysis are shown in figure 9.11. The collapse onto a single scaling function for all system sizes is quite good. The line shows the

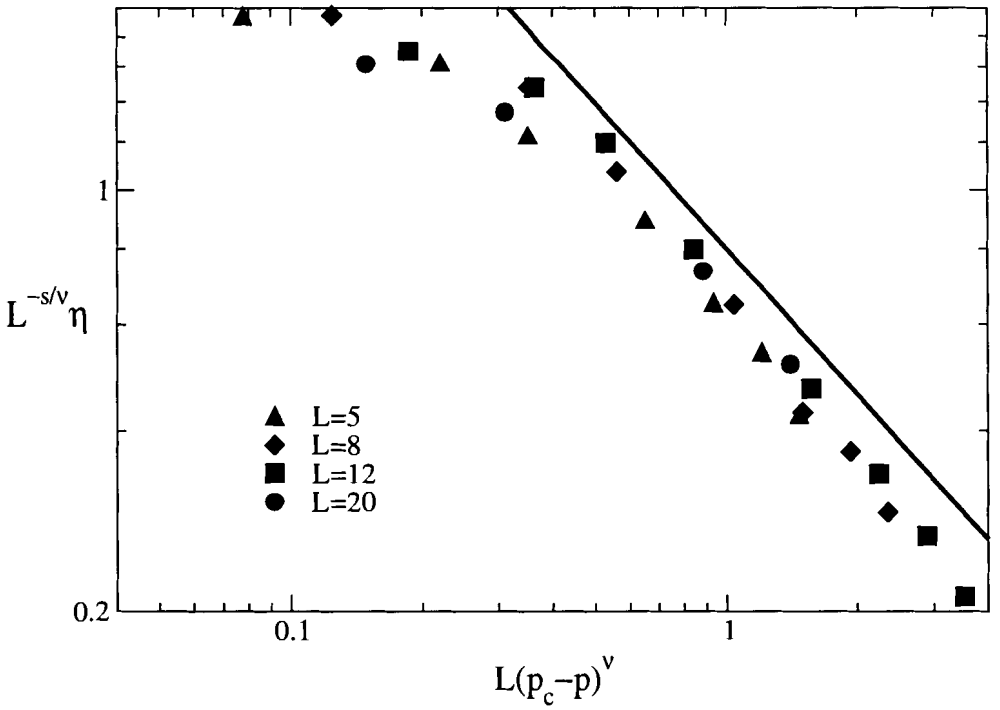


Figure 9.11: Finite size scaled data in $d = 3$. The line shows the expected form of the scaling function at large $(p_c - p)^{\nu} L$.

asymptotic form of the scaling function, and it can be seen that the trend of the data is toward this line.

These two figures show that the viscosity of the system simulated scales as a power law, with an exponent $s = 0.7$. This is consistent with several of the theoretical approaches discussed in chapter 7.

## 9.4 Conclusions

The results of section 9.2 show that the Green-Kubo equilibrium method and the direct simulation of shear flow produce the same estimates for the viscosity of crosslinked materials, at least at the low crosslink densities where these methods are compared in figure 9.4. The results of non-equilibrium simulations over a range of $p$ suggest that both the viscosity and normal stress coefficient of a gelling system in two dimensions

diverge near the gel points, with exponents $s \approx 2$ and $\ell \approx 6$. While extrapolation to the $\dot{\gamma} = 0$ value of the viscosity is difficult, many different methods of performing this extrapolation produce the same scaling behaviour.

Section 9.3 shows results demonstrating that the viscosity of a model gel diverges near the percolation point $p_c$ in three dimensions. The divergence of the viscosity has been measured in experiments on several different materials, as discussed in section 7.4. The experimental results seem to fall into two groups: some with exponents near $s = 1.4$, and some with exponents near $s = 0.7$. The three-dimensional simulations discussed here are consistent with the latter set of experiments. The same simulations are consistent with two of the calculations discussed in section 7.5: the "electrical analogy" suggested by de Gennes, and the calculations done using a Rouse model done by the Zippelius group. However, the results of simulations in two dimensions are consistent with neither calculation. This may indicate that the analytical calculations do not apply to the model, or that there are problems peculiar to two dimensions. A recent paper [92] suggests that two dimensions is special for randomly crosslinked materials. The conclusion of this paper is that the localization length of a two-dimensional crosslinked material diverges logarithmically with the system size, and so the phase above the percolation transition may not be a normal solid.

Since both $s$ and $u$ have been measured for the three-dimensional fluid, the dynamical scaling relation of section 7.5.1 may be used to calculate a value for $t$, the exponent governing the growth of the shear modulus above $p_c$. Using $s = 0.7$ and $u = 0.75$, dynamical scaling implies $t = 2.1$. This gives a consistency check with previous work on a similar model [93, 94, 53], though without excluded volume interactions, which gave $t \approx 2$.

The results here are somewhat complementary to our results in [93, 94, 53]. In this earlier work, the exponent governing the increase of the the shear modulus above the percolation transition was measured. This exponent is related to the exponents measured here, through the dynamical scaling relations, and the exponents measured here are consistent with earlier results. The model used there was somewhat simpler, without the excluded volume interaction used here. One of the issues of importance in this earlier work was the location of the critical point at which this randomly diluted

material begins to behave as a solid. At zero temperature, the transition to a solid happens at $p$ well above the percolation point, while our earlier results show that at finite temperature the percolation point also marks the transition to a solid state. The divergence of the viscosity as $p_c$ is approached from below lends further support to this result.

The divergence of the normal stress close to $p_c$ has not been measured in an experiment. As suggested by [74], it would be interesting to see an experimental value of this exponent, as $\Psi_1$ diverges very rapidly near $p_c$ in both the two-dimensional simulations done here and the calculations of [74, 76]. This should make it easy for an experimentalist to see a power law. Measuring the divergence of $\Psi_1$ would also give another independent dynamical quantity. By measuring both $\eta$ and $\Psi_1$, the ratio of the exponents could be determined from a purely dynamical experiment without knowing the critical point, by plotting $\Psi_1$ as a function of $\eta$. This would be useful, as $p_c$ is often difficult to determine accurately in an experiment. The ratio of $s$ to $\ell$ would then provide a dynamical exponent characteristic of the dynamical universality class of the material studied. It should be possible to determine both quantities in one experiment.

The only other calculation of $\ell$ is in [74, 76]. The value determined in these simulations is again bigger than the calculated value. This may be due to the fact that the calculation is for a model with Rouse dynamics, which would indicate a lack of universal scaling of $\Psi_1$. This may also be due to the possible special nature of the amorphous state in two dimensions.

## 9.5 Future Work

The simulations done here were performed to try to gain some understanding of which microscopic features are important for the macroscopic behaviour of gels and thus to which universality class a particular material should belong. There are several issues which could be addressed to extend the work done here.

One difference between experiments and the simulations done here is that the

experiments are usually done at constant pressure, unlike the constant volume simulations done here. It is possible that in experiments the density could vary as the number of crosslinks is varied, and so the material studied in experiments could approach the critical point along another path. It might be useful to repeat these simulations using a constant pressure technique.

The simulations discussed above provide a characterization of the critical properties of a particular microscopic model of a randomly crosslinked material as it approaches its transition to a gel. An obvious question remains: is it possible to obtain different exponents for other microscopic models and, if so, what are the important features controlling the exponents? The experiments discussed in section 7.4 showed a wide range of exponents, and a better understanding of the features required to produce a set of exponents in a model would be useful in determining the important experimental features. In the theoretical calculations done by the Zippelius group discussed in section 7.5.4, the crossover exponent $\phi$ is related to dynamical exponents. This exponent characterizes the internal structure of clusters and is independent of the other exponents of the percolation problem. It may be possible to vary this exponent and to see how the exponents governing dynamical properties. It may also be useful to study random clusters generated in other ways, to explore the dependence of the dynamical quantities on the usual static exponents. The gelation process allows other possible sets of exponents describing the static structure, though most experiments in which exponents are measured show the percolation ones. There has been an attempt in this direction [95], but a more systematic approach would be helpful.

One possible reason for the difficulty in obtaining good results near $p_c$ in two dimensions is the much larger spring constant ($k = 40$ rather than $k = 5$) used in these simulations, as compared to the simulations in three dimensions. This was done in an attempt to make the effects of the crosslinking more noticeable but also may mean that the simulation takes longer to equilibrate and that relaxation is slower at a fixed $p$. Repeating the simulations with different bond potentials might make it easier to get closer to $p_c$ and also would be a way to test the universality of the exponents measured here.

The three-dimensional simulations reported above used the equilibrium Green-Kubo formula to determine the viscosity, and the normal stress differences could not be measured directly, as was done in the two-dimensional simulations. Non-equilibrium simulations of the same model in three dimensions are under way, and so it will be possible to determine the divergence of the normal stress coefficient in the physically relevant case of three dimensions. If the exponent governing the divergence of $\Psi_1$ does match the value calculated by the Zippelius group, then this would lend support to the idea that the exponents are universal in three dimensions, and that two dimensions is in some way special.

# Bibliography


[1] Jean-Louis Barrat, Mikhail Feigelman, Jorge Kurchan and Jean Dalibard (eds.), *Slow Relaxations and Non-equilibrium Dynamics in Condensed Matter*, Session LXXVII of *École D'éte de Physique des Houches* (Springer-Verlag, 2003).

[2] P. C. Hohenberg and B. I. Halperin, "Theory of dynamic critical phenomena," *Reviews of Modern Physics*, **49** (3) 435–479 (July 1977).

[3] B. Schmittmann and R. K. P. Zia, *Statistical Mechanics of Driven Diffusive Systems*, volume 17 of *Phase Transitions and Critical Phenomena* (Academic Press, London, 1995).

[4] Ron Kroon, Hilde Fleurent and Rudolf Sprik, "Diffusion-limited exciton fusion reaction in one-dimensional tetramethyammonium mangenese trichloride (TMMC)," *Physical Review E*, **47** (4) 2462–2472 (April 1993).

[5] Doug Toussaint and Frank Wilczek, "Particle-antiparticle annihilation in diffusive motion," *Journal of Chemical Physics*, **78** (5) 2642–2647 (March 1983).

[6] M. v. Smoluchowski, "Drei Vorträge über Diffusion, Brownsche Molekularbewegung und Koagulation von Kolloidteilchen," *Physikalische Zeitscrift*, **17** 557–571,585–599 (1916).

[7] M. v. Smoluchowski, "Versuch einer mathematischen Theorie der Koagulationskinetik kolloider Lösungen," *Zeitschrift Phys. Chem., Stoechiom. Verwandtschaftsl.*, **92** 129–168 (1917).

[8] Z. Rácz, "Nonequilibrium Phase Transitions," in Barrat *et al.* [1].

[9] Benjamin P. Lee, "Renormalization group calculation for the reaction $kA \to \emptyset$," *Journal of Physics A: Mathematical and General*, **27** 2633–2652 (1994).

[10] John Cardy and Uwe C. Täuber, "Theory of Branching and Annihilating Random Walks," *Physical Review Letters*, **77** (23) 4780–4783 (December 1996).

[11] John Cardy and Uwe C. Täuber, "Field Theory of Branching and Annihilating Random Walks," *Journal of Statistical Physics*, **90** (1) 1–56 (January 1998).

[12] Géza Ódor, "Universality classes in nonequilibrium lattice systems," to appear in Reviews of Modern Physics, July 2004.

[13] Daniel Vernon and Martin Howard, "Branching and annihilating Lévy flights," *Physical Review E*, **63** 041116 (April 2001).

[14] Daniel C. Vernon, "Long range hops and the pair annihilation reaction $A+A \to \emptyset$: Renormalization group and simulation," *Physical Review E*, **68** 041103 (2003).

[15] Christoph Bennemann, Claudio Donati, Jörg Baschnagel and Sharon C. Glotzer, "Growing range of correlated motion in a polymer melt on cooling towards the glass transition," *Nature*, **399** (6733) 246–249 (May 1999).

[16] The Chemical Society, *Non-Equilibrium Behaviour of Colloidal Dispersions*, volume 123 of *Faraday Discussions* (2003).

[17] Daniel Vernon, Michael Plischke and Béla Joós, "Viscoelasticity near the gel point: A molecular dynamics study," *Physical Review E*, **64** 031505 (2001).

[18] William Feller, *An introduction to probability theory and its applications*, volume 1, third edition (Wiley, New York, 1968).

[19] N. G. van Kampen, *Stochastic Processes in Physics and Chemistry*, second edition (Elsevier, Amsterdam, 1997).

[20] Michael Plischke and Birger Bergersen, *Equilibrium Statistical Mechanics*, second edition (World Scientific, Singapore, 1994).

[21] John Cardy, *Scaling and Renormalization in Statistical Physics*, no. 5 in Cambridge Lecture Notes in Physics (Cambridge University Press, Cambridge UK, 1996).

[22] Jean-Philippe Bouchaud and Antoine Georges, "Anomalous diffusion in disordered media: statistical mechanics, models and physical applications," *Physics Reports*, **195** (4) 127–293 (1990).

[23] Harvey Scher and Elliot W. Montroll, "Anomalous transit-time dispersion in amorphous solids," *Physical Review B*, **12** (6) 2455–2477 (September 1975).

[24] E. W. Montroll and M. F. Shlesinger, "The wonderfull world of random walks," in E. W. Montroll and J. L. Lebowitz (eds.), *Nonequilibrium Pheomena II: From Stochastics to Hydrodynamics*, volume XI of *Studies in Statistical Mechanics*, chap. 1, pp. 1–121 (Elsevier, Amsterdam, 1984).

[25] T. H. Solomon, Eric R. Weeks and Harry L. Swinney, "Observation of Anomalous Diffusion and Lévy Flights in Two-Dimensional Rotating Flow," *Physical Review Letters*, **71** (24) 3975–3978 (December 1993).

[26] Eric R. Weeks and Harry L. Swinney, "Random walks and Lévy flights observed in fluid flows," *Nonlinear Science Today* (1998).

[27] A. Ott, J. P. Bouchaud, D. Langevin and W. Urbach, "Anomalous Diffusion in "Living Polymers": a Genuine Levy Flight?" *Physical Review Letters*, **65** (17) 2201–2204 (October 1990).

[28] F. James, "A Review of Pseudorandom Number Generators," *Computer Physics Communications*, **60** (3) 329–344 (October 1990).

[29] J. M. Chambers, C. L. Mallows and B. W. Stuck, "A Method for Simulating Stable Random Variables," *Journal of the American Statistical Association*, **71** (354) 340–344 (June 1976).

[30] Paul Bratley, Bennett L. Fox and Linus E. Schrage, *A Guide to Simulation*, second edition (Springer-Verlag, New York, 1987).

[31] Masao Doi, "Second quantization representation for clasical many-particle system," *Journal of Physics A: Mathematical and General*, **9** (9) 1465–1477 (September 1976).

[32] Masao Doi, "Stochastic theory of diffusion-controlled reaction," *Journal of Physics A: Mathematical and General*, **9** (9) 1479–1495 (September 1976).

[33] L. Peliti, "Path integral approach to birth-death processes on a lattice," *Journal de Physique*, **46** (9) 1469–1483 (Septembre 1985).

[34] John Cardy, "Renormalisation Group Approach to Reaction-Diffusion Problems," in J. M. Drouffe and J. B. Zuber (eds.), *The Mathematical Beauty of Physics*, volume 24 of *Advanced Series in Mathematical Physics* (World Scientific, 1996).

[35] Benjamin Lee, *Critical Behaviour in Non-Equilibrium Systems*, Ph.D. thesis, Santa Barbara (1994).

[36] Kurt Gottfried and Tung-Mow Yan, *Quantum Mechanics: Fundamentals* (Springer-Verlag, New York, 2003).

[37] Daniel C. Mattis and M. Lawrence Glasser, "The uses of quantum field theory in diffusion-limited reactions," *Reviews of Modern Physics*, **70** (3) 979–1001 (July 1998).

[38] B. Friedman, G. Levine and Ben O'Shaughnessy, "Renormalization-group study of field-theoretic $A+A \rightarrow \emptyset$," *Physical Review A*, **46** (12) R7343–R7346 (December 1992).

[39] Hans-Karl Janssen, "On a Lagrangean for Classical Field Dynamics and Renormalization Group Calculations of Dynamical Critical Properties," *Zeitschrift für Physik B: Condensed Matter*, **23** (4) 377–380 (1976).

[40] C. de Dominicis, "Techniques de renormalisation de la théorie des champs et dynamique des phénomnès critiques," *Journal de Physique Colloque*, **37** (1) C1–247–C1–253 (Janvier 1976).

[41] H. Hinrichsen and M. Howard, "A model for anomalous directed percolation," *European Physical Journal B*, **7** 635–643 (1999).

[42] J. J. Binney, N. J. Dowrick, A. J. Fisher and M. E. J. Newman, *The Theory of Critical Phenomena: An Introduction to the Renormalization Group* (Oxford University Press, Oxford, 1992).

[43] P. Grassberger and A. de la Torre, "Reggeon Field Theory (Schlögl's First Model) on a Lattice: Monte Carlo Calculations of Critical Behaviour," *Annals of Physics*, **122** 373–396 (1970).

[44] A. A. Lushnikov, "Binary reaction $1 + 1 \rightarrow 0$ in one dimension," *Physics Letters A*, **120** (3) 135–137 (February 1987).

[45] Sungchul Kwon and Hyunggyu Park, "Reentrant phase diagram of branching annihilating random walks with one and two offspring," *Physical Review E*, **52** (6) 5955–5960 (December 1995).

[46] Faith A. Morrison, *Understanding Rheology* (Oxford, 2001).

[47] H. A. Barnes, J. F. Hutton and K. Walters, *An Introduction to Rheology* (Elsevier, Amsterdam, 1989).

[48] John D. Ferry, *Viscoelastic Properties of Polymers*, second edition (Wiley, 1970).

[49] M. E. Cates, "Structural Relaxation and Rheology of Soft Condensed Matter," in Barrat *et al.* [1].

[50] Ronald G. Larson, *The Structure and Rheology of Complex Fluids* (Oxford University Press, Oxford, 1999).

[51] Dietrich Stauffer and Amnon Aharony, *Introduction to Percolation Theory*, second edition (Taylor and Francis, London, 1991).

[52] Muhammad Sahimi, *Appplications of Percolation Theory* (Taylor and Francis, London, 1994).

[53] Daniel Vernon, *Numerical Investigations of the Role of Disorder in Models of Growth and of Rigidity*, Master's thesis, Simon Fraser University (1999).

[54] J. P. Cohen Addad (ed.), *Physical Properties of Polymeric Gels* (Wiley, 1996).

[55] James E. Martin and Douglas Adolf, "The sol-gel transition in chemical gels," *Annual Review of Physical Chemistry*, **42** 311–339 (month 1991).

[56] Charles P. Lusignan, Thomas H. Mourey, John C. Wilson and Ralph H. Colby, "Viscoelasticity of randomly branched polymers in the critical percolation class," *Physical Review E*, **52** (6) 6271–6280 (1995).

[57] M. A. V. Axelos and M. Kolb, "Crosslinked Biopolymers: Experimental Evidence for Scalar Percolation Theory," *Physical Review Letters*, **64** (12) 1457–1460 (March 1990).

[58] E. Bouchaud, M. Delsanti, M. Adam, M. Daoud and D. Durand, "Gelation and percolation: swelling effect," *Journal de Physique*, **47** 1273–1277 (Août 1986).

[59] M. Adam, M. Delsanti, J. P. Munch and D. Durand, "Size and mass determination of clusters obtained by polcondensation near the gelation threshold," *Journal de Physique*, **48** 1809–1818 (Octobre 1987).

[60] M. Adam, M. Delsanti, D. Durand, G. Hild and J. P. Munch, "Mechanical properties near gelation threshold, comparison with classical and 3d percolation," *Pure and Applied Chemistry*, **53** 1489–1494 (1981).

[61] M. Adam, M. Delsanti and D. Durand, "Mechanical Measurements in the Reaction Bath during the Polycondensation Reaction, near the Gelation Threshold," *Macromolecules*, **18** (11) 2285–2290 (1985).

[62] D. Durand, M. Delsanti, M. Adam and J. M. Luck, "Frequency Dependence of Viscoelastic Properties of Branched Polymers near Gelation Threshold," *Europhysics Letters*, **3** (3) 297–301 (February 1987).

[63] F. Devreux, J. P. Boilot, F. Chaput and L. Mailier, "Crossover from scalar to vectorial percolation in silica gelation," *Physical Review E*, **47** (4) 2689–2694 (April 1993).

[64] P. G. de Gennes, "Critical behaviour for vulcanization processes," *Journal de Physique Lettres*, **38** (17) L355–L358 (Septembre 1977).

[65] P. G. de Gennes, "On a relation between percolation theory and the elasticity of gels," *Le Journal de Physique Lettres*, **37** (1) 1–2 (January 1976).

[66] P. G. de Gennes, "Incoherent scattering near a sol gel transition," *Le Journal de Physique Lettres*, **40** (9) 197–199 (May 1979).

[67] Pierre-Gilles de Gennes, "Viscosité près d'une transition sol-gel," *Comptes Rendus de l'Acadamie des Sciences Série B*, **286** 131–133 (1978).

[68] W. Tang and M. F. Thorpe, "Mapping between random central-force networks and random resistor networks," *Physical Review B*, **36** (7) 2798–3804 (September 1987).

[69] H. J. Herrmann, B. Derrida and J. Vannimenus, "Superconductivity exponents in two- and three-dimensional percolation," *Physical Review B*, **30** (7) 4080–4082 (October 1984).

[70] Michael Rubinstein and Ralph H. Colby, *Polymer Physics* (Oxford University Press, Oxford, 2003).

[71] Kurt Broderix, Henning Löwe, Peter Müller and Annette Zippelius, "Critical dynamics of gelation," *Physical Review E*, **63** 011510 (December 2000).

[72] M. E. Cates, "Brownian dynamics of self-similar macromolecules," *Journal de Physique*, **46** (7) 1059–1077 (Juillet 1985).

[73] K. Broderix, H. Löwe, P. Müller and A. Zippelius, "Shear viscosity of a crosslinked polymer melt," *Europhysics Letters*, **48** (4) 421–427 (November 1999).

[74] Kurt Broderix, Timo Aspelmeier, Alexander K. Hartmann and Annette Zippelius, "Stress relaxation of near-critical gels," *Physical Review E*, **64** 021404 (August 2001).

[75] Kurt Broderix, Peter Müller and Annette Zippelius, "Normal stresses at the gelation transition," *Physical Review E*, **65** (4) 041505 (April 2002).

[76] Peter Müller, "Critical behaviour of the Rouse model for gelling polymers," *Journal of Physics A:Mathematical and General*, **36** 10443–10450 (2003).

[77] Daan Frenkel and Berend Smit, *Understanding Molecular Simulation*, second edition (Academic Press, 2001).

[78] M. P. Allen and D. L. Tildesley, *Computer Simulation of Liquids* (Oxford University Press, 1987).

[79] William G. Hoover, *Computational Statistical Mechanics*, volume 11 of *Studies in Modern Thermodynamics* (Elsevier, Amsterdam, 1991).

[80] J. M. Thijssen, *Computational Physics* (Cambridge, 1999).

[81] M. Tuckerman, B. J. Berne and G. J. Martyna, "Reversible multiple time scale molecular dynamics," *Journal of Chemical Physics*, **97** (3) 1990–2001 (August 1992).

[82] Shuichi Nosé, "A unified formulation of the constant temperature methods," *Journal of Chemical Physics*, **81** (1) 511–519 (1984).

[83] William G. Hoover, "Canonical dynamics: Equilibrium phase-space distributions," *Physical Review A*, **31** (3) 1695–1697 (March 1985).

[84] A. W. Lees and S. F. Edwards, "The computer study of transport under extreme conditions," *Journal of Physics C: Solid State*, **5** (15) 1921–1929 (August 1972).

[85] Denis J. Evans and G. P. Morriss, "Nonlinear-response theory for steady planar Couette flow," *Physical Review A*, **30** (3) 1528–1530 (1984).

[86] Fei Zhang, Debra J. Serles, Denis J. Evans, Jan S den Toom Hansen and Dennis J. Isbiter, "Kinetic energy conserving integrators for Gaussian thermostatted SLLOD," *Journal of Chemical Physics*, **111** (1) 18–26 (July 1999).

[87] Steven Y. Liem, David Brown and Julian H. R. Clarke, "Investigation of the homogeneous-shear nonequilibrium-molecular-dynamics method," *Physical Review A*, **45** (6) 3706–3713 (March 1992).

[88] M. Ferrario, G. Ciccotti, B. L. Holian and J. P. Ryckaert, "Shear-rate dependence of the viscosity of the Lennard-Jones liquid at the triple point," *Physical Review A*, **44** (10) 6936–6939 (November 1991).

[89] Mattias Fuchs and Michael E. Cates, "Non-Newtonian viscosity of interacting Brownian particles: comparision of theory and data," *Journal of Physics: Condensed Matter*, **15** S401–S406 (2003).

[90] R. G. Palmer, D. L. Stein, E. Abrahams and P. W. Anderson, "Models of Hierarchically Constrained Dynamics for Glassy Relaxation," *Physical Review Letters*, **53** (10) 958–961 (September 1984).

[91] M. N. Barber, "Finite-size Scaling," in C. Domb and J. L. Lebowitz (eds.), *Phase Transitions and Critical Phenomena*, volume 8 (Academic Press, London, New York, 1983).

[92] Paul M. Goldbart, Swagatam Mukhopadhyay and Annette Zippelius, "Goldstone-type fluctuations and their implications for the amorphous solid state," eprint `cond-mat/0405145`.

[93] Michael Plischke and Béla Joós, "Entropic Elasticity of Diluted Central Force Networks," *Physical Review Letters*, **80** (22) 4907–4910 (June 1998).

[94] M. Plischke, D. C. Vernon, B. Joós and Z. Zhou, "Entropic rigidity of randomly diluted two- and three-dimensional networks," *Physical Review E*, **60** (3) 3129–3135 (September 1999).

[95] Michael Plischke, D. C. Vernon and Béla Joós, "Model for gelation with explicit solvent effects: Structure and dynamics," *Physical Review E*, **67** 011401 (2003).